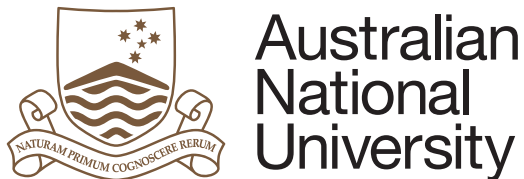


# **Arm Length Stabilisation for Advanced Gravitational Wave Detectors**

Adam Joseph Mullavey

A thesis submitted for the degree of  
Doctor of Philosophy  
of the Australian National University

January 2012





# Declaration

This thesis is an account of research undertaken between February 2007 and January 2012 at the Department of Quantum Science, Research School of Physics and Engineering, Australian National University. The research was under the supervision of Professor David McClelland.

Unless otherwise stated, the work presented within this thesis is my own.

A handwritten signature in black ink, appearing to read "Adam Mullavey".

Adam Joseph Mullavey  
January, 2012



# Acknowledgements

The submission of this thesis, for me, brings an end to five years of post-graduate studies, six years with the Centre for Gravitational Physics, nine years at the Australian National University and ten years of higher education. I therefore have many people to thank.

Let me start by thanking my PhD supervisors - David McClelland, Bram Slagmolen and Daniel Shaddock.

To David, I thank for his patience (which I know I must have tested) over the years, and for creating an excellent group to be a part of. I also thank David for his continued support, especially in the last year when that submission date just kept getting pushed back further and further.

To Bram Slagmolen, whose absence last year was noticed by none more than me, I thank for his unwavering support over the last five years, which without I know I could never have made it to the end. I also thank Bram for helping me find a project for this doctoral thesis.

To Daniel Shaddock, I thank for sharing his technical wisdom. The conversations we had, were always very informative. I learnt a great deal.

As mentioned I have been with the Centre for Gravitational Physics for six years and in that time the group has changed and grown considerably, but has always been a fantastic place to work, and so I thank all of the ‘Graviteers’ I have known in my time, but I’d particularly like to thank - Conor Mow-Lowry, Jong Chow, John Miller, James Dickson, Sheon Chua, Tim Lam, Michael Stefsky, Danielle Wuchenich, Thanh Nguyen, Andrew Sutton, Andrew Wade, Silvie Ngo, Alberto Stochino, Dave Bowman and Ra Inta.

Special thanks has to go to John Miller, for basically being Bram substitute for the last year, for proof reading the majority of my thesis and for giving very helpful suggestions. Also, to Jong for who provided me with some good advice in trying to decide what to do post-PhD.

I’d like to thank the Ebdenites (past and present) - Wes, Al, Alex, Laurie, James, Beth and Seb, for making 32 Ebden St inhabitable, and for not kicking me out (mostly speaking to Wes and Al). I’d especially like to thank Al and Wes for being such fantastic mates over the years and James for his friendship over the last year. I’d also like to thank Al and Alex for the intense and exciting games of ‘Settlers’.

I want to thank my big sisters Bec, Andrea and Kylie for always looking out for their little bro. I’d especially like to thank Andrea and Paul for many a free meal and local support. Having family in the vicinity who I could see every week has meant so much and

I hope I can pay you back some day.

And finally I could never have made it to where I am today without the love, support, encouragement, and advice from my parents. Thank you Mum and Dad for helping me become the person I am today.

# Abstract

Currently the Laser Interferometric Gravitational-wave Observatory (LIGO) is undergoing upgrades from Initial LIGO to become Advanced LIGO. Amongst these upgrades is the addition of a signal recycling mirror at the output port of the interferometer; upgrades of the mirror suspensions to quadruple pendulums; the implementation of less invasive and hence weaker test mass actuators; and the change of readout scheme from a heterodyne based RF readout to a homodyne based DC readout.

The DC readout scheme requires the installation of an Output Mode Cleaner (OMC), to stop ‘junk light’ generated in the interferometer from making its way to the DC photodetector where it can limit the sensitivity of the gravitational wave detector. The steering of the interferometer beam into the OMC will be handled by Tip Tilt mirrors designed at the Australian National University. The first core piece of work presented in this thesis was:

- The characterisation of a prototype Tip Tilt mirror, which involved measuring the various eigenmodes of the mirror.

The Advanced LIGO upgrades are critical in improving the gravitational wave sensitivity of the interferometer, however they also add to the complexity of the instrument. Lock acquisition is the process of taking the multiple degrees of freedom of the interferometer to their required operating points. The lock acquisition problem is made considerably more difficult by these upgrades and as such a deterministic lock acquisition scheme will be implemented as opposed to the probabilistic scheme of Initial LIGO.

An important part of this deterministic lock acquisition scheme will be the Arm Length Stabilisation system. The Arm Length Stabilisation system will be responsible for the stabilisation and tuning of the arm cavities of the interferometer independent of the other degrees of freedom during the lock acquisition process. The majority of the work presented in this thesis is motivated by the Arm Length Stabilisation system. This work includes:

- The experimental verification of an Arm Length Stabilisation system on a benchtop suspended Fabry-Perot cavity formed from two Tip Tilt mirrors.
- The development of a new technique for the stable transfer of an optical frequency through an optical fibre.



# Contents

<b>Acknowledgements</b>	<b>v</b>
<b>Abstract</b>	<b>vii</b>
<b>1 Introduction</b>	<b>1</b>
1.1 Summary of PhD Activities . . . . .	1
1.2 Thesis Overview . . . . .	1
1.3 List of Relevant Publications . . . . .	3
<b>2 Gravitational Wave Detection</b>	<b>5</b>
2.1 Gravitational Wave Theory . . . . .	5
2.2 Astrophysical Sources of Gravitational Waves . . . . .	6
2.3 Gravitational Wave Detection . . . . .	8
2.4 The Michelson Interferometer . . . . .	9
2.5 Limitations To Sensitivity . . . . .	11
2.5.1 Noise . . . . .	11
2.5.2 Increase the Response to the Signal . . . . .	13
2.6 Fabry-Perot Cavity Enhancement . . . . .	14
2.6.1 Arm Cavities . . . . .	16
2.6.2 Power Recycling . . . . .	18
2.6.3 Signal Recycling . . . . .	19
2.7 LIGO . . . . .	20
2.7.1 Initial LIGO . . . . .	21
2.7.2 Advanced LIGO . . . . .	23
2.8 Summary . . . . .	26
<b>3 Interferometric Sensing Techniques</b>	<b>27</b>
3.1 Heterodyne and Homodyne Interferometry . . . . .	27
3.2 Pound Drever Hall Readout of a Simple Cavity . . . . .	30
3.3 Pound Drever Hall Readout of a Three Mirror Coupled Cavity . . . . .	33
3.4 Initial LIGO Readout . . . . .	35
3.5 Advanced LIGO Readout . . . . .	37
3.6 Summary . . . . .	40

<b>4 Tip Tilt Mirrors</b>	<b>41</b>
4.1 Cavity Misalignment Coupling . . . . .	41
4.2 Mechanical Design . . . . .	42
4.2.1 Pendulum Isolation . . . . .	44
4.2.2 Blade Springs . . . . .	45
4.3 Tip Tilt Mirror Control . . . . .	47
4.3.1 Electromagnetic Actuation . . . . .	47
4.3.2 Local Sensing . . . . .	48
4.4 Tip Tilt Characterisation . . . . .	49
4.4.1 Shadow Sensor Calibrations . . . . .	50
4.4.2 Transfer Functions Measurements . . . . .	51
4.4.3 Vertical Mode Measurement . . . . .	54
4.4.4 Tip Tilt Structure Eigenmodes . . . . .	54
4.5 Summary . . . . .	56
<b>5 Lock Acquisition and Arm Length Stabilisation</b>	<b>59</b>
5.1 The Lock Acquisition Problem . . . . .	59
5.1.1 Threshold Velocity . . . . .	59
5.1.2 Dynamic Sensing Matrix . . . . .	60
5.2 The Probabilistic Approach to Lock Acquisition in Initial LIGO . . . . .	61
5.3 The Deterministic Approach to Lock Acquisition in Advanced LIGO . . . . .	63
5.4 Arm Length Stabilisation . . . . .	64
5.4.1 The Suspension Point Interferometer . . . . .	65
5.4.2 Digitally Enhanced Heterodyne Interferometry . . . . .	65
5.4.3 Dual Frequency Pound Drever Hall . . . . .	67
5.5 Summary . . . . .	68
<b>6 Dual Frequency PDH Stabilisation Experiment</b>	<b>71</b>
6.1 Suspended Test Cavity . . . . .	71
6.1.1 Science PDH readout . . . . .	73
6.1.2 Tip Tilt actuation . . . . .	76
6.2 Locking the Auxiliary Laser to the Cavity . . . . .	76
6.2.1 Auxiliary Laser . . . . .	78
6.2.2 Digital PDH readout . . . . .	80
6.2.3 Auxiliary Laser Locking Controller . . . . .	81
6.3 Relative Frequency Measurement . . . . .	83
6.4 ALS Control Loop . . . . .	87
6.5 Tuneability of the Cavity . . . . .	91
6.6 Cavity Stability . . . . .	93
6.7 Control Transfer . . . . .	97
6.8 Discussion . . . . .	99
6.9 Summary . . . . .	99

<b>7 Stable Transfer of an Optical Frequency Through A Fibre</b>	<b>101</b>
7.1 Heterodyning via a 4km Fibre . . . . .	101
7.2 A Novel Technique for Fibre Frequency Noise Suppression . . . . .	103
7.3 Experiment . . . . .	106
7.4 Results . . . . .	108
7.5 Discussion . . . . .	109
7.6 Summary . . . . .	110
<b>8 Conclusion and Future Work</b>	<b>111</b>
8.1 Double Pendulum Suspension for the Tip Tilt Mirrors . . . . .	111
8.2 Digitally Enhanced Heterodyne Interferometry for Lock Acquisition . . . . .	112
8.3 Further Testing of the PLL Fibre Stabilisation Technique . . . . .	112
<b>A Feedback Control Systems</b>	<b>115</b>
<b>B Tip Tilt to OMC Dither Locking</b>	<b>119</b>
<b>C Air Turbulence Effects</b>	<b>121</b>
<b>D Common Fibre Suppression Technique</b>	<b>127</b>
<b>Bibliography</b>	<b>130</b>



# List of Figures

2.1	A ring of test masses as a gravitational wave passes through. The top set shows the $h_+$ polarisation, and the bottom set shows the top shows the $h_\times$ polarisation . . . . .	6
2.2	A Michelson Interferometer and it's optical fields. BS = Beam-splitter, EMX = End Mirror X, EMY = End Mirror Y . . . . .	10
2.3	Magnitude of the transfer function from the motion of the pendulum suspension point (sp) to that of the test mass (tm). . . . .	12
2.4	Sensitivity of the differential arm phase to a gravitational wave signal for Michelson interferometers with arm lengths of 4 km and 40 km. . . . .	14
2.5	The optical fields of a Fabry-Perot cavity formed between two mirrors, the input mirror (IM) and the end mirror (EM). . . . .	15
2.6	Plots for the cavity responses, for under-coupled (red), impedance matched (green) and over-coupled (blue) cavities. The top plots are for the amplitude response, the bottom plots are the phase response. . . . .	16
2.7	The optical fields of a Michelson interferometer with arm cavities. The arm cavities can be treated as compound mirrors with complex reflectivities $F_{xarm}$ and $F_{yarm}$ . . . . .	17
2.8	The optical fields of a power recycled Michelson interferometer. . . . .	18
2.9	The optical fields of a signal recycled Michelson interferometer. . . . .	19
2.10	The design sensitivities for Initial and Advanced LIGO, and the achieved sensitivity for Initial LIGO during the fifth science data run (S5). . . . .	20
2.11	The Initial LIGO architecture - a power recycled Michelson interferometer with arm cavities . . . . .	21
2.12	Schematics of (a) the suspended core optic for Initial LIGO, showing the four coil-magnet actuators and (b) the seismic isolation system for Initial LIGO, showing the four mass-spring layers of the passive stack. . . . .	22
2.13	The Advanced LIGO architecture - a dual recycled Michelson interferometer with arm cavities . . . . .	24
2.14	Solidworks drawings of (a) the total seismic isolation setup for the test mass (b) the quadruple suspension (c) the internal seismic isolation table and (d) the hydraulic external pre-isolator. . . . .	25

---

2.15	The modeled displacement noise for an Advanced LIGO test mass (TM) and also the internal seismic isolation (ISI) platform. . . . .	26
3.1	A common scheme for obtaining a heterodyne measurement of the phase of a system. . . . .	28
3.2	A scheme for obtaining the in-phase and quadrature components . . . . .	29
3.3	A Pound Drever Hall readout scheme for a Fabry-Perot cavity. . . . .	31
3.4	The in-phase (I) and quadrature (Q) error signals, for the reflected, circulating and transmitted pick-offs. Top row: $\nu_m >> HWHM$ . Bottom row: $\nu_m = HWHM$ . . . . .	33
3.5	The sensitivity of the error signal to the cavity roundtrip phase on resonance as a function of the modulation frequency. . . . .	34
3.6	Pound Drever Hall readout scheme for a three mirror coupled cavity. . . . .	34
3.7	The readout scheme for the Initial LIGO detector. . . . .	36
3.8	Basic schematic for the readout scheme for the Advanced LIGO interferometer. . . . .	38
3.9	Layout of the OMC cavity. The carrier from the Dual Recycled Fabry-Perot Michelson (DFM) is transmitted through the OMC, while the junk light is reflected off. . . . .	39
4.1	Translational (x) and Angular Misalignments ( $\theta$ ) inside a Fabry-Perot Cavity. $w_0$ is the waist radius and $\theta_0$ is the divergence angle of the cavities fundamental mode. . . . .	41
4.2	Steering of the interferometer output beam into the OMC by the Tip Tilts. .	42
4.3	The schematic overview of the suspended optic of the Tip Tilt design, showing the six degrees of freedom - longitudinal, transverse, vertical, yaw, pitch and roll. . . . .	43
4.4	An engineering rendering of the Tip Tilt suspension stage. . . . .	44
4.5	The cantilever blade springs and their mounting unit. . . . .	46
4.6	A schematic overview of the electromagnetic actuation of the Tip Tilt mirror showing the coil-magnet configuration. . . . .	48
4.7	The local sensing scheme for the Tip Tilt mirrors, showing the flags attached to the back of the mirrors and the shadow sensors which consist of a Light Emitting Diode (LED) shining light onto a Photo-diode (PD). . . . .	49
4.8	The prototype Tip Tilt mirror. . . . .	50
4.9	Calibration of the four OSEM shadow sensors over a range UL = Upper Left, UR = Upper Right, LL = Lower Left, LR = Lower Right. . . . .	51
4.10	Transfer function from force applied by the coil actuators to longitudinal position of mirror. . . . .	52
4.11	Transfer function from torque applied in pitch by the coil actuators to mirror pitch. . . . .	53

---

4.12 Transfer function from torque applied in yaw by the coil actuators to mirror yaw. . . . .	53
4.13 Spectra of the vertical bounce mode data. . . . .	54
4.14 Setup for measuring the eigenfrequencies of the mechanical modes of the Tip Tilt structure. . . . .	55
4.15 Measured eigenmodes of the Tip Tilt structure. . . . .	56
5.1 Shows the lock acquisition of a simple cavity when (a) the velocity of the mirror is less than the threshold velocity (b) the mirror velocity is greater than the threhold velocity. The top plots show the mirror displacement over time, whereas the bottom plots show the force applied by the actuator (green) and the error signal sent to the actuator (red). . . . .	61
5.2 The five states of lock acquisition for Initial LIGO (see text for description of these states). . . . .	62
5.3 The basic idea behind the Suspension Point Interferometer . . . . .	65
5.4 Schematic for Digitally Enhanced Heterodyne Interferometry. IM = Input Mirror, CM = Coupling Mirror, EM = End Mirror . . . . .	66
5.5 A table showing heterodyne signals for PRN encoding and decoding. . . . .	66
5.6 The dual frequency PDH readout scheme. . . . .	68
6.1 The configuration of the experiment for testing the Arm Length Stabilisation scheme using dual frequency PDH readout. . . . .	72
6.2 Simplified diagram of the Tip Tilt cavity and PDH scheme. . . . .	74
6.3 Calibration of the error signal. (a) full 10s trace of the error signal (b) zoomed in error signal around the carrier and sideband resonance (c) the absolute gradient of the error signal over 10s and (d) the absolute gradient of the zoomed in error signal. . . . .	75
6.4 The position response of Tip Tilt 1 to a signal from the CDS. . . . .	76
6.5 Schematic of the auxiliary laser locking loop. . . . .	77
6.6 Block diagram of the auxiliary laser locking loop. The various components and signals are described in the text. . . . .	77
6.7 The frequency response of the auxiliary laser's green frequency to a voltage sent through the high voltage amplifier into the auxiliary laser PZT. . . . .	79
6.8 Diagram showing the digital PDH readout. . . . .	80
6.9 Calibration of the digital PDH error signal. (a) full 10 second trace of the error signal (b) zoomed in error signal around the carrier and sideband resonance (c) the absolute gradient of the error signal over the full 10 seconds and (d) the absolute gradient of the zoomed in error signal. . . . .	81
6.10 The gain of the controller for the auxiliary locking loop. The DAC conversion is included in the gain of the controller. . . . .	82

6.11	Bode plots for (a) the modelled and measured open loop gain (OLG) for the auxiliary laser locking loop and (b) the modelled response of the auxiliary laser frequency to the cavity length. . . . .	83
6.12	The setup for obtaining the relative frequency measurement between the two lasers. . . . .	84
6.13	Diagram of the Digital Phase Locked Loop . . . . .	85
6.14	A block diagram of the DPLL . . . . .	85
6.15	(a) The modelled open loop gain (OLG) of the DPLL and (b) The modelled and measured frequency-meter gain. . . . .	87
6.16	A time trace of the frequency difference between the two lasers, as measured by the DPLL. . . . .	88
6.17	Feedback to the Tip Tilt mirror via the CDS system. . . . .	88
6.18	Block diagram of the ALS control loop . . . . .	89
6.19	A time trace of the relative frequency between the two lasers, when the measurement is fed back to the Tip-Tilt actuators. . . . .	90
6.20	Measured and modelled ALS open loop gain . . . . .	91
6.21	Schematic for the tuning of the relative frequency between the lasers and therefore the tuning of the cavity length. . . . .	92
6.22	Tuning of the frequency offset over 160 MHz. Top - Normalised cavity transmission of the science infrared laser, Middle - Science PDH error signal, Bottom - Normalised cavity transmission of the auxiliary green laser. . . . .	93
6.23	The transmitted infra-red power (top plot) with the newly optimised ALS setup and the transmitted green power (bottom plot) for comparison. . . . .	94
6.24	The displacement noise of the cavity measured using the science laser PDH, and the in-loop ALS. The ALS stability requirement and the integrated RMS of the science PDH measurement have also been included. . . . .	94
6.25	The initial stability performance, optimised performance and all measured noise sources. . . . .	96
6.26	Diagram showing the basic scheme for transferring the control of the cavity from the ALS feedback to the science PDH feedback. . . . .	97
6.27	Time traces of the transmitted science laser power (top), the ALS and science PDH gains (middle), and the transmitted auxiliary green laser power, during the handoff procedure. . . . .	98
7.1	Relative frequency measurement scheme when the science laser is sent through an optical fibre. . . . .	102
7.2	Feedback of the fibre transfer corrupted heterodyne to the auxiliary laser frequency. . . . .	103
7.3	Transfer functions from (a) the fibre induced frequency fluctuations to the truth measurement and (b) the science laser frequency to the truth measurement. . . . .	104

7.4	Basic layout of the technique where the sum of the phasemeter readouts are fed back to the auxiliary laser to cancel out fibre induced phase noise. . . . .	105
7.5	Transfer function from the relative frequency between the auxiliary and science laser to the summed heterodyne signal. . . . .	106
7.6	Bench-top experiment configuration to test out the technique. . . . .	107
7.7	The true measurement of the relative frequency noise between the two lasers when the auxiliary laser is phase locked to the science laser for the case where: (a) the fibre is bypassed, (b) the fibre is included and the remote signal used for feedback and (c) the fibre is included and the equal delay sum of the local and remote signals fed back to the laser . . . . .	109
A.1	A schematic of a feedback control system and all of its components. $C(\omega)$ , $A(\omega)$ , and $S(\omega)$ represent the frequency dependent transfer functions of the controller, actuator and sensor. $r(\omega)$ , $\varepsilon(\omega)$ and $o(\omega)$ represent the rereference, error and output signals. . . . .	116
A.2	A Bode plot of the open loop gain. The unity gain frequency, phase margin and gain margin are all shown. . . . .	117
B.1	Steering of the IFO beam into the OMC by the Tip Tilts. . . . .	119
C.1	The experimental setup to look at dispersive effects within the cavity. . . . .	122
C.2	Top: Spectra of the equivalent displacement noise for the auxiliary correction measurement and the infrared sideband measurement. Middle: The ratio between the two measurements. Bottom: The coherence between the two measurements. . . . .	123
C.3	The Tip Tilt cavity with the perspex beam tube enclosing the intra-cavity beams. . . . .	124
C.4	The auxiliary correction measurement and the infrared sideband measurements with and without the perspex beam tube. . . . .	125
D.1	The basic schematic for the AOM fibre noise suppression technique. . . . .	127
D.2	Transfer functions from the equivalent fibre frequency fluctuations and the absolute science laser frequency fluctuations to the truth measurement, using the AOM technique. . . . .	128



# Chapter 1

## Introduction

### 1.1 Summary of PhD Activities

As part of the LIGO Scientific Collaboration (LSC), the work presented in this thesis is motivated by research and development for the Laser Interferometric Gravitational Wave Observatory (LIGO).

My PhD began with a year at LIGO where I participated in the Astrowatch program which involved a group of like-minded PhD students operating the 2km interferometric gravitational wave detector at the LIGO Hanford site. During this time I gained considerable insight into the complexity of such an instrument, particularly in sensing and control, and in lock acquisition.

During this time at LIGO, I also assembled and installed newly designed Tip Tilt mirrors. From the installation of the Tip Tilt mirrors, improvements were made to the Tip Tilt mirror design. Chapter 4 presents results, characterising the performance of a prototype Tip Tilt mirror incorporating the new design.

Upon my return to the Australian National University, I continued working on LIGO research and development, participating in the design study of an Arm Length Stabilisation system to be used as part of a deterministic lock acquisition scheme for Advanced LIGO. The majority of the work presented in this thesis is motivated by the Arm Length Stabilisation (ALS) system.

My initial work on this ALS system was on a new technique for the stable transfer of an optical frequency through an optical fibre. This work is presented in Chapter 7. The most significant piece of work however is associated with prototyping the ALS system on a bench-top experiment using a dual frequency Pound-Drever-Hall readout method. This work is presented in Chapter 6.

### 1.2 Thesis Overview

In Chapter 2 a background on gravitational waves is given. This includes the theory behind their prediction, and a summary of the expected astronomical and cosmological sources. This is followed by a description of the techniques, both past and present, that

have been used in a global effort to detect them. Since the content of this thesis is aimed towards ground-based interferometric gravitational wave detection, the last two thirds of Chapter 2 are devoted to interferometric detection, which includes a description of the Michelson interferometer, the main limitations to detector sensitivity, and the use of Fabry-Perot cavities for enhancing their sensitivity. The chapter ends with a closer look at the current long baseline ground-based interferometric detector - the Laser Interferometric Gravitational Wave Observatory (LIGO). A description of Initial LIGO and details for the planned Advanced LIGO are given.

In Chapter 3 a general overview of the interferometric sensing techniques used for detecting the operating condition of the interferometer are presented. These techniques include heterodyne and homodyne interferometry, and the Pound-Drever-Hall technique. It should be noted that this chapter has two purposes, the first is to provide the required background to the interferometric sensing techniques used for the main experimental work presented in this thesis. The second is to give a working understanding of the techniques used for the readout of the LIGO degrees of freedom. At the end of the chapter a description of the Initial LIGO RF and Advanced LIGO DC readout schemes are provided. The Advanced LIGO DC readout includes a description of the Output Mode Cleaner.

Chapter 4 gives an overview of the design of the Tip Tilt mirrors and presents results measuring the performance of a prototype Tip Tilt mirror. The Tip Tilt mirrors will be responsible for actively steering the Advanced LIGO interferometer output beam into an Output Mode Cleaner as part of the DC readout scheme. A complete description of the mechanical design and requirements is provided. The sensing and control schemes are described in detail. The chapter ends showing measurements characterising the performance of the Tip-Tilt mirrors. The design of these mirrors was predominantly carried out by Dr. Bram Slagmolen at The Australian National University, who also assisted in the measurements of the performance, along with Dr. John Miller.

Chapter 5 discusses the difficulties of lock acquisition of a gravitational wave detector and looks at how the problem was approached in Initial LIGO and how it will be carried out for Advanced LIGO. This leads to the introduction of the notion of an Arm Length Stabilisation system to be used as part of a deterministic lock acquisition scheme for Advanced LIGO. The end of the chapter discusses three techniques proposed for the Arm Length Stabilisation system - the suspension point interferometer, digitally enhanced heterodyne interferometry and dual frequency Pound-Drever-Hall.

Chapter 6 gives a detailed step by step description of the setup of an experiment to employ an Arm Length Stabilisation system for a suspended Fabry-Perot cavity made from two of the Tip Tilt mirrors. This Arm Length Stabilisation system is based on the dual frequency Pound-Drever-Hall readout method. The end of the chapter presents results measuring the performance of the system with respect to two requirements.

Chapter 7 discusses the stable transfer of an optical frequency through an optical fibre. A new technique is described and the results for an experiment testing this technique are presented.

### 1.3 List of Relevant Publications

- **Adam J. Mullavey**, Bram J. J. Slagmolen, John Miller, Matthew Evans, Peter Fritschel, Daniel Sigg, Sam J. Waldman, Daniel A. Shaddock and David E. McClelland, “*Arm-length stabilisation for interferometric gravitational-wave detectors using frequency-doubled auxiliary lasers*”, Optics Express **20**, 81-89 (2012)
- **Adam J. Mullavey**, Bram J. J. Slagmolen, Daniel A. Shaddock and David E. McClelland, “*Stable transfer of an optical frequency standard via a 4.6 km optical fiber*”, Optics Express **18**, 5213-5220 (2010)
- Bram J. J. Slagmolen, **Adam J. Mullavey**, John Miller, David E. McClelland and Peter Fritschel, “*Tip-tilt mirror suspension: Beam steering for advanced laser interferometer gravitational wave observatory sensing and control signals*”, Review of Scientific Instruments **82**, 125108 (2011)



## Chapter 2

# Gravitational Wave Detection

At the beginning of the 20th Century, Albert Einstein dramatically changed the way we think about the universe. First he derived his Special Theory of Relativity [1], which proposed that the speed of light is constant in all inertial reference frames. One consequence of Special Relativity was that nothing in the universe could travel faster than the speed of light. This was in direct disagreement with Newton's theory of gravity, which was considered to be instantaneous, even between objects large distances apart. This led Einstein to formulate his own theory of gravity, and ten years after he published his work on Special Relativity, he published a paper on his General Theory of Relativity [2].

The central idea of general relativity is that gravity is really just a warping of space-time around massive bodies. The planets are really moving in a straight line through space, but the space is curved around the sun and therefore the planets move in an orbit. An object free falling towards Earth, is really moving at a constant velocity through space but space becomes more stretched closer to the Earth and therefore the object appears to accelerate.

A less obvious consequence of general relativity, is the prediction of oscillations of the space-time metric called Gravitational Waves [3, 4]. Gravitational Waves and their elusive detection provide the ultimate motivation for this thesis, and will be covered in this chapter.

### 2.1 Gravitational Wave Theory

Applying a weak field limit to the Einstein field equations yields an approximation of the space-time metric:

$$g_{\mu\nu} \simeq \eta_{\mu\nu} + h_{\mu\nu} \quad (2.1)$$

where  $\eta_{\mu\nu}$  is the Minkowski metric, which represents flat space, and  $h_{\mu\nu}$  is a small perturbation. It is shown in [5] and [6] that the small perturbation yields wavelike solutions:

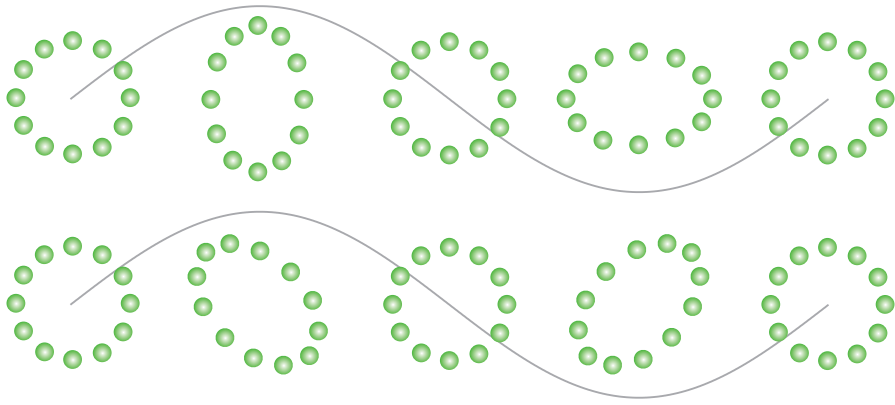


Figure 2.1: A ring of test masses as a gravitational wave passes through. The top set shows the  $h_+$  polarisation, and the bottom set shows the top shows the  $h_x$  polarisation

$$h_{\mu\nu} = \begin{pmatrix} 0 & 0 & 0 & 0 \\ 0 & h_+ & h_x & 0 \\ 0 & h_x & -h_+ & 0 \\ 0 & 0 & 0 & 0 \end{pmatrix} \cos(\omega(t - z/c)) \quad (2.2)$$

where  $\omega$  is the gravitational wave frequency. Just like their electromagnetic counterparts gravitational waves travel at the speed of light and have two polarisation states. Unlike electromagnetic waves which are generated by accelerating charges, gravitational waves are generated by accelerating mass. They also have a quadrupole like geometry, which is best illustrated by the effect they have on a ring of test particles, shown in Figure 2.1. A gravitational wave passing through this ring of test masses, results in one axis expanding and contracting while the other axis contracts and expands. The strength of a gravitational wave is described in terms of the strain in space,  $h$ , that it induces. The induced fractional length change caused by the gravitational wave as it passes is given by

$$\frac{h}{2} = \frac{\Delta L}{L} \quad (2.3)$$

where  $\Delta L$  is the induced length change and  $L$  is the length over which the measurement is made.

## 2.2 Astrophysical Sources of Gravitational Waves

Gravitational radiation arises from accelerating mass distributions, where the motion isn't spherically or cylindrically symmetric. Our attempts to build an instrument sensitive enough to detect gravitational waves, are largely motivated by the desire to gain an understanding of the astrophysical or cosmological objects that produce them. In this section a brief description of some of the predicted sources is given, however for a more in-depth look at the astrophysics of gravitational waves, the reader is directed to the review article [7].

### Binary Star Systems

High mass binary systems, made up of black holes and neutron stars, are a good target for gravitational wave searches, as the mechanism by which they generate gravitational waves, according to general relativity, is well understood and modelled [7].

As the two stars orbit one another, they lose orbital kinetic energy to gravitational radiation, which in effect reduces their orbital period and distance. The efficiency of this energy transfer increases as the stars move closer to each other. The resulting gravitational wave signal therefore accelerates in its frequency increase, resulting in what is commonly referred to as a chirp.

Coalescing binaries are the most promising source of gravitational wave signals as the waveform of such a signal is accurately predicted and can be searched for using matched-filtering [8].

There is indirect evidence of the existence of gravitational waves, from the observations of the neutron star system PSR1913+16 [9]. One of the neutron stars is a pulsar meaning that the orbital period of the system can be accurately measured. The orbital period was plotted verse time and shown to be decaying exactly as if it were losing energy to gravitational waves, as predicted by general relativity [10].

### Pulsars

Gravitational waves are generated from imperfections in the spherical geometry of a rotating neutron star. The gravitational wave carries angular momentum and energy away, resulting in the neutron star spinning down. For pulsars the spin rate can be measured, which makes them ideal for targeted gravitational wave searches.

The observed spin-down times for most of the known pulsars are too long for the associated gravitational wave signals to be detectable by current gravitational wave detectors. For the few candidates with short enough spin-downs, an upper limit can be set on the percentage of rotational energy lost to gravitational radiation, based on the sensitivity of current gravitational wave detectors.

One such example is the Crab Pulsar, whose young age means that it has a relatively short spin-down. An upper limit of 2% has been set on the amount of rotational energy lost in the form of gravitational waves [11].

### Gravitational Collapse

A highly evolved star collapsing under its own gravity can result in the emission of gravitational waves through many different mechanisms [12]. Some of these collapses result in the largest explosions in the universe, referred to as Supernovae (and Hypernovae) which can also produce gravitational waves [13].

Numerical simulations of gravitational wave collapse events is a very active area in computational astrophysics [12], however due to the complex nature of the collapse and the limitations of current computers, much of the physics behind the collapse is still unknown.

Observations by gravitational wave detectors should provide unique information of these stellar core collapse events.

### Stochastic

Quite possibly the most enticing aspect of gravitational wave astronomy is the prediction of a stochastic background of gravitational radiation. Some of this stochastic background is due to countless unresolved astrophysical sources. The more interesting part is due to sources of cosmological origin, referred to as a cosmic gravitational wave background.

Unlike its electromagnetic astronomy counterpart, the cosmic microwave background, which only provides observations as far back as 380000 years after the Big Bang, the detection of a cosmic gravitational wave background would allow for the recovery of information about the universe in its earliest epochs, going as far back as  $10^{-30}$  seconds after the Big Bang.

Predictions from standard inflation models put stochastic gravitational wave induced strains at a magnitude beyond the detection capabilities of even the next generation of gravitational wave detectors, however limits have been set by correlating the output of multiple detectors [14].

## 2.3 Gravitational Wave Detection

Whilst gravitational waves are generated by the most violent events in the universe, the extreme stiffness of space-time means that gravitational waves have tiny amplitudes. Consider that for a coalescing binary system with each star 1.4 solar masses located in the nearby Virgo cluster, the maximum strain we expect to see on Earth is  $10^{-21}$  [15]. This is equivalent to the distance from here to the sun changing by the diameter of an atom. It is obvious that instruments of unprecedented sensitivity are required to measure such tiny fluctuations.

The first gravitational wave detectors were resonant bar detectors, designed and constructed by Joseph Weber [16]. These detectors were aluminium bars, with a natural resonance frequency the same as the gravitational wave frequency of some predicted sources. In 1969, Weber reported that two of his detectors had been simultaneously excited by a gravitational wave [17]. However his results could not be repeated. Despite this apparent failure to detect a gravitational wave, Weber's work sparked more interest in the field.

In current times, optical interferometry techniques provide the best chance for detecting gravitational waves. It was one of Weber's former students, Robert Forward, who in the early 1970s along with his colleagues built the first gravitational wave interferometer [18, 19]. At about the same time Rainier Weiss performed a detailed analysis outlining the main limitations to the sensitivity of a long baseline interferometric detector [20]. This work, along with work from other pioneers such as Ron Drever has led to the construction of a global network of kilometre scale interferometric gravitational wave detectors.

The largest (4 km long) and most sensitive of these detectors belong to the Laser

Interferometric Gravitational-Wave Observatory (LIGO) [21] in the US. Next in scale and sensitivity is the French-Italian built 3 km Virgo detector [22] located in Italy, followed by the 600m German-British built GEO-600 [23, 24] in Germany and then TAMA-300 [25] in Japan. The goal of the first generation of detectors has been to show that instruments of such sensitivity could be built, operated for sustained periods of time, and record useful data. In this regard they have been a success, however, to date there has been no direct gravitational wave detection.

Over the next decade, the second generation of detectors will come online. These detectors are expected to have the required sensitivity to detect gravitational waves on a regular basis. Currently LIGO and Virgo are undergoing substantial upgrades to become Advanced LIGO [26] and Advanced Virgo [27] respectively. GEO600 is undergoing upgrades to become GEO-HF, where HF (High Frequency) refers to the detector's improvement in sensitivity at frequencies above 1 kHz by about an order of magnitude [28]. The construction of the Large-Scale Cryogenic Gravitational-Wave Telescope (LCGT) [29] in Japan began in 2010.

In addition to the ground-based detectors, there are plans to put interferometric gravitational wave detectors into space. The most well known of these is the Laser Interferometer Space Antenna (LISA) [30], which is being developed by the European Space Agency (ESA)<sup>1</sup>.

Each ground-based gravitational wave detector is a Michelson interferometer enhanced by coupled Fabry-Perot cavities. In the following section we will analyse a Michelson interferometer and deduce why it is an ideal device for gravitational wave detection. We will then discuss the main limitations to the sensitivity of such a device, which will then be followed by an introduction to Fabry-Perot cavities and how they can be used to enhance a Michelson's sensitivity.

## 2.4 The Michelson Interferometer

A Michelson interferometer, illustrated in Figure 2.2, consists of a beamsplitter and two end mirrors. Laser light incident on the Michelson is split into two perpendicularly propagating beams by the beam splitter, which travel down to the end mirrors where they are reflected back towards the beam splitter to be recombined. There are two ports where the light can exit the interferometer. The port where the light exits back towards the laser is referred to as the symmetric port, and the other exit port is referred to as the asymmetric port.

Assuming no scattering or absorption losses the responses of the symmetric field ' $E_{sym}$ ' and asymmetric field ' $E_{asy}$ ' to the incident field ' $E_{inc}$ ' can be derived from the reflectivity ' $R_{optic}$ ' and transmissivity ' $T_{optic}$ ' of each optic, where the reflectivity and transmissivity are defined as the ratio of optical power they reflect or transmit. The optical power is the square of the electric field amplitude, and therefore we will define the amplitude reflectivity

---

<sup>1</sup>This was originally a joint NASA-ESA project however recent developments in 2011 have led to ESA pursuing the project on their own.

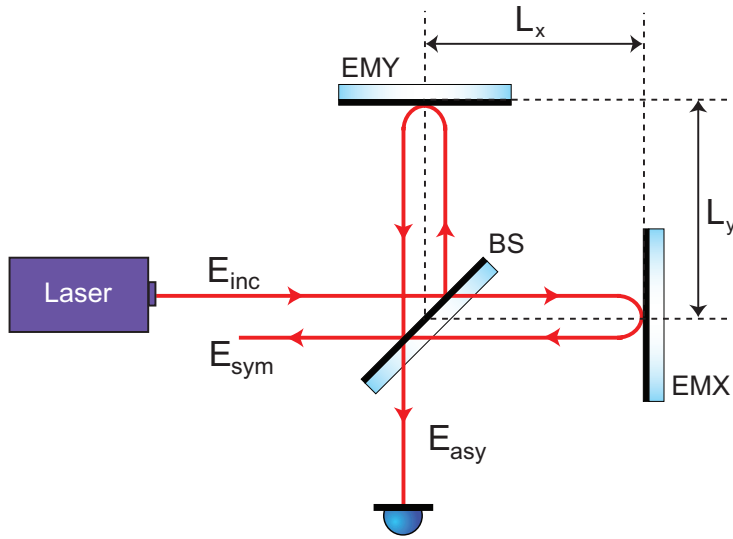


Figure 2.2: A Michelson Interferometer and its optical fields. BS = Beam-splitter, EMX = End Mirror X, EMY = End Mirror Y

of each optic as  $r_{optic} = \sqrt{R_{optic}}$ , and the amplitude transmissivity as  $t_{optic} = \sqrt{T_{optic}}$ . The convention where a field receives a  $\pi$  phase shift upon reflection off the coating side of the optic is adopted.

The beam-splitter is 50% reflective ( $R_{bs} = T_{bs} = 0.5$ ). The length of each arm, i.e. the distance between beam-splitter and end mirror, is denoted with ‘ $L_x$ ’ and ‘ $L_y$ ’. The phase shift imparted onto the optical field after it has probed the arm, commonly referred to as the roundtrip phase is given by:

$$\phi_{x,y} = \frac{4\pi L_{x,y}}{\lambda} \quad (2.4)$$

where  $\lambda$  is the optical wavelength of the light source used. The symmetric and asymmetric field responses to the incident field are given by:

$$F_{sym} = \frac{E_{sym}}{E_{inc}} = -\frac{1}{2} (r_{emx}e^{i\phi_x} + r_{emy}e^{i\phi_y}) \quad (2.5)$$

$$F_{asy} = \frac{E_{asy}}{E_{inc}} = -\frac{1}{2} (r_{emx}e^{i\phi_x} - r_{emy}e^{i\phi_y}) \quad (2.6)$$

If the end mirrors have equal reflectivity,  $r_{emx} = r_{emy} = r_{em}$  (typical for gravitational wave detectors), then the Michelson responses can be rewritten as:

$$F_{sym} = -r_{em}e^{i\phi_+} \cos \phi_- \quad (2.7)$$

$$F_{asy} = -r_{em}e^{i\phi_+} i \sin \phi_- \quad (2.8)$$

where  $\phi_+ = (\phi_x + \phi_y)/2$  is the common arm phase and  $\phi_- = (\phi_x - \phi_y)/2$  is the differential arm phase.

The differential and common arm phase information are encoded onto the phase of the light, which can be read out using heterodyne detection techniques (see Chapter 3). Due to its quadrupole moment, a gravitational wave with the right polarization traveling

perpendicular to the interferometer plane would impose itself onto the differential arm phase of the interferometer. Changes in the differential arm phase are given by:

$$\Delta\phi_- = \frac{4\pi L_-}{c} \Delta\nu + \frac{4\pi\nu}{c} \Delta L_- \quad (2.9)$$

where  $L_-$  is the macroscopic differential arm length,  $\nu$  is the optical frequency,  $c$  is the speed of light in a vacuum,  $\Delta\nu$  represent changes in optical frequency, and  $\Delta L_-$  represent changes in the differential arm length.

A gravitational wave of strength  $h$ , will result in a change of length  $\Delta L_x = hL_x/2$  in one arm and  $\Delta L_y = -hL_y/2$  in the other, resulting in differential arm length change of  $\Delta L_- = hL_+$ . Here  $L_+$  is the average arm length. There are a variety of noise sources that will shake the mirrors differentially, which we will label  $\Delta d_-$ . Substituting  $\Delta L_- = hL_+ + \Delta d_-$  into Equation 2.9 gives:

$$\Delta\phi_- = \frac{4\pi L_-}{c} \Delta\nu + \frac{4\pi\nu}{c} \Delta d_- + \frac{4\pi\nu L_+}{c} h \quad (2.10)$$

Note that the above equation assumes that the travel time of the light in the arms is considerably less than the period of the gravitational wave. Equation 2.10 shows that to detect the gravitational wave the laser frequency noise and displacement noise components need to be made small enough so as not to mask the gravitational wave.

## 2.5 Limitations To Sensitivity

The sensitivity is defined in terms of signal to noise ratio. From the third term in Equation 2.10 the response to the gravitational wave signal is given by  $4\pi\nu L_+/c$ . The other two terms in the equation constitute noise, as they are unwanted signals that can mask the gravitational wave signal.

### 2.5.1 Noise

The first term in Equation 2.10 represents laser frequency noise  $\Delta\nu$ . The second term represents displacement noise  $\Delta d_-$  which refers to any noise that results from unwanted motion of the interferometer optics. Another important type of noise that isn't represented in Equation 2.10 is readout noise which arises from uncertainty in the read out of the differential arm phase  $\Delta\phi_-$ .

#### Laser Frequency Noise

Various sources can result in the frequency of the laser fluctuating. These sources include technical noise such as temperature fluctuations of the laser gain medium and quantum noise. There exist various techniques for stabilising the frequency of a laser, such as locking to a highly stable cavity [31]. Also from the first term in Equation 2.10, one obvious way to reduce the instruments response to laser frequency fluctuations is to reduce the macroscopic differential arm length  $\Delta L_-$ , (make the arms the same length).

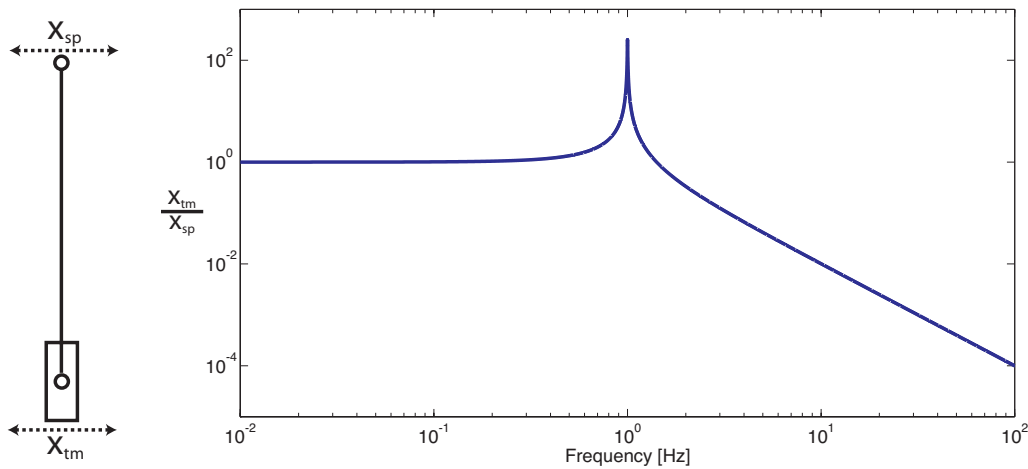


Figure 2.3: Magnitude of the transfer function from the motion of the pendulum suspension point (sp) to that of the test mass (tm).

### Displacement Noise

Displacement noise refers to any noise that results from unwanted motion of the interferometer optics. Notable sources of displacement noise include seismic noise, thermal noise and radiation pressure noise.

Ideally for a gravitational wave detector, the mirrors would be free-falling. Here though we are considering ground-based detectors for which the mirrors are connected to the surface of the earth. Seismic vibrations therefore couple directly to the motion of the mirrors. This seismic noise can be anthropogenic (man-made) or natural. The mirrors can be seismically isolated by suspending them on pendulums. Figure 2.3 shows the transfer function from the motion of the suspension point to the suspended test mass, for a pendulum with a resonance frequency of 1 Hz. Below the pendulum resonance the response is unity and flat, around resonance the motion of the suspension point is amplified and above resonance the response falls off as the inverse Fourier frequency squared ( $f^{-2}$ ). Therefore the pendulum acts as a filter of high frequency seismic noise.

Thermal or Brownian motion of the individual particles within the mirror substrates and coatings, and also within the mirror suspensions is another type of displacement noise. From the Fluctuation Dissipation Theorem [32, 33], using high Q (low loss) materials for the suspensions [34, 35] and mirror coatings [36, 37] reduces thermal noise.

Radiation pressure noise refers to noise that occurs from fluctuations in the intensity of the light pushing on the mirrors in the arms. It can be either classical or quantum. More often than not classical radiation pressure fluctuations will be common to both arms. However they can couple into the differential arm phase through imbalances in the masses of the arm mirrors or through imbalances in the circulating cavity power between the arms due to differing scatter losses in the coatings of the test masses or the beam-splitter not being perfectly 50/50.

Quantum fluctuations in the amplitude of the light are uncorrelated between the arms

and therefore result in differential displacement of the end mirrors, limiting the gravitational wave sensitivity [38]. The quantum radiation pressure limited signal to noise scales inversely with the square root of the power in the arms [39].

$$SNR_{rpn} \propto \frac{1}{\sqrt{P}} \quad (2.11)$$

Therefore radiation pressure noise can be reduced by decreasing the power incident on the Michelson. The first generation of interferometric detectors were not limited by radiation pressure noise, however the second generation detectors are expected to be limited between 10 and 50 Hz [40].

### Readout Noise

Any uncertainty that arises from the readout of the differential arm phase  $\Delta\phi_-$  is referred to as readout noise. The most noteable form of readout noise is photo-electron shot noise.

The readout of the differential arm phase  $\Delta\phi_-$ , involves detection of the optical field that falls onto the photo-detector (explained in Chapter 3). A photo-detector is a device that measures optical power by effectively counting the photons that hit the diode per some interval of time.

The photon number in a given laser beam follows Poissonian counting statistics and as such will have some statistical uncertainty. The shot noise limited sensitivity is proportional to the square root of the power in the arms [39].

$$SNR_{sn} \propto \sqrt{P} \quad (2.12)$$

Therefore shot noise can be reduced by increasing the power incident on the Michelson. First generation detectors were limited and the second generation detectors are expected to be shot noise limited above a few hundred Hertz.

#### 2.5.2 Increase the Response to the Signal

From the third term in Equation 2.10 one clear method for boosting a Michelson's response to a gravitational wave is to increase the length of the arms. However, Equation 2.10 assumes that the storage time of the light in the arms is considerably less than the period of the gravitational wave. Increasing the length of the arms increases the light storage time which in turn decreases the frequency range of which the Michelson will be sensitive to gravitational waves. This is demonstrated in Figure 2.4, which shows the frequency response of the differential arm phase sensitivity to a gravitational wave for 4 km and 40 km long Michelson interferometers.

The nulls in the sensitivity curves result when the gravitational wave period (inverse of the frequency) is equal to the light storage time. Conceptually this is because the light experiences positive and negative phase shifts (equal in magnitude) from the trough and crest of the gravitational wave. Figure 2.4 shows the trade off between sensitivity and bandwidth (frequency range) that one needs to consider when designing a Michelson based gravitational wave detector.

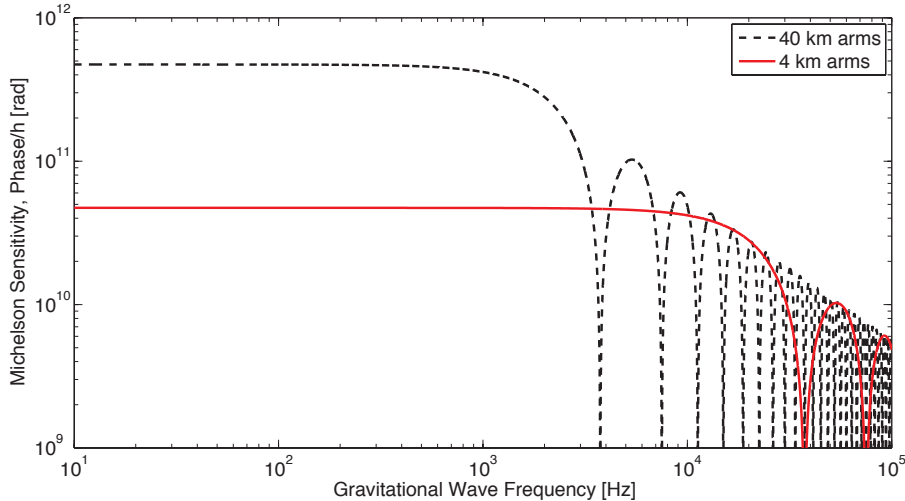


Figure 2.4: Sensitivity of the differential arm phase to a gravitational wave signal for Michelson interferometers with arm lengths of 4 km and 40 km.

Unfortunately for ground-based Michelson gravitational wave detectors, this trade-off can't be explored due to the complications that accompany an increase in the length of the arms, such as the cost of the vacuum system, finding the space and the curvature of the earth. This is one of the advantages that space-based interferometers possess. For ground-based detectors however, there is a simple method that increases the effective length of the Michelson arm, and that is to fold the arms over multiple times. This technique, referred to as an optical delay line [41], allows the light in the arms to interact with a gravitational wave longer, just as it would if the arms were considerably longer. This method is limited by scattering between the different paths [42]. Alternatively the beam can be folded back on itself, by using a Fabry-Perot cavity in the arms.

## 2.6 Fabry-Perot Cavity Enhancement

A Fabry-Perot cavity [43] is another type of interferometer that is just as, if not more important in ground-based gravitational wave detection, due to some important properties that allow it to enhance the sensitivity of the detector.

The Fabry-Perot cavity has a simple configuration, depicted in Figure 2.5, consisting of two parallel partially transmissive mirrors - the input mirror (IM) and the end mirror (EM). Light incident on the partially transmissive input mirror, is split into a promptly reflected beam and a leakage beam which then travels back and forth inside the cavity, gradually leaking back outside of the cavity as it encounters the two cavity mirrors. If the phase of the intra-cavity field reflected off the input mirror matches that of the incident field transmitted through the input mirror, then resonance occurs and the optical power builds up inside the cavity. This occurs when the roundtrip phase of the cavity  $\phi_{crt}$ , which is a function of the cavity length  $L$  and the optical wavelength  $\lambda$ , is an integer multiple of

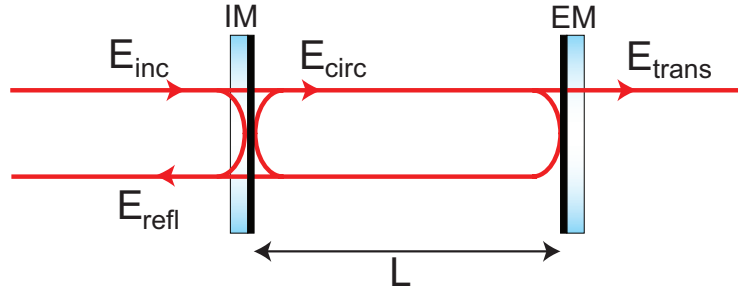


Figure 2.5: The optical fields of a Fabry-Perot cavity formed between two mirrors, the input mirror (IM) and the end mirror (EM).

$2\pi$ . More specifically:

$$\phi_{crt} = \frac{4\pi L}{\lambda} = 0 \pmod{2\pi} \quad (2.13)$$

The light field interacting with the cavity can be broken down into three optical fields - intra-cavity, reflected and transmitted. The intra-cavity or circulating field ( $E_{circ}$ ) is equal to the summation of the transmitted incident field and the circulating field after one roundtrip of the cavity. The reflected field ( $E_{refl}$ ) is equal to the instantly reflected incident field plus the circulating field that leaks back out through the input mirror. The transmitted field ( $E_{trans}$ ) is equal to the circulating field that is transmitted through the end mirror. The cavity response of each of these fields to the incident field ( $E_{inc}$ ) can be derived using a self consistent approach. The responses are:

$$F_{circ}^{sc} = \frac{E_{circ}}{E_{inc}} = \frac{t_{im}}{1 - r_{im}r_{em}e^{i\phi}} \quad (2.14)$$

$$F_{refl}^{sc} = \frac{E_{refl}}{E_{inc}} = \frac{r_{im} - r_{em}e^{i\phi}}{1 - r_{im}r_{em}e^{i\phi}} \quad (2.15)$$

$$F_{trans}^{sc} = \frac{E_{trans}}{E_{inc}} = \frac{t_{im}t_{em}e^{i\phi/2}}{1 - r_{im}r_{em}e^{i\phi}} \quad (2.16)$$

The amplitude and phase for each response is plotted in Figure 2.6 for the case of an under-coupled cavity ( $r_{im} > r_{em}$ ), an impedance matched cavity ( $r_{im} = r_{em}$ ) and an over-coupled cavity ( $r_{im} < r_{em}$ ).

In the reflected field response, it can be seen that on resonance the over-coupled response is  $\pi$ , whereas it is 0 for the under-coupled case and undefined for the impedance matched case. This  $\pi$  response is equivalent to a flip in the sign of the reflected field, which is an important effect in gravitational wave detectors.

The resonance condition of the cavity depends on the roundtrip phase. If it is an integer multiple of  $2\pi$  then the light will resonate. There are an infinite number of solutions or modes for the cavity. There are two parameters which can be controlled to meet this condition, the optical frequency  $\nu$  and the length of the cavity  $L$ . The free spectral range (FSR) is defined as the spacing between modes, which can be represented as a frequency

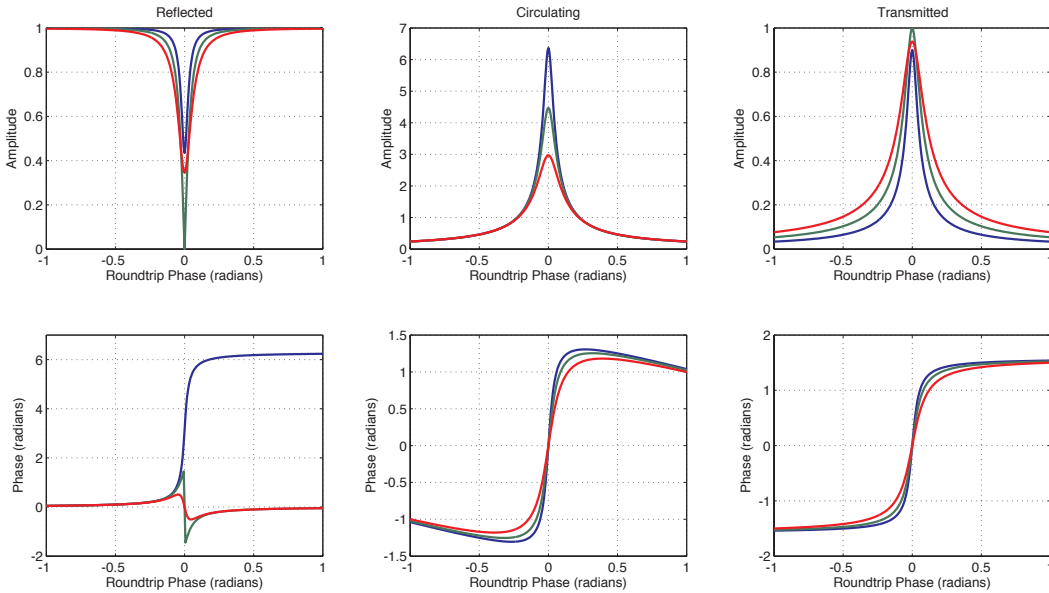


Figure 2.6: Plots for the cavity responses, for under-coupled (red), impedance matched (green) and over-coupled (blue) cavities. The top plots are for the amplitude response, the bottom plots are the phase response.

spacing or length spacing:

$$FSR_\nu = \frac{c}{2L} \quad (2.17)$$

$$FSR_L = \frac{\lambda}{2} \quad (2.18)$$

Another useful cavity parameter is the finesse  $\mathcal{F}$ , which is a measure of the sharpness of the resonance peaks, and is given in terms of the mirror reflectivities:

$$\mathcal{F} = \frac{\pi\sqrt{r_{im}r_{em}}}{1 - r_{im}r_{em}} \quad (2.19)$$

The line-width of the resonance peaks is defined as the full width at half maximum and is the ratio of the FSR and the finesse. Therefore the line-width in both frequency and displacement is given by:

$$\delta_\nu = \frac{c}{2L\mathcal{F}} \quad (2.20)$$

$$\delta_L = \frac{\lambda}{2\mathcal{F}} \quad (2.21)$$

Properties of the resonant Fabry-Perot cavity that make it useful in gravitational wave detection are its large optical storage time and its amplification of the light power within the cavity.

### 2.6.1 Arm Cavities

The phase of the Fabry-Perot reflected field is more sensitive to the cavity roundtrip phase near resonance than off resonance (where it is quite flat) as can be seen in Figure 2.6. Also

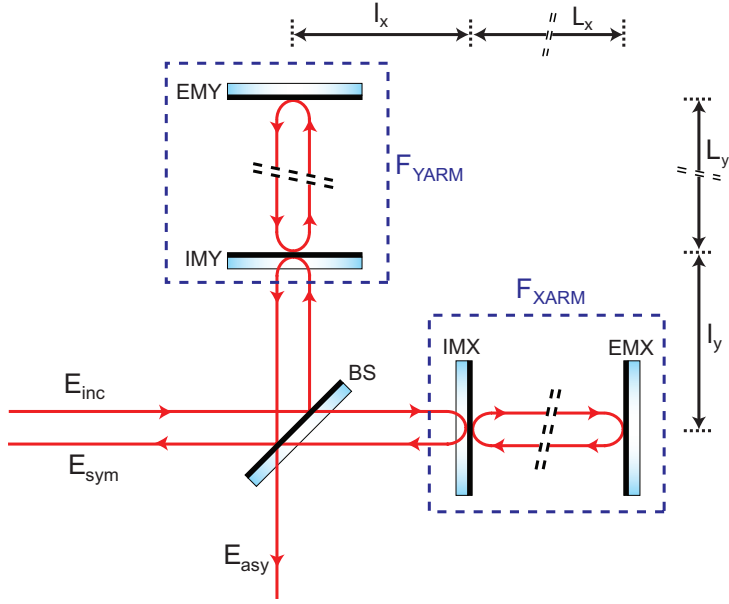


Figure 2.7: The optical fields of a Michelson interferometer with arm cavities. The arm cavities can be treated as compound mirrors with complex reflectivities  $F_{xarm}$  and  $F_{yarm}$ .

the reflected field phase is approximately linearly dependent on the arm cavity roundtrip phase. For an over-coupled cavity, the reflected phase near resonance can therefore be approximated by the linear equation:

$$\Phi_{refl} = \kappa\phi_{crt} + \pi \quad (2.22)$$

where the addition of  $\pi$  is due to this over-coupling and  $\kappa$  is the on resonance reflected field to cavity phase response, which is dependent on the reflectivities of the cavity mirrors.

$$\kappa = \frac{r_{em}(1 - r_{im}^2)}{(r_{em} - r_{im})(1 - r_{im}r_{em})} \quad (2.23)$$

By introducing a resonant Fabry-Perot cavity in each arm the gravitational wave sensitivity of the detector can be enhanced. Figure 2.7 shows the basic layout of a Michelson enhanced with Fabry-Perot cavities in each arm. The compound mirror approach, is where an interferometer (Fabry-Perot cavity or Michelson) is treated as a mirror with complex reflectivity and complex transmissivity.

Treating the resonant arm cavities as compound mirrors, the complex reflectivities are given by:

$$F_{xarm} = -Ae^{i\kappa\Phi_x} \quad (2.24)$$

$$F_{yarm} = -Ae^{i\kappa\Phi_y} \quad (2.25)$$

where  $A$  is the amplitude reflectivity. The negative sign is due to the over-coupled nature of the cavities. Substituting these compound mirror reflectivities into Equation 2.5

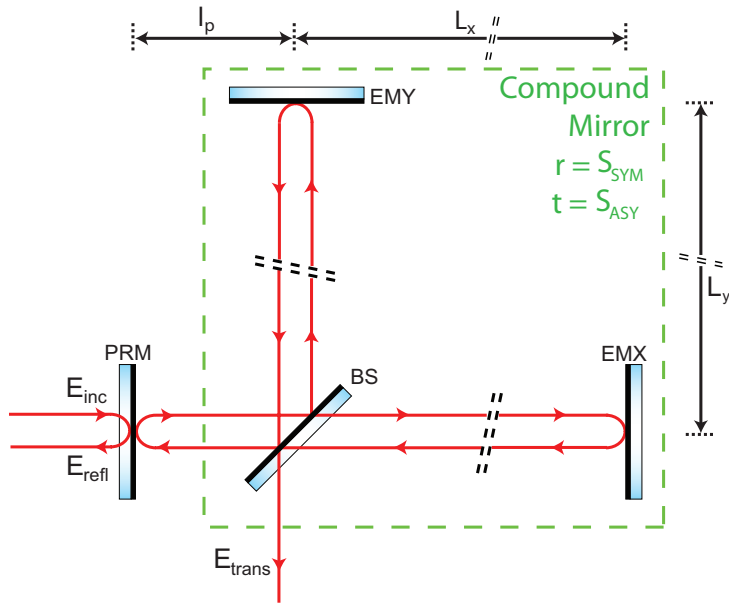


Figure 2.8: The optical fields of a power recycled Michelson interferometer.

and Equation 2.6 and changing to a common and differential mode representation, the symmetric and asymmetric responses of the resonant Fabry-Perot Michelson are given by:

$$F_{sym}^{fpm} = Ae^{i(\kappa\Phi_+ + \phi_+)} \cos(\kappa\Phi_- + \phi_-) \quad (2.26)$$

$$F_{asy}^{fpm} = Ae^{i(\kappa\Phi_+ + \phi_+)} i \sin(\kappa\Phi_- + \phi_-) \quad (2.27)$$

where  $\Phi_+ = \frac{\Phi_x + \Phi_y}{2}$  and  $\Phi_- = \frac{\Phi_x - \Phi_y}{2}$  are the common and differential arm phase respectively. The common phase between the short Michelson arms is given by  $\phi_+ = \frac{\phi_x + \phi_y}{2}$  and the differential phase between the short Michelson arms is given by  $\phi_- = \frac{\phi_x - \phi_y}{2}$ .

The roundtrip to field phase response  $\kappa$ , is what amplifies the detectors response to the gravitational wave. In the low frequency limit, the Fabry-Perot Michelson interferometer can be thought of as having an effective arm length given by  $L_{\text{eff}} = \kappa L$ .

## 2.6.2 Power Recycling

The shot noise limited sensitivity of an interferometric gravitational wave detector is most sensitive at or very near a point where the asymmetric port is dark [39]. As such interferometric gravitational wave detectors are held in a configuration where the light returning from the two arms, interferes destructively at the asymmetric port. Consequently, constructive interference occurs at the symmetric port, and all the light heads back towards the laser where it can no longer contribute to the shot noise limited sensitivity of the interferometer.

Effectively the Michelson acts as a highly reflective mirror, and by placing a partially transmissive mirror before the beam-splitter a cavity can be formed. Matching the loss of this mirror with the losses of the the interferometer and positioning the mirror so that resonance occurs, the circulating power inside this cavity can be optimised, giving

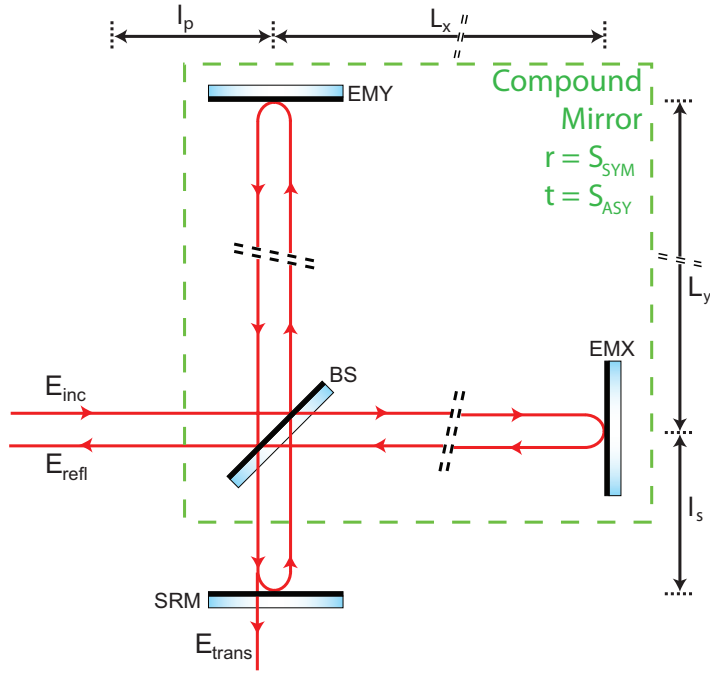


Figure 2.9: The optical fields of a signal recycled Michelson interferometer.

maximum power in the Michelson. The technique is referred to as power recycling [44, 45, 46], the basic layout of which can be seen in Figure 2.8. The power recycling gain is given by:

$$\kappa_{pr} = \frac{t_{prm}}{1 - r_{prm} \frac{A}{2}} \quad (2.28)$$

The shot-noise limited sensitivity of a Michelson scales with the square root of the power incident on the beam splitter (see Equation 2.12) and therefore power recycling enhances the signal to noise ratio by the square root of the power recycling gain.

### 2.6.3 Signal Recycling

The gravitational wave interacting with the arms can be thought of as creating modulation sidebands on the light at the signal frequency, which constructively interfere at the asymmetric port. A mirror placed at the asymmetric port, and held at the right position with the right reflectivity, can reflect the gravitational wave signal back into the interferometer where it constructively interferes with the new modulations. This technique is commonly referred to as signal recycling [45, 47, 48].

There are two configurations for the signal recycling cavity - broadband and narrowband. The broadband configuration uses a signal recycling mirror with lower reflectivity, which ensures a larger frequency response to the gravitational wave. This configuration is desirable when trying to detect gravitational waves of unknown frequency, such as those from binary coalescence, supernovae and stochastic sources. For this configuration the signal recycling cavity is resonant with the carrier (non-detuned).

The narrowband configuration uses a signal recycling mirror with higher reflectivity,

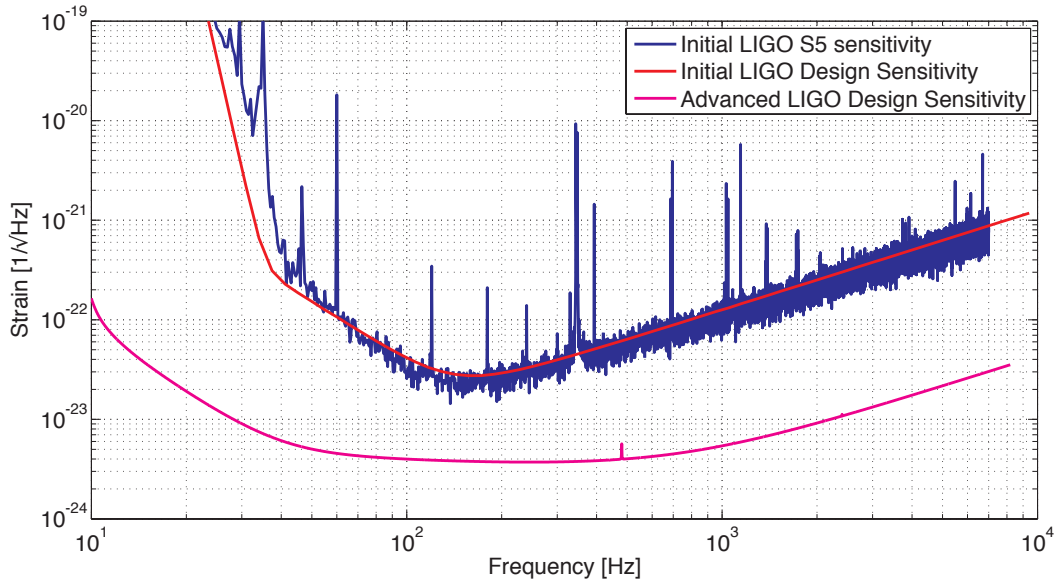


Figure 2.10: The design sensitivities for Initial and Advanced LIGO, and the achieved sensitivity for Initial LIGO during the fifth science data run (S5).

which gives a smaller bandwidth to the gravitational wave signal, but a much higher recycling gain and therefore signal to noise ratio. This configuration is desirable when detecting a gravitational wave of known frequency such as those from a Pulsar. In this configuration the signal recycling cavity needs to be detuned from the carrier, and made resonant with the gravitational wave modulation sidebands.

## 2.7 LIGO

As part of the LIGO Scientific Collaboration (LSC), our research is carried out with applicability to the LIGO detectors our main motivation. However the core architecture and technologies are largely the same for all the ground-based interferometric detectors and the work in this thesis is also applicable to other detectors.

LIGO is a network of three interferometric Gravitational Wave detectors constructed by the Californian Institute of Technology and the Massachusetts Institute of Technology with the support of the US National Science Foundation, located at two sites in the U.S. The first site at Hanford, Washington, is home to a 4km long detector (H1) and a 2km detector<sup>2</sup> (H2), whereas the second site at Livingston, Louisiana, has one 4km detector (L1) [21].

The LIGO detectors are currently undergoing upgrades to increase sensitivity by an order of magnitude in the LIGO detection band. At first this seems like a modest improvement, however it equates to a detection volume of space 1000 times larger. We refer to the LIGO instrument prior to the upgrades as Initial LIGO, whereas the instrument

<sup>2</sup>For Advanced LIGO this second detector will be upgraded to a 4 km interferometer, and possibly be moved to India (pending a final decision from the National Science Foundation)

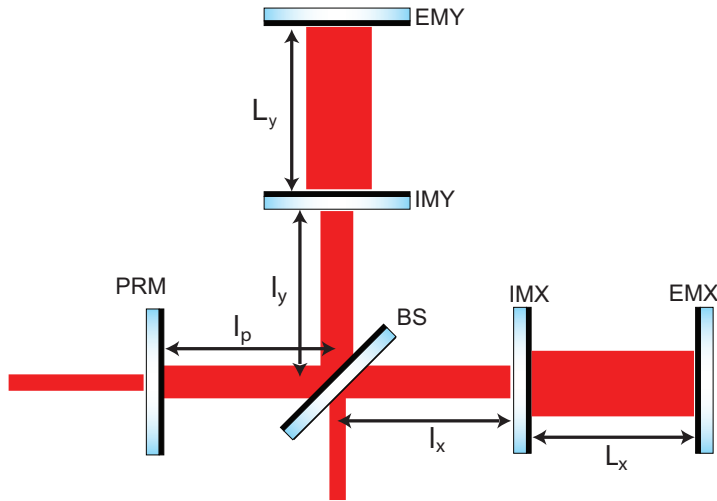


Figure 2.11: The Initial LIGO architecture - a power recycled Michelson interferometer with arm cavities

after the detector upgrades is referred to as Advanced LIGO [26]. In this final section of the chapter, a brief description of Initial LIGO is given, followed by a description of some of the upgrades of Advanced LIGO. The predicted improvement in sensitivity across the detection frequency band of Advanced LIGO is shown in Figure 2.10 [49, 50].

### 2.7.1 Initial LIGO

The Initial LIGO detector was a power-recycled Michelson with arm cavities, as depicted in Figure 2.11. Each core optic (EMs, IMs, BS and RM) was suspended as a pendulum by a single loop of steel wire, as shown in Figure 2.12(a). The length of the pendulum was set to give a pendulum mode resonance of approximately 0.75 Hz [51]. For frequencies above the resonance frequency, the pendulum attenuates the seismic motion by a factor of  $\left(\frac{0.75 \text{ Hz}}{f}\right)^2$ .

Furthermore, each pendulum structure was mounted to a stack of four alternating mass spring layers [52], as shown in Figure 2.12(b). Each mass spring layer provided an extra attenuation factor proportional to  $f^{-2}$  above the mechanical resonances of the springs. Therefore the total attenuation factor was proportional to  $f^{-10}$ . This level of attenuation was enough to reduce the seismic motion to the Initial LIGO S5 sensitivity shown in Figure 2.10 (below 40 Hz).

The science laser was an Nd:YAG laser, frequency stabilised to a temperature controlled reference cavity, and also intensity stabilised. The laser produced light with an optical wavelength of  $\lambda = 1064 \text{ nm}$  at a power of 10W. This power is reduced to 6W at the input to the recycling mirror, due to light loss at the various input optics such as the input mode cleaner which is a three mirror ring cavity responsible for spatially filtering the laser light[53].

For the detector to reach maximum sensitivity, the arm cavities and power recycling

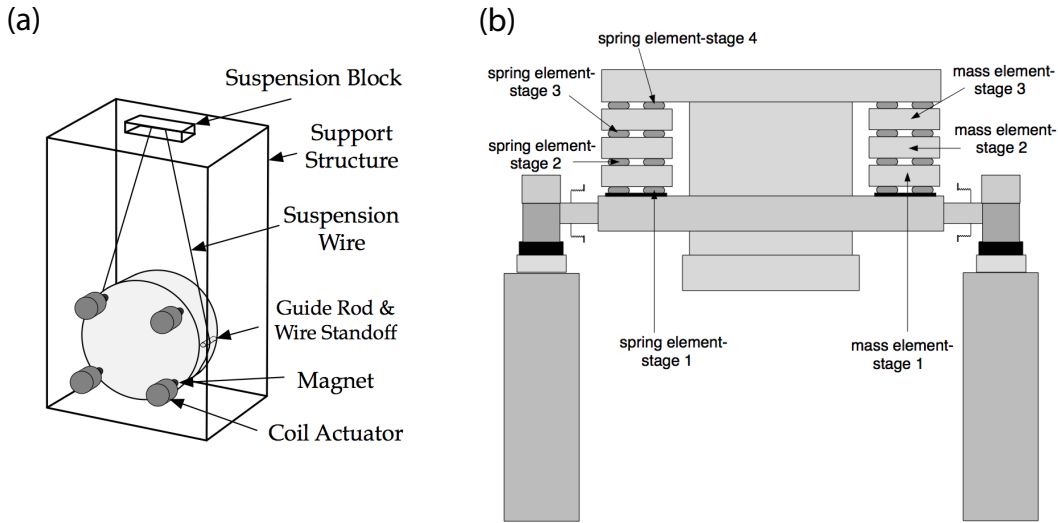


Figure 2.12: Schematics of (a) the suspended core optic for Initial LIGO, showing the four coil-magnet actuators and (b) the seismic isolation system for Initial LIGO, showing the four mass-spring layers of the passive stack.

cavity need to be resonant with the 1064nm light, and the Michelson held so that the asymmetric port is dark. For Initial LIGO the finesse of the arm cavities is approximately 210 [54], and therefore from Equation 2.21, the line width of the cavity is about 2.5 nm.

Within the gravitational wave detection band ( $>40\text{Hz}$ ), the motion of the mirrors is much less than the line-width of the cavity. However due to the amplification of anthropogenic noise by the passive stack resonances (between 1.5 and 12 Hz) and the suspension resonance (0.75 Hz) and also due to the lack of isolation from seismic disturbances such as the ocean induced double frequency microseism ( $\sim 0.15\text{Hz}$ ), the RMS (root mean squared) motion of the mirrors is considerably more than this ( $\sim 1\mu\text{m}$ ). Therefore the arm cavities, left uncontrolled, would swing through multiple resonances.

To hold the mirrors at their required operating points, feedback control systems [55] were utilized. This involved sensing the power recycled Michelson's degrees of freedom using heterodyne techniques (discussed in Chapter 3), and producing correction signals which were then fed back to the mirror actuators.

A force was applied to the mirror via electromagnetic actuators, made up of inductor coils surrounding magnets that were glued to the back of the mirrors. Each mirror had four of these coil-magnet actuators, which along with position control, allowed for the mirror to be controlled in pitch and yaw. The maximum force that these actuators could apply to the test masses was  $\sim 25\text{ mN}$  [56]. These electromagnetic actuators are quite invasive and are known to introduce noise sources [57, 58], the most noteable source being Barkhausen noise [59].

It should be noted that if the range of the coil magnet actuators is less than the seismic noise, than they will not be able to hold the arm cavities on resonance. In the earlier science runs, at Livingston during the daytime hours, this was the case. Two schemes

were implemented to improve the Livingston duty cycle. Both involved actuating on the end passive stack support positions (in the direction of the arms) using the long range fine actuation system, which had been installed to correct for the tidal induced motions. The velocity of the support structure was sensed and fed back to reduce the motion at the first two passive stack resonances. The ground motion was also sensed using highly sensitive seismometers and fed forward to the fine actuators to reduce the microseism disturbance to the mirrors [60].

The five degrees of freedom as seen in Figure 2.11 are  $\Phi_x$ ,  $\Phi_y$ ,  $\phi_x$ ,  $\phi_y$ , and  $\phi_p$ . However three of the DOFs can be reduced to two, leaving four in total. Here we will adopt the LIGO terminology, and define the degrees of freedom in terms of CARM (Common Arm), DARM (Differential Arm), MICH (Michelson) and PRCL (Power Recycling Cavity Length), the phase of these four degrees of freedom in terms of the original five are given below:

$$\Phi_{darm} = \frac{\Phi_x - \Phi_y}{2} \quad (2.29)$$

$$\Phi_{carm} = \frac{\Phi_x + \Phi_y}{2} \quad (2.30)$$

$$\phi_{mich} = \frac{\phi_x - \phi_y}{2} \quad (2.31)$$

$$\phi_{prcl} = \phi_p + \frac{\phi_x + \phi_y}{2} \quad (2.32)$$

By sensing and controlling these four degrees of freedom the interferometer could be held at the required operating point for optimal sensitivity. A heterodyne technique for sensing these four degrees of freedom is discussed in Section 3.4.

### 2.7.2 Advanced LIGO

For the Advanced LIGO detector upgrade, a signal recycling mirror will be installed at the asymmetric port, making the instrument a dual-recycled Michelson with arm cavities as shown in Figure 2.13. An extra degree of freedom, referred to as SRCL (Signal Recycling Cavity Length), needs to be controlled. The phase of SRCL is defined as:

$$\phi_{srcl} = \phi_s + \frac{\phi_x + \phi_y}{2} \quad (2.33)$$

The seismic isolation systems are also being upgraded to increase the instrument's detection band ( $>10$  Hz). Each core optic will now be suspended from multistage pendulums. The arm cavity input and end mirrors will be suspended from quadruple pendulums whereas the beam splitter and recycling mirrors will be suspended from triple suspensions. In this section we'll focus only on the seismic isolation of the arm cavity mirrors as they are of most concern to the topic of this thesis, and from here on we will refer to these mirrors as test masses.

Each quadruple suspension is mounted to an in-vacuum two-stage six-degree-of-freedom active isolation platform, which in turn is supported by an external six-degree-of-freedom hydraulic actuation stage [61]. A solidworks diagram of the total seismic isolation system

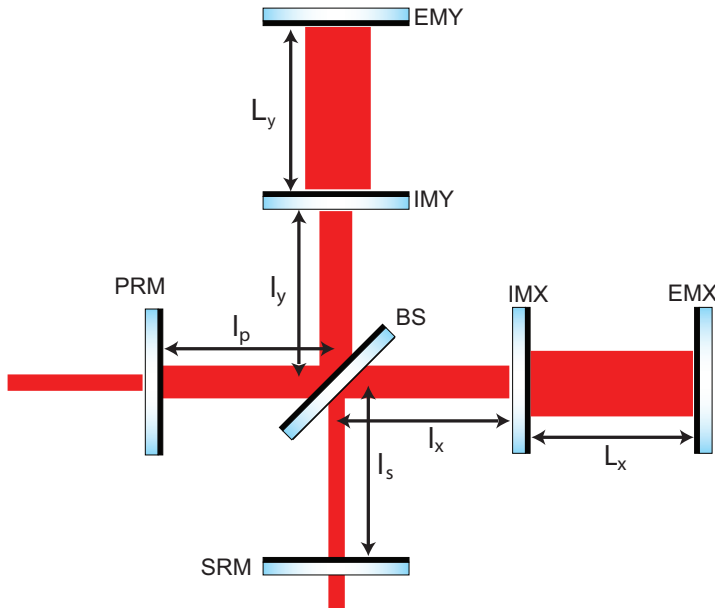


Figure 2.13: The Advanced LIGO architecture - a dual recycled Michelson interferometer with arm cavities

for the test mass can be seen in Figure 2.14, along with the main components [62]. The two stages of the internal seismic isolation (ISI) platform combined with the four stages of the quadruple pendulum, give an attenuation factor proportional to  $f^{-12}$  above the resonance frequencies of the suspensions stages and the platform stages. These resonance frequencies are approximately an order of magnitude less than that of the Initial LIGO passive stack. Therefore the seismic noise of the test masses in Advanced LIGO roll off earlier and faster than in Initial LIGO. This can be seen in Figure 2.15, which shows the approximate displacement noise of the test mass [63].

The electromagnetic actuators of Initial LIGO are being replaced with less invasive electrostatic actuators. These less invasive actuators are also considerably weaker than the electromagnetic actuators, with a maximum force of  $100 \mu\text{N}$  [64], which presents difficulties in lock acquisition (discussed in Chapter 5).

Other changes include an increase in laser power to 165W and an increase in the finesse of the arm cavities by about a factor of 2. This gives a line-width of about 1 nm. The RMS motion of the mirror is approximately  $0.1 \mu\text{m}$  (calculated from Figure 2.15). Therefore the RMS motion is approximately 2 orders of magnitude more than the line-width of the arm cavity and as such the various cavities still need to be locked.

A heterodyne sensing scheme will still be used to readout the various degrees of freedom, except for the gravitational wave readout (DARM) which will use a homodyne sensing scheme commonly referred to as ‘DC readout’ which will be discussed at the end of Chapter 3.

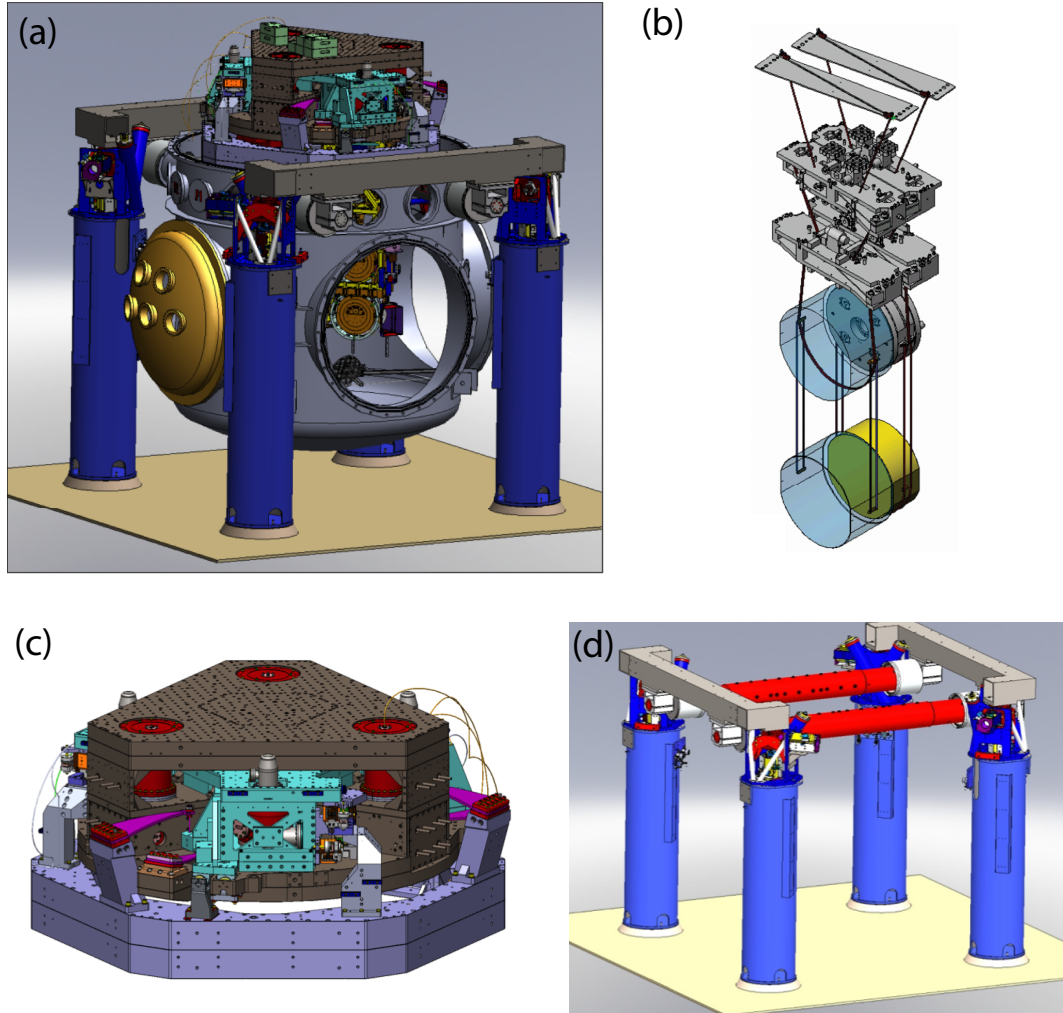


Figure 2.14: Solidworks drawings of (a) the total seismic isolation setup for the test mass (b) the quadruple suspension (c) the internal seismic isolation table and (d) the hydraulic external pre-isolator.

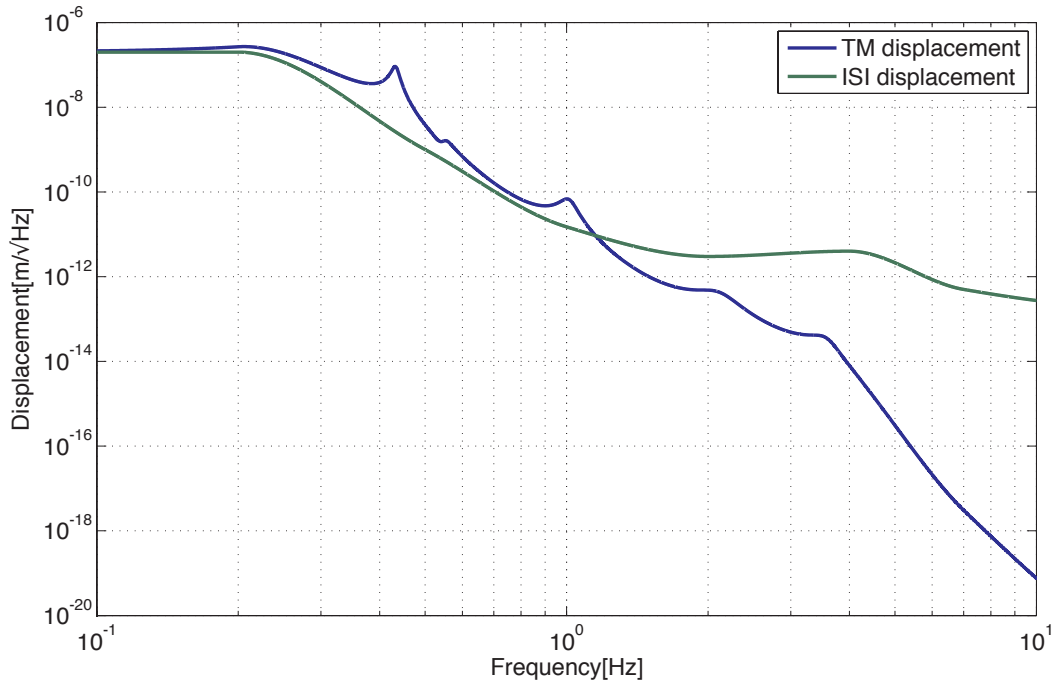


Figure 2.15: The modeled displacement noise for an Advanced LIGO test mass (TM) and also the internal seismic isolation (ISI) platform.

## 2.8 Summary

This chapter has given an overview on gravitational waves, including the theory behind their predicted existence and a description of some of the expected astronomical and cosmological sources. This was followed by a brief description of the techniques that have been used in a global effort to detect them.

The rest of the chapter was devoted to ground-based interferometric gravitational wave detection, looking at a Michelson interferometer as a gravitational wave detector, its limitations and the use of Fabry-Perot cavities to enhance sensitivity. The chapter ended with a closer look at the current long baseline detector - LIGO, which included a description of Initial LIGO and some of the planned upgrades for Advanced LIGO.

# Chapter 3

## Interferometric Sensing Techniques

The motivation for the inclusion of this chapter is twofold. The first motivation is to provide the reader with sufficient background into the interferometric sensing techniques used to extract information about the various degrees of freedom of a gravitational wave detector from the optical fields used to probe them. This is important in gaining the sufficient insight into the lock acquisition problem and hence the need for an Arm Length Stabilisation system (both discussed in Chapter 5).

The second is to provide the necessary background of the sensing techniques used in the experimental work presented in this thesis, which are largely the same as those utilised in gravitational wave detection.

### 3.1 Heterodyne and Homodyne Interferometry

Consider a beam which has been used to probe some simple system, such as a mirror (shown in Figure 3.1). The motion of the mirror,  $x_m$ , is encoded onto the phase of the probe beam. The phase change due to the mirror motion is:

$$\Delta\phi_m = \frac{4\pi\Delta x_m}{\lambda} \quad (3.1)$$

To recover information about the displacement of the mirror, one simply has to measure the phase of the probe beam. However, unlike for radio or microwaves, measuring the phase of the oscillating electric field is not so trivial, due to the much more rapid rate at which it varies. For an optical beam with a wavelength of  $1\text{ }\mu\text{m}$ , the phase varies at a rate of  $3 \times 10^{14}$  cycles per second (Hz). There exists no device capable of measuring such a rapid variation of an electric field.

Heterodyne interferometry refers to a technique where such a probe beam is interfered on a photo-detector with another beam of similar frequency, commonly referred to as the local oscillator beam, to down-convert the wanted signal to a lower frequency (less than  $10^8$  Hz), in order to obtain the phase information via common signal processing techniques. The electric field at the photodetector,  $E_{pd}$  is given by:

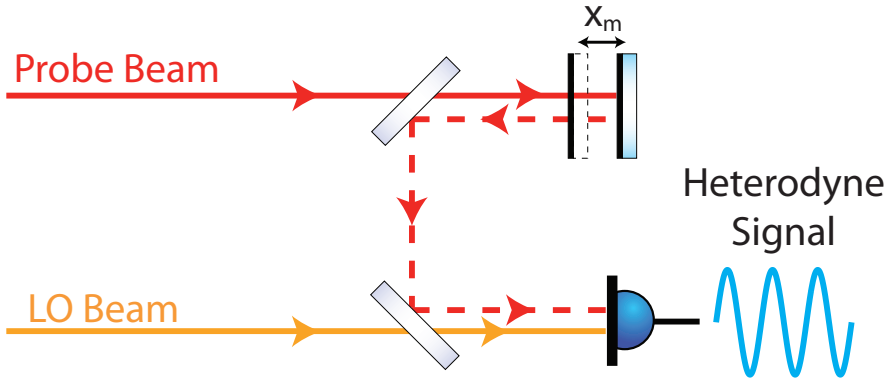


Figure 3.1: A common scheme for obtaining a heterodyne measurement of the phase of a system.

$$E_{pd} = E_{pro}e^{i(2\pi\nu_{pro}t+\phi_m)} + E_{lo}e^{i2\pi(\nu_{lo}t)} \quad (3.2)$$

where  $E_{pro}$  and  $E_{lo}$  are the electric fields of the probe and local oscillator beams, and  $\nu_{pro}$  and  $\nu_{lo}$  are their respective frequencies. A photo-detector is a device that converts incident light power into electrical current via the equation:

$$I_{pd} = \frac{\eta e}{h\nu} P_{pd} \quad (3.3)$$

where  $I_{pd}$  is the photo-current,  $P_{pd}$  is the optical power incident on the detector,  $\eta$  is the quantum efficiency,  $e$  the charge of an electron,  $h$  is Planck's constant and  $\nu$  is the optical frequency. This current is converted to a measurable voltage via a trans-impedance amplifier. The finer details of photo-detection won't be discussed here, instead the reader is referred to [65]. The power at the photodetector can be calculated using  $P_{pd} = |E_{pd}|^2$ , which yields:

$$P_{pd} = |E_{pro}|^2 + |E_{lo}|^2 + 2E_{pro}E_{lo} \cos(2\pi(\nu_{pro} - \nu_{lo})t + \phi_m) \quad (3.4)$$

The first two terms are time independent, whereas the third term oscillates at the difference frequency, which for the rest of this thesis we will refer to as the heterodyne or beat frequency:

$$\nu_h = \nu_{pro} - \nu_{lo} \quad (3.5)$$

The third term in Equation 3.4 carries the phase information of the system and can be isolated by AC coupling the photo-detector output. Using trigonometric identities the AC-coupled PD output is

$$P_{pd-ac} = 2E_{pro}E_{lo} \{ \cos(2\pi\nu_h t) \cos(\phi_m) - \sin(2\pi\nu_h t) \sin(\phi_m) \} \quad (3.6)$$

To simplify the analysis we will define in-phase and quadrature components:

$$\varepsilon_I = E_{pro}E_{lo} \cos(\phi_m) \quad (3.7)$$

$$\varepsilon_Q = E_{pro}E_{lo} \sin(\phi_m) \quad (3.8)$$

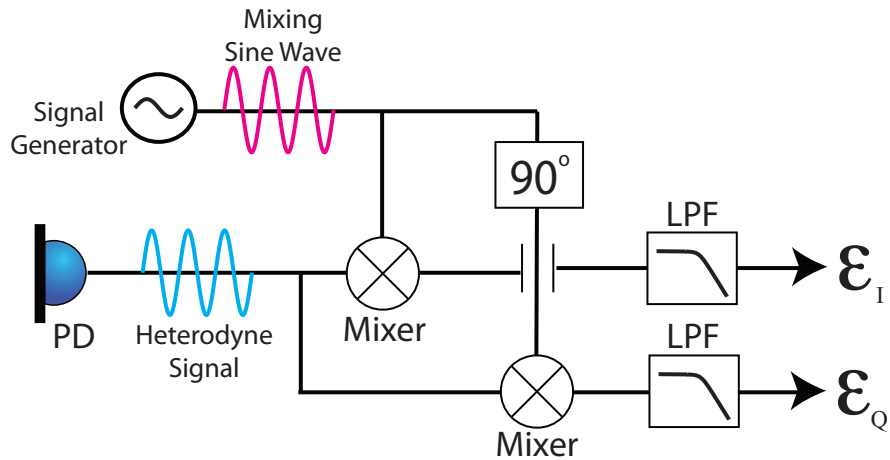


Figure 3.2: A scheme for obtaining the in-phase and quadrature components

The AC coupled photo-detector output in Equation 3.6 can be written in terms of these components:

$$P_{pd-ac} = 2\varepsilon_I \cos(2\pi\nu_h t) - 2\varepsilon_Q \sin(2\pi\nu_h t) \quad (3.9)$$

If the in-phase and quadrature components can be isolated, then the phase can be obtained via:

$$\phi_m = \arctan\left(\frac{\varepsilon_Q}{\varepsilon_I}\right) \quad (3.10)$$

The in-phase and quadrature terms can be isolated by electronically multiplying (mixing) the AC-coupled photo-detector output from Equation 3.9, with a sinusoid at the same frequency, (the heterodyne frequency  $\nu_h$ ). From convolution theory [66], a multiplication in the time domain is equivalent to a convolution in the frequency domain.

Effectively multiplication by this sine wave, results in the two terms in Equation 3.9 being up and down converted by the heterodyne frequency, yielding terms that oscillate at twice the heterodyne frequency ( $2\nu_h t$ ) as well as terms at baseband. The  $2\nu_h t$  terms can be eliminated by sending the output of the mixer through a low pass filter, leaving only the baseband terms.

For convenience, we'll assume that the AC-coupled photo-detector output is mixed with a cosine function with tunable phase,  $\theta_{mix}$ , before being sent through a low pass filter. Note that a cosine function is simply a sine function offset in phase by  $90^\circ$ . The output of the low pass filter is given by:

$$S = 2\varepsilon_I \cos(\theta_{mix}) + 2\varepsilon_Q \sin(\theta_{mix}) \quad (3.11)$$

Therefore by tuning the mixing phase, the in-phase and quadrature components or some combination of both can be recovered. A mixing phase of  $\theta_{mix} = 0^\circ$  will give the in-phase component only whereas a mixing phase of  $\theta_{mix} = 90^\circ$  will yield only the quadrature component. A scheme for obtaining both components is shown in Figure 3.2.

Equation 3.10 shows one way to obtain a readout of the phase,  $\phi_m$ . Alternatively, if  $\phi_m$  is small, the small angle approximation means that  $\varepsilon_Q$  is proportional to  $\phi_m$ , and will

be enough to deduce information about the mirror's motion.

$$\varepsilon_Q = E_{pro}E_{lo}\phi_m \quad (3.12)$$

One way to ensure that  $\phi_m$  is sufficiently small is to feed back the  $\varepsilon_Q$  measurement to the mixing phase, so as to create a control loop that suppresses the measurement and therefore also  $\phi_m$ . This idea is exploited in the phase-locked loop based frequency-meter, in Chapter 6.

Homodyne interferometry refers to a special case of heterodyne interferometry where the frequencies of the probe and local oscillator beams are equal, so that the desired signal is down-converted to baseband at the photo-detector. Substitution of  $\nu_{lo} = \nu_{pro}$  into Equation 3.4 gives:

$$P_{pd} = |E_{pro}|^2 + |E_{lo}|^2 + 2E_{pro}E_{lo}\cos(\phi_m) \quad (3.13)$$

Essentially a fluctuation in the phase  $\phi_m$  gives a direct change in the intensity of the light  $P_{pd}$  incident on the photodetector. The sensitivity of the power to phase is maximum half-way up the fringe, and zero at the maxima and minima.

Homodyne interferometry is commonly overlooked in favor of a heterodyne scheme due to the signal we are trying to detect being indistinguishable from laser intensity fluctuations.

## 3.2 Pound Drever Hall Readout of a Simple Cavity

The heterodyne scheme in Figure 3.1 can only read out the motion of one mirror, and is unsuitable for displacement readout of multiple optics (i.e. cavities). A derivative of the heterodyne technique is the Pound-Drever-Hall (PDH) technique [67, 68].

The PDH technique is the most common technique for sensing the roundtrip phase of a cavity. The light is sent through an electro-optic modulator [65], which consists of a Pockels crystal. A voltage applied across this crystal results in a change in its refractive index, and therefore also a change in the phase of the light passing through it. A time varying voltage then leads to a time varying phase shift of the optical field, an effect referred to as phase modulation.

For sinusoidal phase modulation with small modulation depth ( $\delta \ll 1$ ) the phase modulated field can be represented mathematically as:

$$E_{inc} = E_0 e^{i\omega_c t} \left[ 1 + \frac{\delta}{2} i \sin(\omega_m t) \right] \quad (3.14)$$

$$= E_0 e^{i\omega_c t} \left[ 1 + \frac{\delta}{2} e^{i\omega_m t} - \frac{\delta}{2} e^{-i\omega_m t} \right] \quad (3.15)$$

where  $\omega_c = 2\pi\nu_c$  is the carrier angular frequency and  $\omega_m = 2\pi\nu_m$  is the modulation angular frequency. From the super-position principle [69] the phase modulated field in Equation 3.15 can be decomposed into three optical fields, a carrier field  $E_c = E_0 e^{i\omega_c t}$ , an upper sideband field,  $E_{su} = +E_0 \frac{\delta}{2} e^{i(\omega_c+\omega_m)t}$  and a lower sideband field,  $E_{sl} = -E_0 \frac{\delta}{2} e^{i(\omega_c-\omega_m)t}$ .

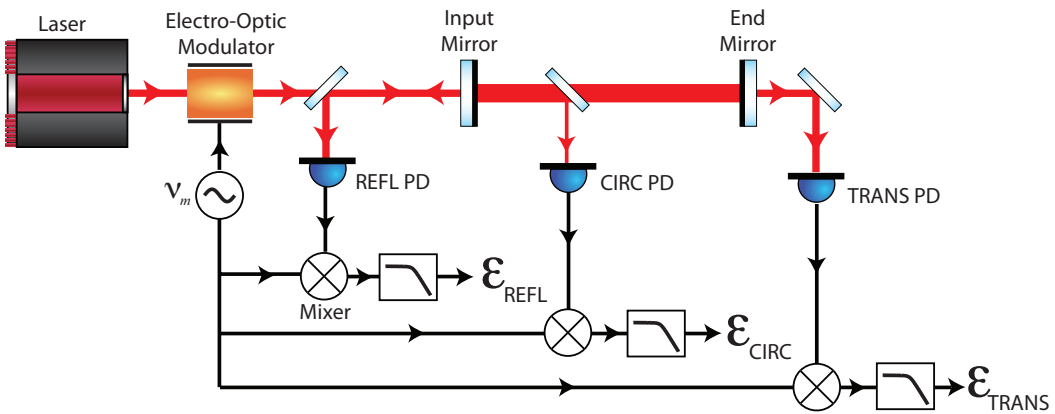


Figure 3.3: A Pound Drever Hall readout scheme for a Fabry-Perot cavity.

The optical frequencies of the sidebands are offset from that of the carrier by plus and minus the modulation frequency and therefore incur different cavity responses. It is here that the PDH technique can be considered a type of heterodyne technique, as the sidebands act as local oscillators to the carrier.

By picking off the modulated field after it has interacted with the cavity and shining it onto a photo-detector, a beat signal between the carrier and sidebands can be obtained. This beat signal can be demodulated and an error signal for the cavity roundtrip phase can be derived.

Consider the PDH readout scheme for a simple two mirror cavity in Figure 3.3. The cavity needs to be held on, or near resonance with the carrier beam as this is where the intra-cavity power builds up and the phase of the cavity fields are most sensitive to changes in cavity roundtrip phase.

Mathematically, the picked off modulated field is the multiplication of the modulated incident field with the complex transfer function,  $F_{port}$  for each component, i.e.

$$E_{port}^{sc}(\phi_c) = E_{inc} e^{i\omega_c t} \left[ F_{port}^{sc}(\phi_c) + F_{port}^{sc}(\phi_{su}) \frac{\delta}{2} e^{i\omega_m t} - F_{port}^{sc}(\phi_{sl}) \frac{\delta}{2} e^{-i\omega_m t} \right] \quad (3.16)$$

The roundtrip phase for the upper and lower sidebands are  $\phi_{su} = 2 [\omega_c + \omega_m] L/c$  and  $\phi_{sl} = 2 [\omega_c - \omega_m] L/c$  respectively. The pick off could be from the reflected beam, transmitted beam, or from within the cavity, in which case  $F_{port}$  is either the transfer function from the incident field to - the reflected field  $F_{refl}$ , the transmitted field  $F_{trans}$  or the circulating field  $F_{circ}$ .

Since a photodetector can only measure power, phase modulation can not be sensed directly. Upon interaction with the cavity some of this phase modulation is converted to amplitude modulation.

The optical power, given by  $P_{port} = E_{port}^* E_{port}$ , consists of components that don't oscillate (DC terms), components that oscillate at the modulation frequency ( $\omega_m$  terms), and components that oscillate at twice the modulation frequency ( $2\omega_m$  terms). The DC terms are the carrier and sideband fields multiplied by themselves. The  $2\omega_m$  terms are

the sidebands multiplied by their opposite sidebands. And the  $\omega_m$  terms are the carrier multiplied by the sidebands.

The  $\omega_m$  terms sample the cavity roundtrip phase most strongly. Just like for the heterodyne scheme in Section 3.1 the DC terms can be eliminated by AC coupling the photo-detector and the  $2\omega_m$  terms can be eliminated by sending the signal through a low pass filter, leaving the  $\omega_m$  terms. Therefore to simplify the analysis we will only look at the  $\omega_m$  terms. The  $\omega_m$  components of the optical power at the pick off are given by the following equation:

$$\begin{aligned} P_{port-\omega_m}(\phi_c) = & 2\sqrt{P_c P_s} (F_{port}^{sc}(\phi_c)^* F_{port}^{sc}(\phi_{su}) e^{i\omega_m t} - F_{port}^{sc}(\phi_c)^* F_{port}^{sc}(\phi_{sl}) e^{-i\omega_m t} \\ & + F_{port}^{sc}(\phi_c) F_{port}^{sc}(\phi_{su})^* e^{-i\omega_m t} - F_{port}^{sc}(\phi_c) F_{port}^{sc}(\phi_{sl})^* e^{i\omega_m t}) \end{aligned} \quad (3.17)$$

where  $P_c$  and  $P_s$  are the powers in the carrier and sidebands respectively (dependent on the modulation depth). The above equation can be manipulated using complex analysis to give:

$$P_{port-\omega_m}(\phi_c) = \varepsilon_{port-I}^{sc}(\phi_c) \cos(\omega_m t) + \varepsilon_{port-Q}^{sc}(\phi_c) \sin(\omega_m t) \quad (3.18)$$

Where  $\varepsilon_{port-I}^{sc}$  refers to the component in-phase with the real part of the complex term  $\varepsilon_{port}^{sc}$  and  $\varepsilon_{port-Q}^{sc}$  refers to the quadrature phase component (imaginary part) of  $\varepsilon_{port}^{sc}$ . The complex term  $\varepsilon_{port}^{sc}$  is given by:

$$\varepsilon_{port}^{sc}(\phi_c) = 2\sqrt{P_c P_s} (F_{port}^{sc}(\phi_c) F_{port}^{sc}(\phi_{su})^* - F_{port}^{sc}(\phi_c)^* F_{port}^{sc}(\phi_{sl})) \quad (3.19)$$

As in Section 3.1 the in-phase and quadrature components can be extracted by mixing the output of the photodetector with a sine wave oscillating at the same frequency (the modulation frequency). The mixing process results in the  $\omega_m t$  terms in Equation 3.18 being up-converted to  $2\omega_m t$  terms and also down-converted to base-band. The  $2\omega_m t$  terms are again eliminated by passing the mixer output through a low pass filter.

The phase  $\theta_{mix}$  of the mixing signal can be tuned, and the resulting demodulated signal is given by:

$$S_{port}^{sc}(\phi_c) = \varepsilon_{port-I}^{sc}(\phi_c) \cos(\theta_{mix}) + \varepsilon_{port-Q}^{sc}(\phi_c) \sin(\theta_{mix}) \quad (3.20)$$

The in-phase and quadrature components or a combination of both can therefore be obtained by tuning the electronic mixing phase. Figure 3.4 shows the in-phase and quadrature error signals for when the modulation sidebands are within the cavity line-width and for when they are outside it. If the modulation frequency is larger than the line-width of the cavity then the sidebands will be mostly reflected off the cavity, won't build up in the cavity nor transmit through it. This lack of sideband for the carrier to beat with is why the size of the transmitted and circulating error signals are much smaller than for when the modulation frequency is within the line-width.

Near resonance, the reflected error signal with the faster modulation frequency, is mostly imaginary when the carrier is resonant. This is because the carrier receives a

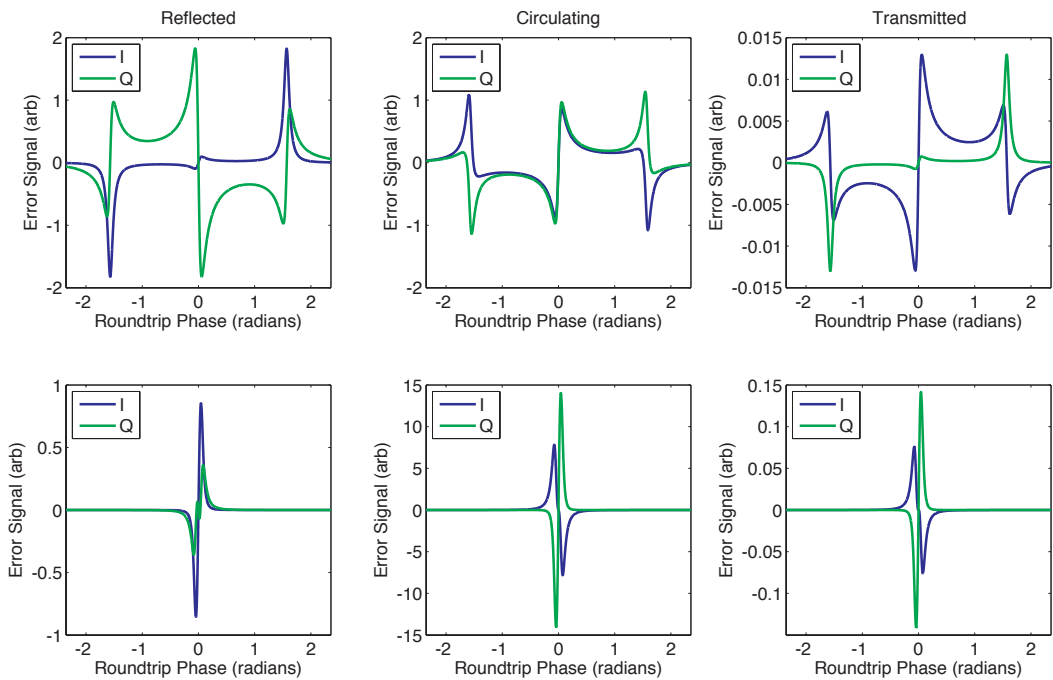


Figure 3.4: The in-phase (I) and quadrature (Q) error signals, for the reflected, circulating and transmitted pick-offs. Top row:  $\nu_m \gg HWHM$ . Bottom row:  $\nu_m = HWHM$

phase shift from the cavity, whereas the sidebands receive effectively none, meaning that the relative change between the carrier and sidebands is in phase and not amplitude.

When the sidebands lie inside the linewidth, the sidebands and carrier receive similar phase shifts from the cavity. The amplitude for the sidebands however is much larger than that for the carrier. Therefore the relative change between the carrier and sidebands is mostly in amplitude, hence the error signal is more real than imaginary near resonance.

There are 6 error signals, two quadratures for each of the three ports. They are all zero crossing for the cavity carrier roundtrip phase, some are more sensitive than others. The sensitivity depends mostly on the modulation frequency. Figure 3.5 shows the sensitivity of each error signal to the cavity roundtrip phase, when the cavity is carrier resonant. As can be seen, when the modulation frequency is much greater than the half width half maximum of the cavity, the imaginary reflected error signal is the most sensitive error signal.

### 3.3 Pound Drever Hall Readout of a Three Mirror Coupled Cavity

The PDH technique is capable of producing multiple error signals from one modulation, essentially two for every port. Therefore, in theory multiple degrees of freedom can be read out. To see how this works we will consider a PDH readout scheme for a three mirror coupled cavity where there are two degrees of freedom that need to be controlled. Figure 3.6 shows this scheme, where the reflected port and a pickup from first cavity are

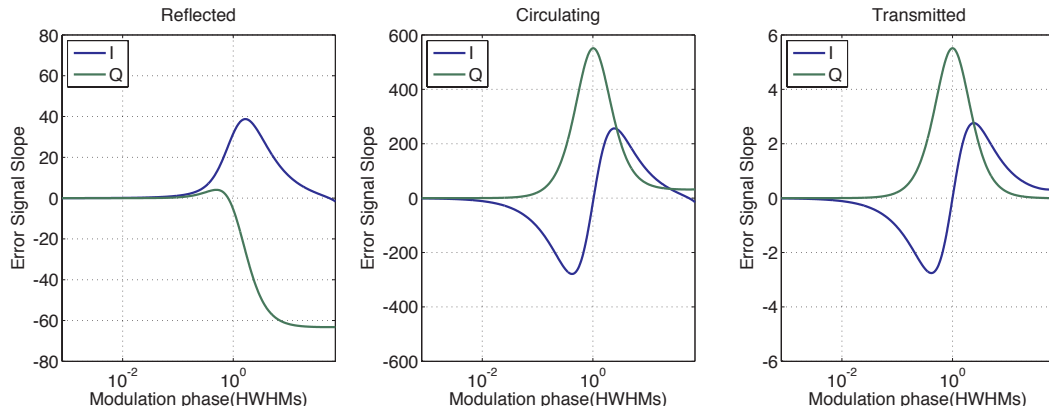


Figure 3.5: The sensitivity of the error signal to the cavity roundtrip phase on resonance as a function of the modulation frequency.

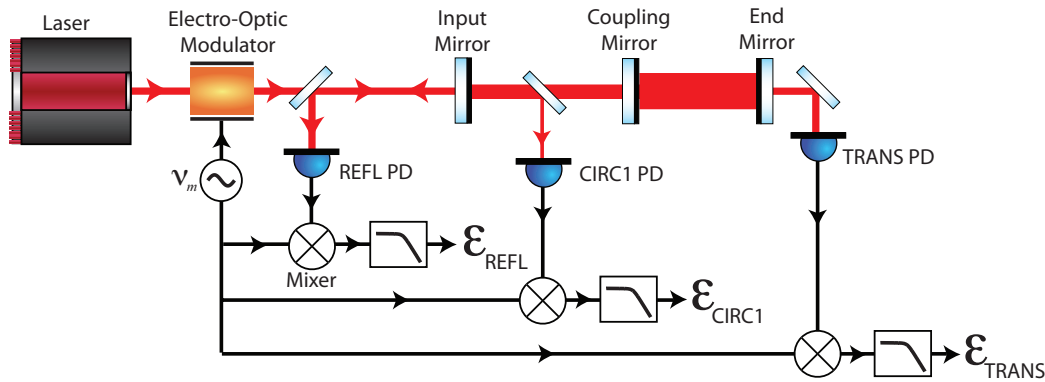


Figure 3.6: Pound Drever Hall readout scheme for a three mirror coupled cavity.

used, to derive the error signals.

Just as for the single cavity case the light fields interacting with a three-mirror cavity can be broken down into reflected, transmitted and intra-cavity fields, however here there are two intra-cavity fields (one for each cavity). The responses of these fields to the incident field can be derived using a compound mirror approach and are given below:

$$F_{refl}^{cc}(\phi_1, \phi_2) = \frac{r_{im}(1 - r_{cm}r_{em}e^{i\phi_2}) + (r_{cm} - r_{em}e^{i\phi_2})e^{i\phi_1}}{1 + r_{im}r_{cm}e^{i\phi_1} - r_{cm}r_{em}e^{i\phi_2} - r_{im}r_{em}e^{i(\phi_1+\phi_2)}} \quad (3.21)$$

$$F_{circ1}^{cc}(\phi_1, \phi_2) = \frac{t_{im}(1 - r_{cm}r_{em}e^{i\phi_2})}{1 + r_{im}r_{cm}e^{i\phi_1} - r_{cm}r_{em}e^{i\phi_2} - r_{im}r_{em}e^{i(\phi_1+\phi_2)}} \quad (3.22)$$

$$F_{circ2}^{cc}(\phi_1, \phi_2) = \frac{t_{im}t_{cm}e^{i\phi_1/2}}{1 + r_{im}r_{cm}e^{i\phi_1} - r_{cm}r_{em}e^{i\phi_2} - r_{im}r_{em}e^{i(\phi_1+\phi_2)}} \quad (3.23)$$

$$F_{trans}^{cc}(\phi_1, \phi_2) = \frac{t_{im}t_{cm}t_{em}e^{i(\phi_1+\phi_2)/2}}{1 + r_{im}r_{cm}e^{i\phi_1} - r_{cm}r_{em}e^{i\phi_2} - r_{im}r_{em}e^{i(\phi_1+\phi_2)}} \quad (3.24)$$

It is obvious from these four cavity field responses, why the cavity is referred to as ‘coupled’. Each field response is a function of the roundtrip phase of both cavities,  $F^{cc}(\phi_1, \phi_2)$ .

The electric field at each port can be derived in the same way as for Equation 3.16:

$$E_{port}^{cc} = E_{inc} e^{i\omega_c t} \left[ F_{port}^{cc}(\phi_{c1}, \phi_{c2}) + F_{port}^{cc}(\phi_{su1}, \phi_{su2}) \frac{\delta}{2} e^{i\omega_m t} - F_{port}^{cc}(\phi_{sl1}, \phi_{sl2}) \frac{\delta}{2} e^{-i\omega_m t} \right] \quad (3.25)$$

Carrying out the same analysis as in the previous section, a complex error signal term that is dependent on the roundtrip phase of both cavities, can be derived for each port:

$$\varepsilon_{port}^{cc}(\phi_{c1}, \phi_{c2}) = F_{port}^{cc}(\phi_{c1}, \phi_{c2}) F_{port}^{cc}(\phi_{su1}, \phi_{su2})^* - F_{port}^{cc}(\phi_{c1}, \phi_{c2})^* F_{port}^{cc}(\phi_{sl1}, \phi_{sl2}) \quad (3.26)$$

Remembering that each error signal term is made up of two isolatable quadratures, then for the three port example in Figure 3.6, there are in theory six error signals from which we can retrieve our two cavity phase readouts.

Of course there are configurations where these error signals would be insensitive to one or both cavities. In this regard the choice of the modulation frequency and cavity lengths is crucial, as they are the properties that decide the sideband resonance condition in both cavities in relation to the carrier resonance condition.

For example through the right choice of modulation frequency and cavity lengths, the sidebands can be made resonant in the first cavity, and anti-resonant in the second cavity, when the carrier is resonant in both.

This ensures that the sideband is interacting with the second cavity, and will result in the reflected and pick-off port error signals being sensitive to fluctuations in both cavities when the carrier is resonant. This relationship can be represented by a system of linear equations, shown in the matrix equation below.

$$\begin{bmatrix} \Delta\varepsilon_{refl}^{cc} \\ \Delta\varepsilon_{circ1}^{cc} \end{bmatrix} = \begin{bmatrix} S_{1 \rightarrow refl} & S_{2 \rightarrow refl} \\ S_{1 \rightarrow circ1} & S_{2 \rightarrow circ1} \end{bmatrix} \begin{bmatrix} \Delta\phi_1 \\ \Delta\phi_2 \end{bmatrix} \quad (3.27)$$

$$\vec{\Delta\varepsilon} = \mathbf{S} \vec{\Delta\Phi} \quad (3.28)$$

The matrix  $\mathbf{S}$  in the above equation is referred to as the sensing matrix. Providing this matrix is invertible, it can be diagonalized, yielding an input matrix  $\mathbf{M}$  which can be used to obtain isolated measurements of the two degrees of freedom, i.e.

$$\vec{\Delta\Phi} = \mathbf{M} \vec{\Delta\varepsilon} \quad (3.29)$$

Here we have shown that the PDH technique, utilising one set of modulation sidebands, allows for the readout of multiple degrees of freedom. The limitation to the number of degrees of freedom that can be read-out is ultimately decided by the number of light pick-offs from different parts of the coupled cavity system.

## 3.4 Initial LIGO Readout

In this section we describe the frontal modulation scheme [70, 71, 72] used for the readout of the Initial LIGO degrees of freedom. The optimum sensitivity for a power-recycled

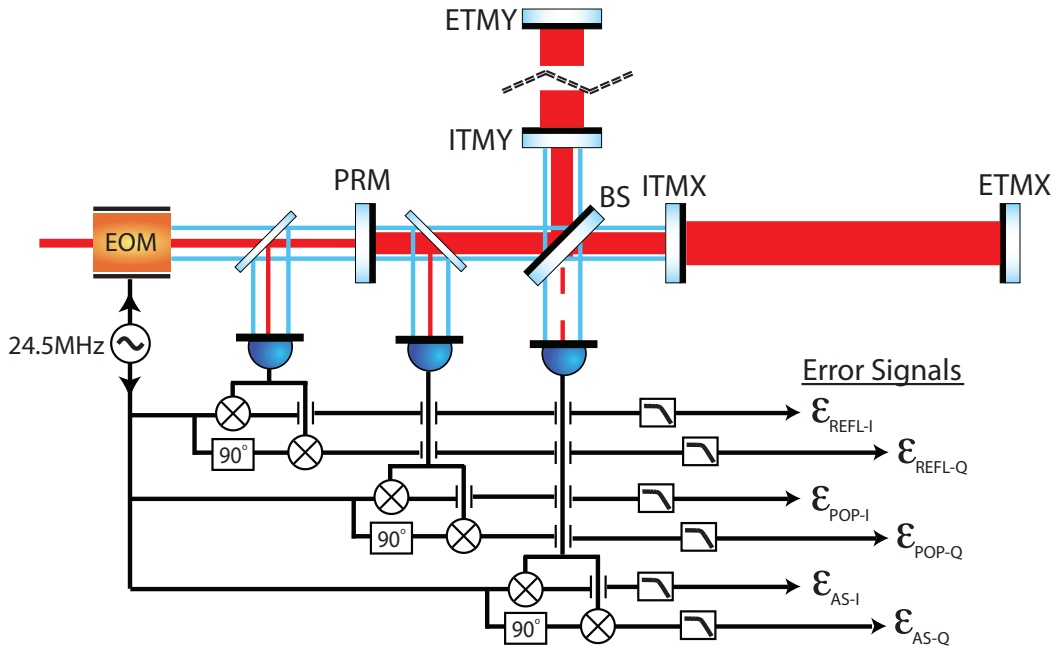


Figure 3.7: The readout scheme for the Initial LIGO detector.

interferometer occurs when the arm cavities and power recycling cavity are held on resonance with the carrier, and the asymmetric (or transmitted) port of the Michelson is held on a dark fringe.

Mathematically this is the same as requiring that the phases of the four degrees of freedom, CARM, DARM, MICH and PRCL, equals zero modulo  $2\pi$ , i.e.

$$\Phi_{DARM} = 0 \pmod{2\pi} \quad (3.30)$$

$$\Phi_{CARM} = 0 \pmod{2\pi} \quad (3.31)$$

$$\phi_{MICH} = 0 \pmod{2\pi} \quad (3.32)$$

$$\phi_{PRCL} = 0 \pmod{2\pi} \quad (3.33)$$

To ensure that this condition is met these degrees of freedom need to be read out and fed back to the mirror actuators. In the previous section the PDH technique was extended to a system with two degrees of freedom and here it is extended to obtain readouts of the four Initial LIGO degrees of freedom.

The LIGO readout problem involves finding a vector of four suitable error signals, that are a function of these four degrees of freedom, i.e. the sensing matrix needs to be realisable and diagonalisable. The interaction of the modulation sidebands with the various cavities during carrier resonance is what ultimately determines this. As in the previous section, the choice of modulation frequency and cavity lengths are crucial here.

A simplified diagram of the PDH readout scheme adopted for Initial LIGO is shown in Figure 3.7. The modulation sidebands are imposed onto the science beam at a frequency of 24.5 MHz.

There are three ports of which the error signals are derived from - the reflected port

(REFL), a pick-off from the power recycling cavity (POP) and the asymmetric port (AS). Therefore there are in theory six error signals from which readouts of the four degrees of freedom can be constructed from.

The modulation frequency and the average power recycling cavity length were chosen so that when the carrier is resonant inside the arm cavities and power recycling cavity, the modulation sidebands are resonant in the power recycling cavity while being anti-resonant in the arm cavities. This ensures that the REFL and POP error signals are sensitive to PRCL and CARM (analogous to the coupled cavity readout scheme in the previous section).

The asymmetric port is held on a dark fringe. To obtain an error signal some of the sideband power needs to be made to exit at this port. The arm cavities when resonant with the carrier act as perfect reflectors for the sidebands. As such the sidebands only see the short michelson. Therefore the asymmetric port can be made brighter for the sidebands by introducing an asymmetry into the short Michelson arm lengths, while remaining dark for the carrier. This asymmetry in the short Michelson is referred to as ‘Schnupp’ asymmetry [73]. Fluctuations in DARM, which can be caused by a passing gravitational wave, result in some carrier light exiting at the asymmetric port, where it beats with the sidebands and gives a reading in the AS error signal.

In reality these error signals are a linear combination of the degrees of freedom and the sensing matrix needs to be derived. The inverse of this sensing matrix is used as the control matrix, which yields readouts of the four degrees of freedom which are then fed back to the actuators, to hold the detector at its operating point.

### 3.5 Advanced LIGO Readout

The Advanced LIGO detector differs from Initial LIGO, with the inclusion of a fifth degree of freedom that needs to be controlled, i.e. the signal recycling cavity. The asymmetric readout has also been converted from heterodyne readout to a type of homodyne readout, referred to as DC readout [74, 75].

In the DC readout scheme, a slight offset is injected into DARM, which slightly detunes the arm cavities from resonance, resulting in the asymmetric port being no longer dark to the carrier beam. This offset induced carrier light acts as the local oscillator for any gravitational wave induced carrier light to interfere with. This is a homodyne scheme because the local oscillator and signal light are at the same frequency. A more intuitive picture for DC readout, is to think of the power at the asymmetric port to DARM fluctuations, which is non-zero when offset from a dark fringe.

With the addition of the signal recycling cavity, the response of the detector can be varied. For broadband operation the signal recycling cavity is held on carrier resonance, whereas for narrowband operation it is slightly detuned. The power recycling cavity is still held resonant with the carrier. The operating point of the Advanced LIGO detector can be reached by holding the roundtrip phases of the five degrees of freedom to the following

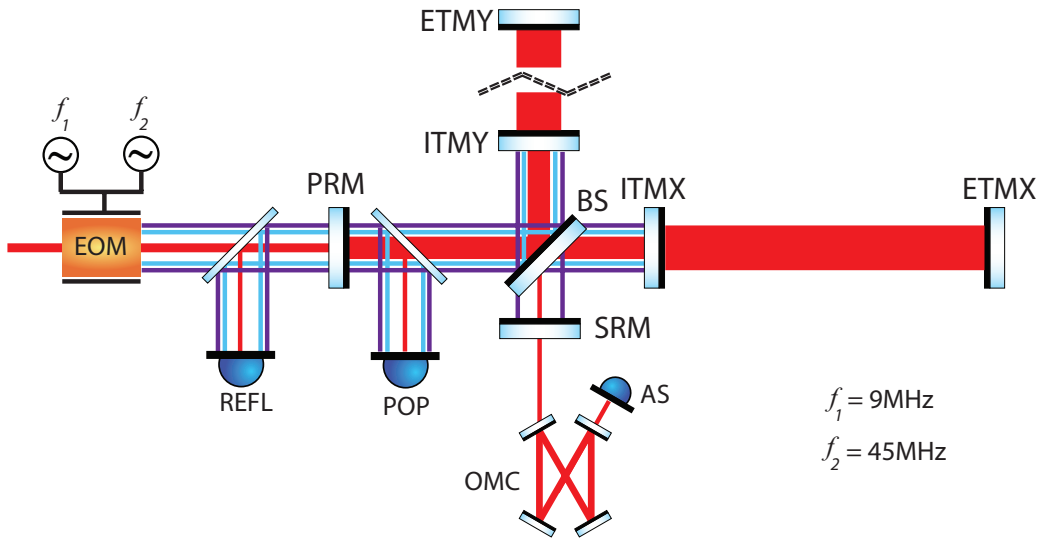


Figure 3.8: Basic schematic for the readout scheme for the Advanced LIGO interferometer.

values (modulo  $2\pi$ ):

$$\Phi_{DARM} = \Phi_{dc} \pmod{2\pi} \quad (3.34)$$

$$\Phi_{CARM} = 0 \pmod{2\pi} \quad (3.35)$$

$$\phi_{MICH} = 0 \pmod{2\pi} \quad (3.36)$$

$$\phi_{PRCL} = 0 \pmod{2\pi} \quad (3.37)$$

$$\phi_{SRCL-bb} = 0 \pmod{2\pi} \quad (3.38)$$

$$\phi_{SRCL-nb} = \phi_{det} \pmod{2\pi}$$

Where  $\phi_{SRCL-bb}$  refers to the DARM phase for broadband operation and  $\phi_{SRCL-nb}$  refers to the DARM phase for narrowband operation.  $\Phi_{dc}$  represents the detuning of the DARM degree of freedom in order to invoke DC readout and  $\phi_{det}$  is the detuning of the SRCL degree of freedom for narrowband operation. From here on, we will only consider the broadband operation of the signal recycling cavity. A simplified diagram depicting the layout for the proposed Advanced LIGO readout is shown in Figure 3.8. Again the reflected field and a pick from the power recycling cavity are demodulated to obtain error signals. Besides the signal recycling mirror, there are two other important additions to the readout scheme.

The first addition is the extra set of modulation sidebands. In theory the five error signals that would be obtained from one set of sidebands with the REFL and PO ports, and the DC error signal from the AS error port, should be sufficient to cover the five degrees of freedom. However in practice, such a readout scheme is more complicated. Hence the need for the second set of sidebands.

The second addition is that of the four mirror bow-tie cavity at the asymmetric port (after the signal recycling mirror). This cavity, referred to as the Output Mode Cleaner (OMC) [76], is used to filter off unwanted modes of light that exit out the interferometer

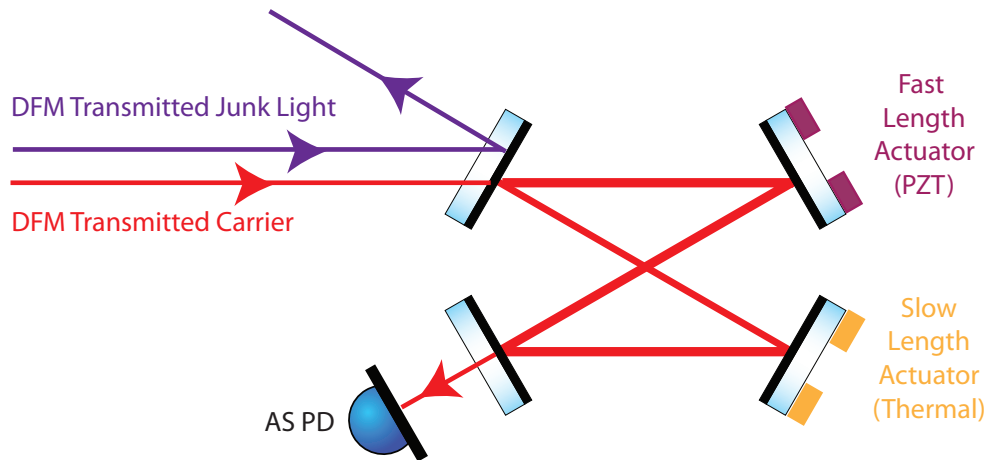


Figure 3.9: Layout of the OMC cavity. The carrier from the Dual Recycled Fabry-Perot Michelson (DFM) is transmitted through the OMC, while the junk light is reflected off.

towards the AS photo-detector.

The science beam is phase modulated at two frequencies,  $f_1 = 9$  MHz and  $f_2 = 45$  MHz. As in Initial LIGO, both set of sidebands are anti-resonant in the arm cavities when the carrier is resonant. The 9 MHz sidebands are made resonant inside the power recycling cavity again through careful choice of the power recycling cavity length and sideband frequency.

The 45 MHz sidebands are made to resonate inside the signal recycling cavity. This is achieved by introducing a Schnupp asymmetry into the MICH degree of freedom for this sideband ( $\phi_{mich-sb2} \neq 0$ ), so that the sideband is transmitted to the asymmetric port. The 45 MHz sidebands also need to be made resonant in the power recycling cavity<sup>1</sup>.

### Output Mode Cleaner

The optical fields that exit the interferometer and shine onto the AS photodetector are intended to exist only in the fundamental gaussian spatial mode. Any higher order spatial modes (Hermite-Gauss and Laguerre-Gauss) will corrupt the measurement via unwanted noise couplings. An input mode cleaner is used at the input of the interferometer to remove higher order modes produced by the laser, however imperfections in the interferometer optics also lead to production of higher order modes that make their way to the photodetector. The control sidebands also find their way to the asymmetric port. These unwanted modes of light are referred to as ‘junk light’.

The Output Mode Cleaner (OMC) is responsible for filtering off this junk light. Figure 3.9 shows the configuration of the OMC, which is a four mirror bow tie cavity. The OMC is made resonant with the carrier light that is transmitted by the dual recycled

<sup>1</sup>The signal recycling cavity forms a coupled cavity with the power recycling cavity (with the Fabry-Perot Michelson acting as the coupling mirror)

Fabry-Perot Michelson. The higher order spatial modes that make up the junk light receive a larger phase retardation from the guoy effect than the gaussian mode and are therefore reflected off the cavity (shown in Figure 3.9).

To sense and control the length of OMC, and lock it on resonance with the carrier light a technique called ‘dither locking’ is used. The length of the cavity is modulated by a small amount at 10kHz. The transmitted light intensity is demodulated at this frequency to sense the cavity resonance condition.

The length dither is supplied by a piezo-electric transducer (PZT) on the back of one of the mirrors. The OMC cavity readout is fed back to this PZT, however the range of this PZT is quite short ( $< 0.1 \mu m$ ), and can not track over a full cycle ( $0.5 \mu m$ ). A thermal actuator is fitted to the back of one of the other mirrors (resistive heater). This thermal actuator has a range of  $20 \mu m$ .

## 3.6 Summary

This chapter provided a background on the main interferometric sensing techniques used to readout the degrees of freedom, such as heterodyne interferometry and the Pound-Drever-Hall technique. These techniques were also used in the experimental work presented in Chapters 6 and 7.

The final sections in this chapter looked at the readout scheme for Initial LIGO and the planned readout scheme for Advanced LIGO. The homodyne DC gravitational wave readout was discussed, and the Output Mode Cleaner (OMC) introduced.

The need for an OMC has led to the design of the Tip Tilt mirrors, which are used to steer the interferometer output beam into the OMC. The design of these Tip Tilt mirrors is presented in the next chapter, along with results from the characterisation of a proto-type Tip Tilt.

# Chapter 4

## Tip Tilt Mirrors

As mentioned in the previous chapter, an Output Mode Cleaner (OMC) cavity will be used at the readout port of the interferometer, as part of the new DC readout scheme for Advanced LIGO. The added complexity that comes with the inclusion of this OMC is that misalignment fluctuations of the interferometer output beam into the OMC will couple into the gravitational readout. As such the design of the optics used to steer and mode-match the beam into the OMC are critical to the performance of the DC readout. We refer to these optics as Tip Tilt mirrors [77].

### 4.1 Cavity Misalignment Coupling

Angular and translational misalignments of the beam inside the OMC [76] result in intensity fluctuations of the transmitted beam, and therefore into the gravitational wave readout.

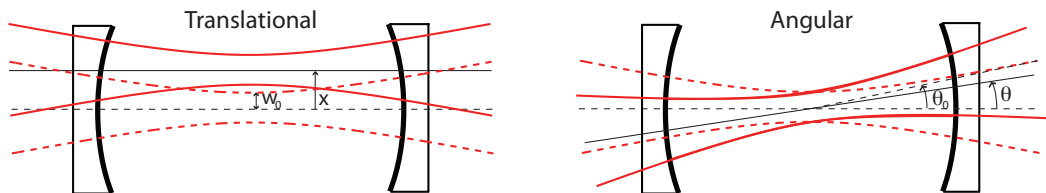


Figure 4.1: Translational ( $x$ ) and Angular Misalignments ( $\theta$ ) inside a Fabry-Perot Cavity.  $w_0$  is the waist radius and  $\theta_0$  is the divergence angle of the cavities fundamental mode.

To first order the power of the transmitted beam (derived from [78]) is given by:

$$P_t = P_{t0} \left( 1 - 2 \left( \frac{x}{w_0} \right)^2 - 2 \left( \frac{\theta}{\theta_0} \right)^2 \right) \quad (4.1)$$

where  $P_{t0}$  is the transmitted power for optimal alignment, when the interferometer beam is perfectly aligned to the cavity,  $x$  and  $\theta$  are the translational and angular misalignments respectively between the beam axis and the cavity axis, and  $w_0$  and  $\theta_0$  are the waist radius

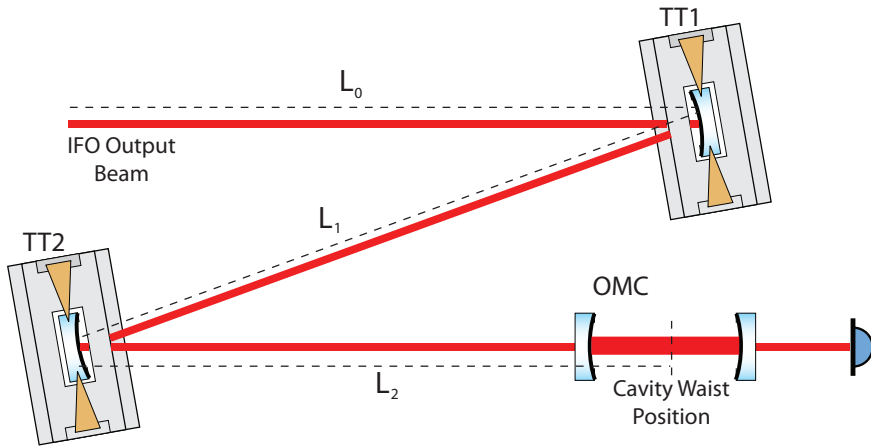


Figure 4.2: Steering of the interferometer output beam into the OMC by the Tip Tilts.

and divergence angle respectively of the fundamental Gaussian beam of the cavity (see Figure 4.1<sup>1</sup>).

A minimum of two mirrors are therefore required to steer the interferometer output beam into the OMC, as shown in Figure 4.2. These mirrors are also curved appropriately to mode-match the interferometer output beam into the OMC cavity. The translational and angular displacement of the beam with respect to the OMC can be controlled, through control of the angles of the two mirrors. This is how the mirrors get their name ‘Tip Tilt’ mirrors.

Misalignment fluctuations into the OMC, arise through two mechanisms:

- via ground motion coupling to the angular motion of the Tip Tilt mirrors
- through relative angular jitter of the interferometer beam with respect to the OMC

To counter the misalignments via the first mechanism the Tip Tilts are suspended as pendulums. Above the pendulum resonance frequency of the Tip Tilt suspension, the mirrors act as free masses and are therefore isolated from the ground motion (see Section 2.5.1). In addition to the longitudinal mode, the other two linear degrees (vertical and transverse) and the three rotational degrees (pitch, yaw and roll) of freedom also need to be seismically isolated, for reasons discussed in Section 4.2.

In relation to both the first and second mechanisms, the angular and translational misalignments of the cavity are sensed directly, and suppressed by feeding back to the angles of the Tip Tilt mirrors in a control loop. The sensing and actuation of the Tip Tilts is discussed further in Section 4.3.

## 4.2 Mechanical Design

The Tip Tilt mirror suspension has been designed to provide isolation in all six degrees of freedom. The eigenfrequencies of the six degrees of freedom are all designed to be less than

---

<sup>1</sup>The OMC is illustrated as a linear cavity for simplicity

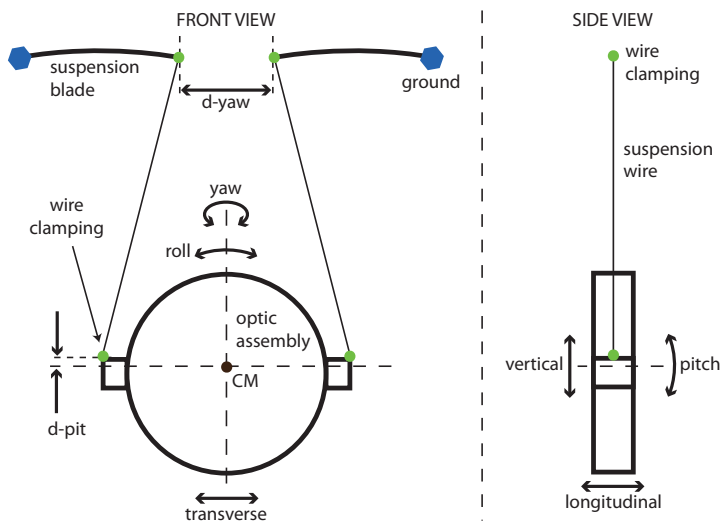


Figure 4.3: The schematic overview of the suspended optic of the Tip Tilt design, showing the six degrees of freedom - longitudinal, transverse, vertical, yaw, pitch and roll.

10 Hz which is at the lower end of the Advanced LIGO sensitivity band (see Figure 2.10). The quality factors of these eigenmodes are required to be less than 100.

The Tip Tilt mirror suspension is designed around a suspended aluminium ring, which holds a  $\varnothing 50.8\text{ mm} \times 9.52\text{ mm}$  optic. Seismic isolation of the mirror and mirror holder is provided by means of a single stage pendulum and cantilever blade springs. This is schematically shown in Figure 4.3. The blue hexagonal ‘ground’ points indicate where the base of the blades are attached to the mounting structure. The suspension wires are attached at the tip of the suspension blades via a clamping mechanism as indicated by the green circles. At the other end of the suspension wire, the wire is clamped to the aluminium ring.

The blade springs are mounted to the Tip Tilt structure, which is also responsible for holding the mirror actuators. The structure is manufactured from standard vacuum compatible materials (aluminium and stainless steel) and is  $\sim 250\text{ mm}$  in height. The structure was designed to be stiff so that its mechanical modes would have eigenfrequencies greater than 150 Hz [79]. This design requirement was to ensure that the structure had minimal impact on the platform it was mounted to.

The whole unit was designed using Solidworks, an engineering rendering of the whole Tip Tilt stage can be seen in Figure 4.4. From Solidworks theoretical values of the moments of inertia and various eigen-modes of the Tip Tilt can be obtained, which are important properties for the seismic isolation of mirror.

The seismic isolation is provided by means of the single stage pendulum and the cantilever blade springs. Ideally it would only be the pitch and yaw degrees of freedom that would need to be isolated, as in theory these are the only degrees of freedom that affect the translational and angular misalignment in the cavity. However there are mechanisms that can couple the other degrees of freedom into the misalignment. One such mechanism

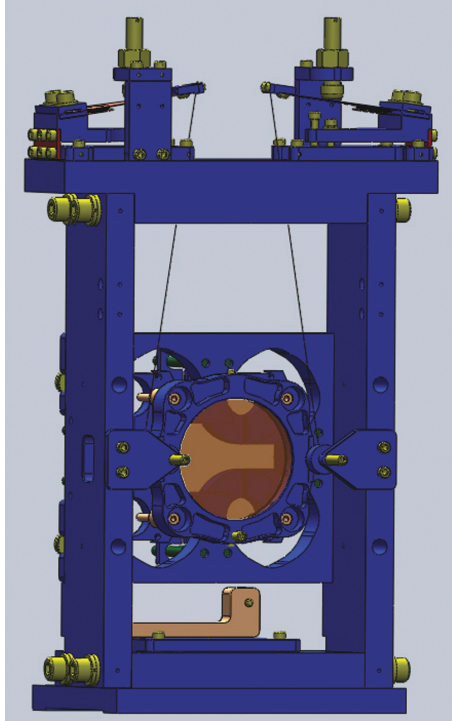


Figure 4.4: An engineering rendering of the Tip Tilt suspension stage.

is the curvature of the mirror, which couples in the longitudinal, transverse and vertical motion. Longitudinal motion also diverts away from optimum mode matching into the cavity.

The longitudinal, transverse, pitch and yaw degrees of freedom, are isolated via the single stage pendulum, whereas the vertical and roll modes are isolated via the blade springs.

#### 4.2.1 Pendulum Isolation

Horizontal isolation is achieved by suspending the mirror by a simple pendulum with two wires, one on either side of the aluminium ring. The wire ends are clamped between two metal plates.

The pendulum has a length of 140 mm. The suspension wire is 127  $\mu\text{m}$  in diameter, thin enough to reduce flexing of the wire near the wire clamps, and thick enough to prevent the wire from breaking during handling and assembly.

The resonance frequencies for the linear modes are determined by the resistance to the displacement in that mode, and the mass. For angular modes, they are determined by the resistance to angular deviations and the moment of inertia. The resonance frequency of each degree of freedom is important, as above this frequency the mirror acts as a free mass and is isolated from the motion of the suspension point.

For the pendulum isolated modes - longitudinal, transverse, pitch and yaw; the resistance is mostly due to gravity [80]. The resonance frequency of the longitudinal mode is

simply given by:

$$f_{long} \simeq \frac{1}{2\pi} \sqrt{\frac{g}{l}} \quad (4.2)$$

where  $l$  is the vertical distance from the centre of mass to the suspension point ( $l = 140$  mm). The transverse mode receives its isolation via the same mechanism, however it also receives extra resistance from strains in the wires, and therefore has a slightly higher resonance frequency than the longitudinal mode

$$f_{tran} \gtrsim f_{long} \quad (4.3)$$

The mirror suspension point is above the centre of mass, meaning that the main resistance to pitch is gravity. The pitch resonance is dependent on the displacement of the suspension point above the centre of mass, denoted  $d_{pit}$ , and is approximately equal to:

$$f_{pit} \simeq \frac{1}{2\pi} \sqrt{\frac{Mgd_{pit}}{I_{pit}}} \quad (4.4)$$

where  $M$  is the mass of the mirror and  $I_{pit}$  is the moment of inertia of the mirror about the pitch axis of rotation. When the mirror twists or rotates in yaw, the mirror rises in height, and therefore gravity again provides the main resistance. The yaw resonance frequency is given by:

$$f_{yaw} \simeq \frac{1}{2\pi} \sqrt{\frac{Mgd_{eff}d_{yaw}}{4I_{yaw}l}} \quad (4.5)$$

where  $I_{yaw}$  is the moment of inertia of the mirror about the yaw axis of rotation,  $d_{eff}$  is the effective diameter of the optic and  $d_{yaw}$  is the distance between the upper suspension points (see Figure 4.3).

Note that these equations only provide an approximation of the eigenmode frequencies. In reality the eigenmodes of the pendulum are more complex, mostly due to the elastic properties of the wire [51]. In particular, their exists a coupling between the longitudinal and pitch mode, due to the stiffness of the wire near the aluminium ring clamping point.

The modelled eigenmode frequencies for the pendulum isolated modes are:

Mode	Modelled Frequency
Longitudinal	1.31 Hz
Transverse	1.34 Hz
Pitch	1.65 Hz
Yaw	1.60 Hz

Table 4.1: The modelled frequencies of the pendulum isolated modes.

### 4.2.2 Blade Springs

Vertical isolation for the suspended mirror is provided by two triangular shaped beryllium copper cantilever blade springs. Beryllium copper has been chosen as the blade spring

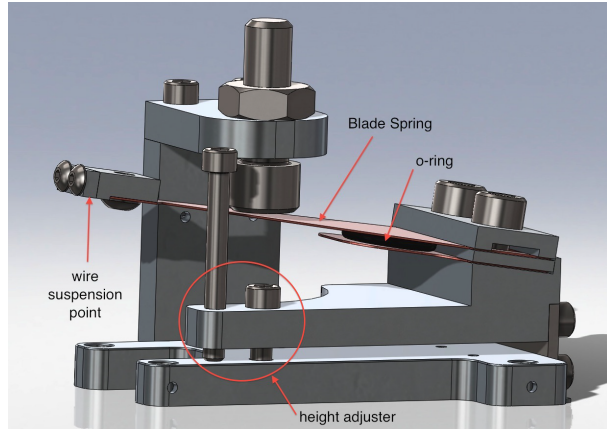


Figure 4.5: The cantilever blade springs and their mounting unit.

material, due to its elastic properties and high tensile strength. These blades are of similar design to those used in the VIRGO and Advanced LIGO test mass suspensions [81, 82]. Each blade is mounted in an aluminium structure with a lockable height adjuster, which allows for the height of the suspended optic to be adjusted relative to the backplane of the Tip Tilt structure. To reduce the bending of the wire at the suspension point, the blades are launched at an angle such that the wires leave the clamps at  $90^\circ$  when loaded with the mirror. A solidworks illustration of the blade spring unit is shown in Figure 4.5.

The vertical and roll modes receive most of their isolation via the blade springs. The blade vertical resonance frequency is given by

$$f_{vert} \approx \frac{1}{2\pi} \sqrt{\frac{Ew_{blade}t_{blade}^3}{4Ml_{blade}^3\alpha}} \quad (4.6)$$

where  $E$  is the Young's Modulus,  $w_{blade}$  is the width of the blade at the base,  $t_{blade}$  is the blade thickness,  $l_{blade}$  is the length of the blade, and  $\alpha$  is defined as the shape factor, which is 1.5 for this blade [81]. The vertical resonance was set, by choosing these blade parameters carefully (thickness, width and length).

A practical balance was achieved between the length of the blades (to simplify manufacturing and keep the unit small) and the requirement to keep the resonance under 10 Hz. The modelled frequencies of the two modes isolated by the blade spring are:

Mode	Modelled Frequency
Vertical	6.0 Hz
Roll	8.7 Hz

Table 4.2: The modelled eigenmode frequencies of the blade spring isolated modes.

## 4.3 Tip Tilt Mirror Control

Active suppression of the misalignments into the OMC, requires that the Tip Tilt mirrors be controllable in pitch and yaw. This is achieved through electromagnetic actuation, and a combination of sensing techniques - local sensing and dither locking.

The electromagnetic actuation consists of four voice-coils surrounding magnets which are mounted to the mirror holder. The local sensing scheme, uses four flags mounted on the back of the magnets, and therefore the mirror holder. Each flag is positioned between a ‘shadow sensor’ which consists of an LED shining light onto a photodiode. Movement of the mirror and therefore the flag, results in a change in optical power falling on the diode, providing a readout. See Appendix B for a description on dither locking.

Each shadow sensor and voice-coil are integrated into a single unit, referred to as the Optical Sensor and Electro-Magnetic actuator (OSEM). The four OSEMs are mounted into the backplane of the Tip Tilt structure. The particular OSEMs used in the Tip Tilts were designed and built at the University of Birmingham and are referred to as BOSEMs [83].

The actuation controllers and readouts of the degrees of freedom are all digitally contained on a system commonly referred to as the Control and Data System (CDS).

### 4.3.1 Electromagnetic Actuation

A simplified schematic of the actuation scheme of the Tip Tilt mirror’s longitudinal, pitch and yaw degrees of freedom is shown in Figure 4.6.

Actuation of the longitudinal, pitch and yaw degrees of freedom is provided by four voice coils, which are part of the BOSEMs. Each voice-coil is paired with a magnet, which is mounted to the suspended aluminium ring. The four coil magnets are located in the upper left (UL), upper right (UR), lower left (LL) and lower right (LR) corners of the mirror.

The magnets used in the Tip Tilts are Nickel plated SmCo ( $\text{Sm}_2\text{Co}_{17}/\text{SmCo}$  2:17), and are  $\varnothing 2 \text{ mm} \times 3 \text{ mm}$  long. The magnets are arranged with alternating polarities to reduce the magnetic moment of the mirror assembly.

A force is exerted on each magnet by sending current through the coil. The force is dependent on the magnet strength and polarity, the magnet to coil separation and the current magnitude and sign. The magnitude and sign of the current through the coil (and therefore the force) is controlled by a digital coil controller. The digital signal from the controller passes through a digital to analog converter (DAC), which converts the signal from a digital number in counts (cts) to a voltage. This voltage passes through a series resistor where it is converted to current for the coil.

The longitudinal position of the mirror is controlled by the POS controller which sends signals of the same magnitude to the controllers of the upper left coil (ULC), upper right coil (URC), lower left coil (LLC) and lower right coil (LRC). The pitch of the mirror is controlled by the PIT controller which sends signals of the opposing magnitude to the upper and lower coil controllers so as to impose a torque about the horizontal axis of the

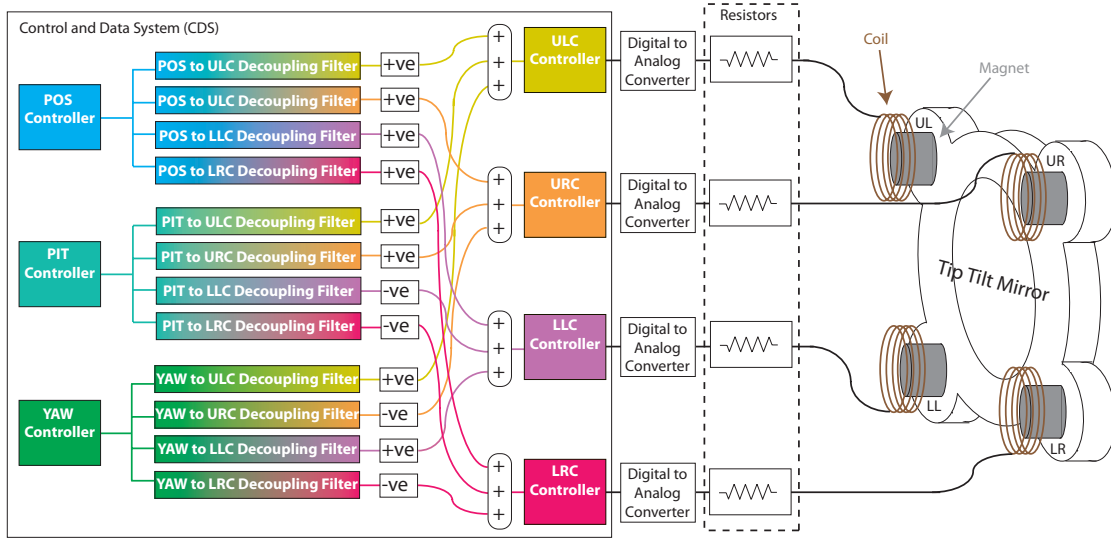


Figure 4.6: A schematic overview of the electromagnetic actuation of the Tip Tilt mirror showing the coil-magnet configuration.

mirror. The mirror is controlled in yaw by the YAW controller which sends signals of opposing magnitude to the left and right coil controllers so as to impose a torque on the mirror about its vertical axis.

The decoupling filters (shown in Figure 4.6) between the degree of freedom controllers and the coil controllers provide a way of reducing frequency dependent cross-coupling between the degrees of freedom. One example of such a frequency dependent cross coupling is the one that exists between the longitudinal and pitch degrees of freedom [84]. Due to the mirror suspension point being above the centre of mass, to actuate on the mirror's position the force on the upper part of the mirror needs to be greater than the force on the lower part, so as to ensure that the net pitch torque is zero. However above the pendulum resonance, the mirror acts as a free mass and the upper and lower forces should be equal.

### 4.3.2 Local Sensing

Local sensing of the mirror's longitudinal, pitch and yaw degrees of freedom relative to the Tip Tilt structure are obtained by mounting four flags to the mirror holder (over the magnets). Each flag is positioned such that it blocks half of the light falling onto a photo-diode (PD) from an opposing light emitting diode (LED). This combination of the PD and the LED is referred to as a shadow sensor. Movement of the flag and hence the aluminium ring, registers as a change in optical power falling on the PD. The photo-current from the PD is converted to voltage by a trans-impedance amplifier, which in turn is converted to a digital signal by the analog to digital converter (ADC). This digital signal is the BOSEM shadow sensor readout. A simplified diagram of the local sensing scheme is shown in Figure 4.7.

A readout of each degree of freedom is obtained through combinations of each shadow sensor readout, in the same way that the three actuations were achieved. The readout

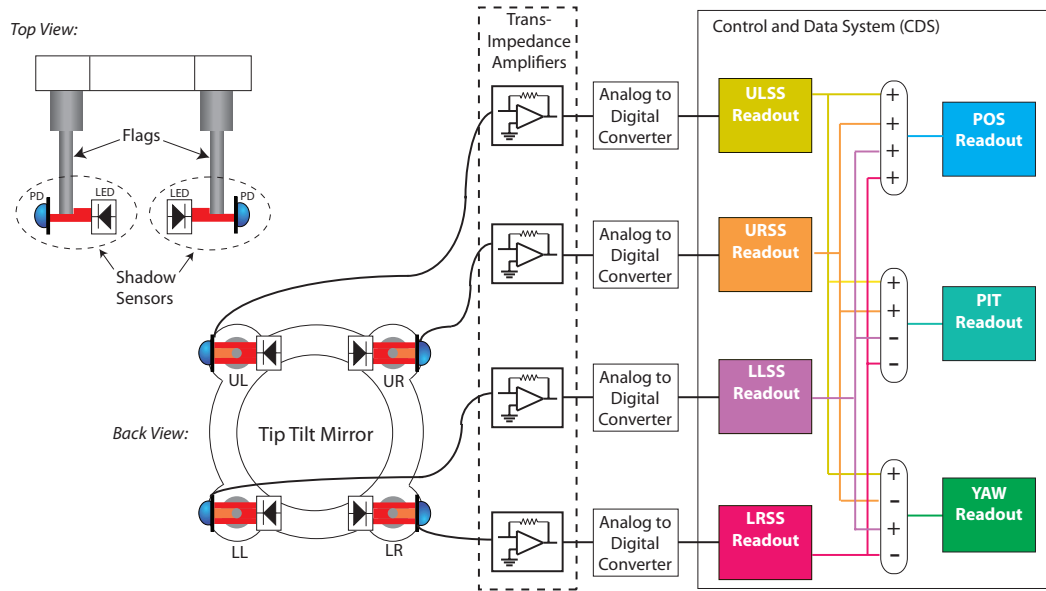


Figure 4.7: The local sensing scheme for the Tip Tilt mirrors, showing the flags attached to the back of the mirrors and the shadow sensors which consist of a Light Emitting Diode (LED) shining light onto a Photo-diode (PD).

of the mirror's longitudinal position (POS readout) is obtained by summing the upper left shadow sensor (ULSS), upper right shadow sensor (URSS), lower left shadow sensor (LLSS) and lower right shadow sensor (LRSS) readouts. The readout of the pitch of the mirror (PIT readout) is obtained by summing the upper and subtracting the lower SS readouts. The readout of the yaw of the mirror is obtained by summing the left and subtracting the right SS readouts.

Local sensing will only be used for initial coarse steering into the OMC and for damping of the mechanical resonances. The damping is carried out by feeding the local sensor readouts back to the actuators via ac-coupled filters. The frequency dependent controller also has to have a roll off above the resonance frequency to ensure that the mirror remains isolated from the Tip Tilt structure and still acts as a free mass. In addition to this active local damping, the mirror will be passively damped via the eddy-current damping, which arises due to the magnets being surrounded by conductors i.e. the copper coils.

## 4.4 Tip Tilt Characterisation

The performance of a prototype Tip Tilt mirror suspension, shown in Figure 4.8, was measured and compared to numerical models. First the shadow sensors were calibrated so that the POS, PIT and YAW readouts could be derived. The transfer functions of the longitudinal, pitch and yaw modes were then measured and from these transfer functions the modal resonances and quality factors were obtained and compared to the design requirements. A shadow sensor scheme was used to measure the resonance frequencies of the vertical and roll modes. The eigenmodes of the Tip Tilt structure were also measured.

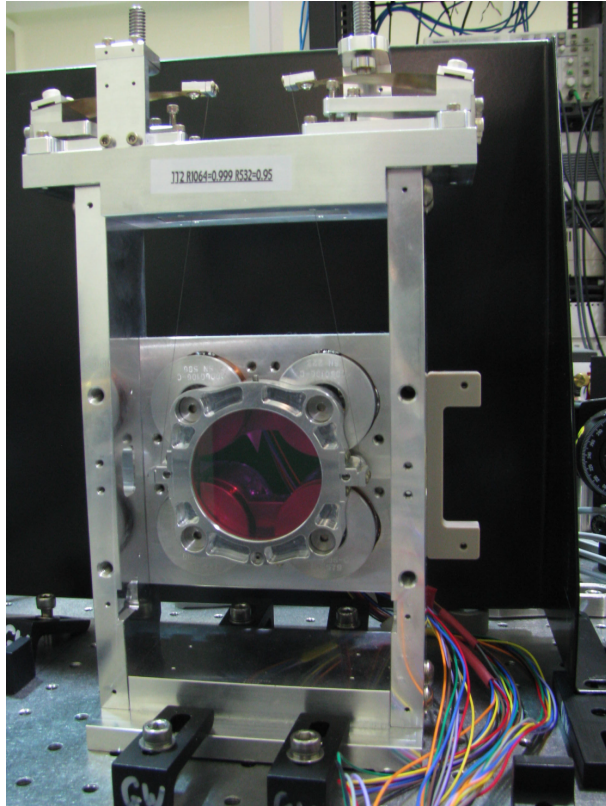


Figure 4.8: The prototype Tip Tilt mirror.

#### 4.4.1 Shadow Sensor Calibrations

Prior to the transfer function measurements, each OSEM shadow sensor had to be calibrated. This was achieved by mounting a flag onto a translational stage that allowed the position of the flag between the LED and the PD, to be tuned. The translational stage was fitted with a micro-metre gauge for precise readout of the position. The position of the flag was tuned over a range of  $\sim 1$  mm, and the micro-metre and shadow sensor readouts recorded. More points were recorded near where the flag was blocking half of the light, to emphasise the linearity at this position. The results of these measurements are plotted in Figure 4.9.

A line was fitted to the linear region, and the sensitivity of each OSEM shadow sensor obtained at this point. Each OSEM shadow sensor was normalised by multiplying by a sensor gain in the CDS. The sensitivities and sensor gain are listed in Table 4.3. The normalised sensitivity for each OSEM was  $16.36 \text{ ct}/\mu\text{m}$ .

The POS readout is the sum of the four OSEM shadow sensor readouts, and therefore the calibration for the position of the mirror is found by summing the four OSEM normalised sensitivities. This calibration was found to be:

$$S_{sspos} = 65.4 \text{ ct}/\mu\text{m} \quad (4.7)$$

The calibration for the angle (PIT and YAW) of the mirror is calculated from the

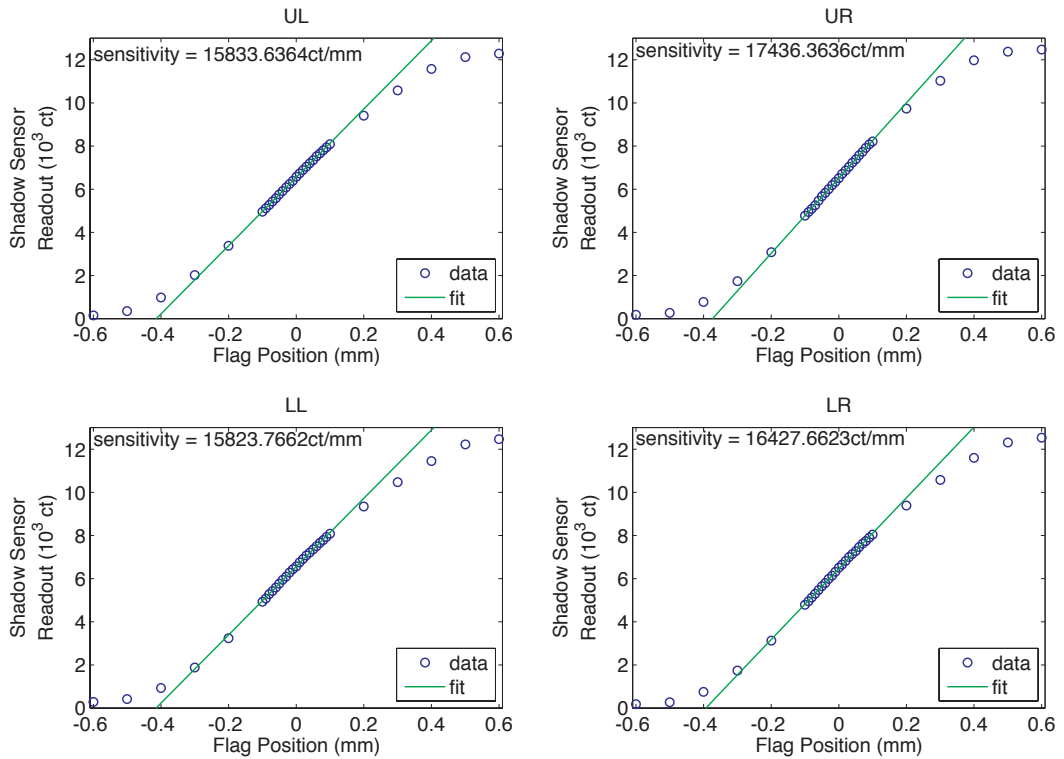


Figure 4.9: Calibration of the four OSEM shadow sensors over a range UL = Upper Left, UR = Upper Right, LL = Lower Left, LR = Lower Right.

OSEM Shadow Sensor	Sensitivity (ct/ $\mu$ m)	Sensor Gain	Normalised Sensitivity (ct/ $\mu$ m)
UL	15.83	1.0329	16.36
UR	17.44	0.9380	16.36
LL	15.82	1.0336	16.36
LR	16.42	0.9956	16.36

Table 4.3: Measured sensitivity and calculated gains for the normalisation of the shadow sensors.

OSEM calibrations and the distance between the flags (48 mm). This was found to be:

$$S_{ssangle} = 1.57 \text{ ct}/\mu\text{rad} \quad (4.8)$$

#### 4.4.2 Transfer Functions Measurements

The transfer functions for the longitudinal, pitch and yaw were measured between 0.5 and 20 Hz. This was achieved by exciting each degrees of freedom using the POS, PIT and YAW controllers and recording the corresponding readouts derived from the shadow sensor signals.

The longitudinal transfer function was calibrated using Equation 4.7 and is plotted in

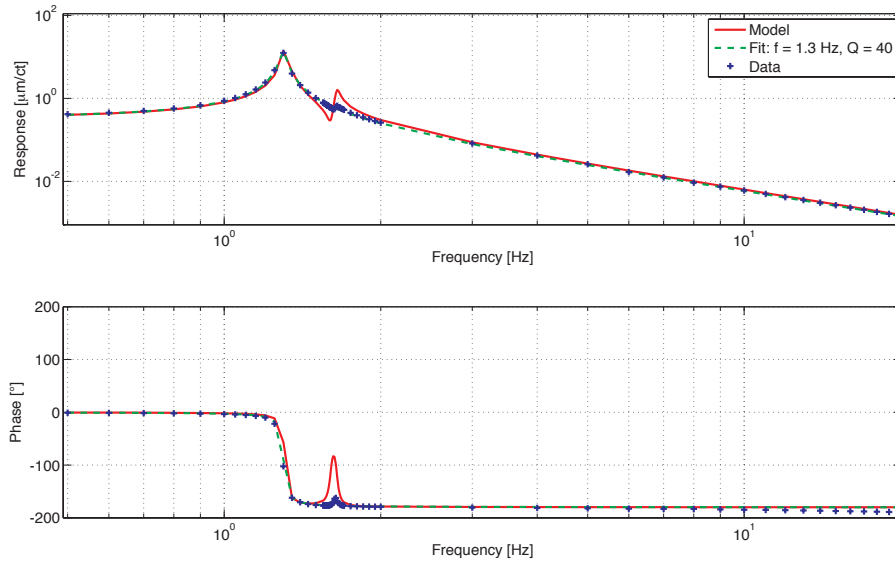


Figure 4.10: Transfer function from force applied by the coil actuators to longitudinal position of mirror.

Figure 4.10). As expected the response is that of a pendulum (see Figure 2.3), with a  $f^{-2}$  response above resonance.

The pitch and yaw transfer functions were calibrated using Equation 4.8 and are plotted in Figure 4.11 and 4.12 respectively. The responses of these degrees of freedom also have a  $f^{-2}$  response above resonance, which is expected as they are also seismically isolated via the pendulum.

Each response was fitted and values for the resonance frequency and mechanical quality factor were obtained. These values are listed in Table 4.4. The Tip Tilt responses were also modeled using Mark Barton's suspension modeling toolkit [85], and are plotted with the responses.

Mode	Measured Resonance	Modelled Resonance	Quality Factor
Longitudinal	1.30 Hz	1.31 Hz	40
Pitch	1.63 Hz	1.65 Hz	40
Yaw	1.59 Hz	1.60 Hz	23

Table 4.4: The measured and modelled resonance frequencies and the mechanical quality factors of the pendulum isolated modes.

The measured resonances differ from the modelled values by less than 2%, and are all much less than 10 Hz, meeting the requirement. The quality factors are less than 100 and therefore also meet the Advanced LIGO requirement.

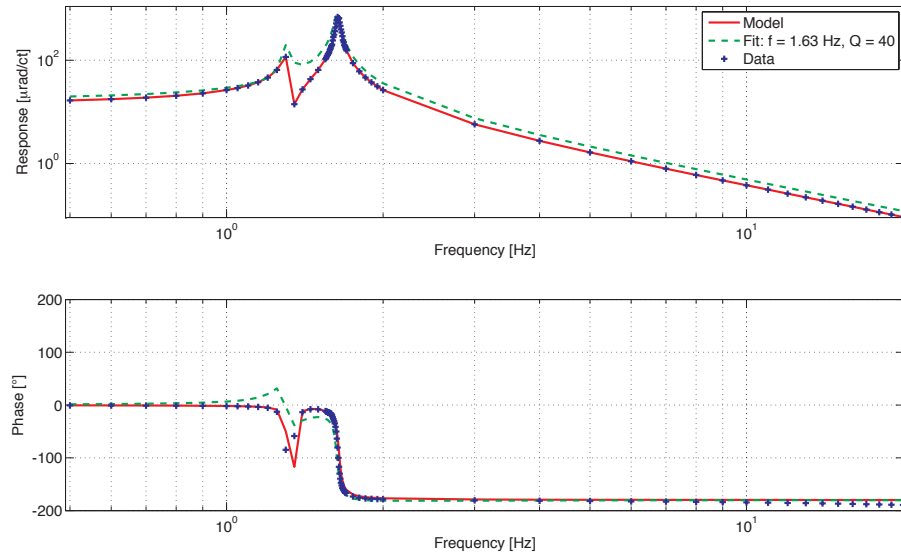


Figure 4.11: Transfer function from torque applied in pitch by the coil actuators to mirror pitch.

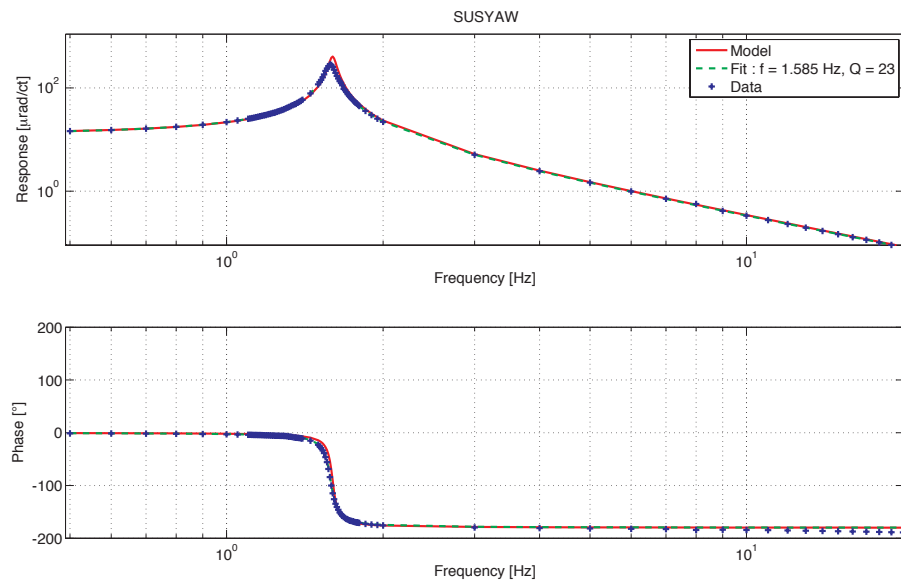


Figure 4.12: Transfer function from torque applied in yaw by the coil actuators to mirror yaw.

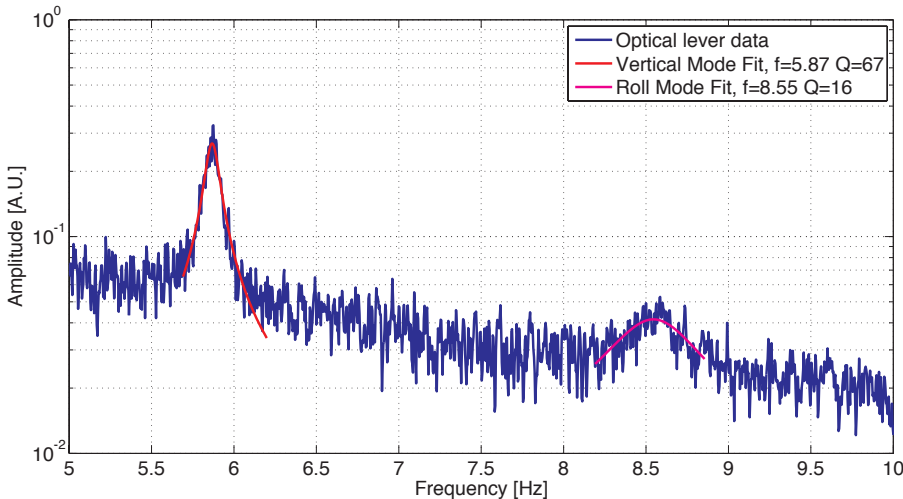


Figure 4.13: Spectra of the vertical bounce mode data.

#### 4.4.3 Vertical Mode Measurement

The vertical bounce mode was measured by creating a shadow sensor at the tip of one of the suspension blades. A laser was shone onto the wire clamp of one of the blades, which blocked approximately half of the light, and let the half past to a photo-detector.

The mirror was excited by the air turbulence and seismic noise naturally present in the laboratory. Intensity fluctuations due the oscillations in the blade were recorded. Figure 4.13 shows the spectra of this read out. The measured resonance frequency and mechanical quality factor were fitted and are listed in Table 4.5. The roll mode was also excited sufficiently to register on the shadow sensor readout. The fitted resonance frequency and quality factor of the roll mode are also included in Table 4.5.

Mode	Measured Resonance	Modelled Resonance	Quality Factor
Vertical	5.87 Hz	6.0 Hz	67
Roll	8.55 Hz	8.7 Hz	16

Table 4.5: The measured and modelled frequencies and the quality factors of the blade spring isolated modes.

#### 4.4.4 Tip Tilt Structure Eigenmodes

The Tip Tilt structure was designed to be stiff so that its lowest mechanical mode would be above 150 Hz [79]. To measure these mechanical modes, the Tip Tilt structure was mounted on a vertically actuated vibration table (TIRA TV 55240/LS-340), and accelerometers mounted to the structure and vibration table were used to record the relative vibrations.

The eigenmode of the structure that corresponded to longitudinal mirror motion was

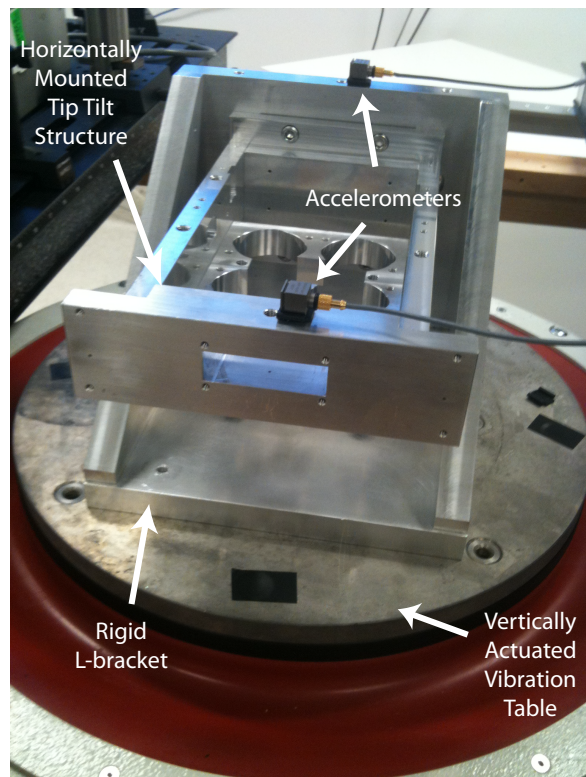


Figure 4.14: Setup for measuring the eigenfrequencies of the mechanical modes of the Tip Tilt structure.

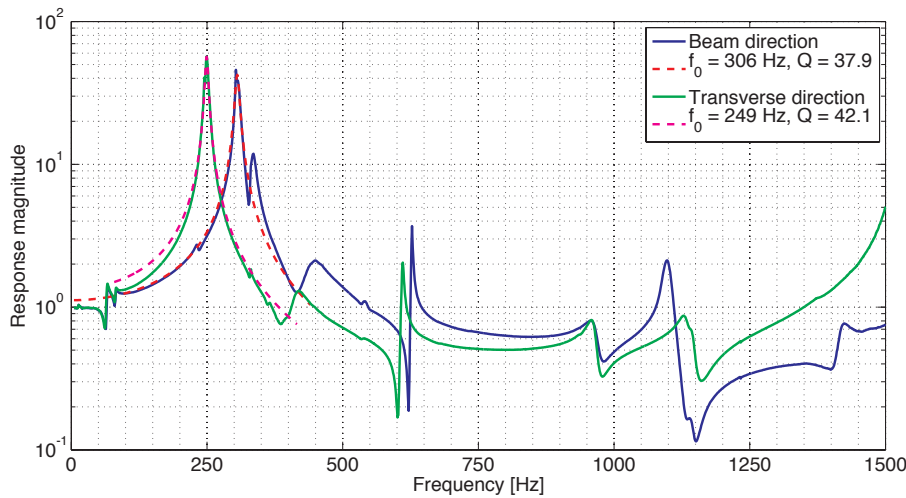


Figure 4.15: Measured eigenmodes of the Tip Tilt structure.

measured first. This mode was measured by mounting the Tip Tilt structure horizontally to the vibration table via a rigid L-bracket, as shown in Figure 4.14. Three accelerometers were used to record the vibrations, one was mounted on the base of the platform (Accelerometer 1), one on top of the L-bracket (Accelerometer 2) and the other on top of the Tip Tilt structure (Accelerometer 3). The measurement of the longitudinal eigenmode was obtained by taking the ratios between the three accelerometer measurements:

$$\text{Measurement} = \frac{\text{Accelerometer 3/Accelerometer 1}}{\text{Accelerometer 2/Accelerometer 1}} \quad (4.9)$$

The structure was then rotated by 90°, and the procedure repeated to obtain a measurement of eigenmode corresponding to the transverse direction. The results for both measurements are shown in Figure 4.15. The largest resonances were fitted and were found to be at ∼306 Hz in the longitudinal direction and ∼249 Hz in the transverse direction, with respective quality factors of 37.9 and 42.1.

## 4.5 Summary

The Tip Tilt mirrors will be installed in Advanced LIGO as part of the DC readout. These suspended mirrors will be responsible for steering the interferometer beam into the OMC. The Tip Tilt mirrors are controllable in position, pitch and yaw, so that active beam jitter noise may be suppressed.

Through careful mechanical design, the eigenmode frequencies of the Tip Tilt mirrors linear and rotational degrees of freedom, are less than 10 Hz to ensure that they don't affect the Advanced LIGO performance across the sensitivity band (see Figure 2.10). The measurements of the proto-type presented in this chapter have shown that the Tip Tilt mirrors meet the design specifications. The eigenmodes of the Tip Tilt structure were also measured and found to meet design specifications.

Two of these Tip Tilt mirrors were used as mirrors for the Fabry-Perot cavity, in the Arm Length Stabilisation experiment presented in Chapter 6.



# Chapter 5

# Lock Acquisition and Arm Length Stabilisation

Lock acquisition is the process of taking an interferometer from an uncontrolled state where the mirrors swing freely and the interferometer's cavities flash through resonances to the locked state where the light is resonant in the interferometer and the various lengths are controlled.

In this chapter the problem of lock acquisition for Gravitational Wave Detectors and why it is difficult will be discussed. A summary of how lock acquisition was achieved in a first generation gravitational wave detector (Initial LIGO) will be given, followed by a summary of the proposed lock acquisition solution for a second generation gravitational wave detector (Advanced LIGO). It is here that Arm Length Stabilisation will be introduced, which is the motivation behind the experimental work presented in Chapters 6 and 7.

## 5.1 The Lock Acquisition Problem

The main difficulties with lock acquisition are:

- The mirrors are moving too fast through the linear range of the error signal, for the force limited actuators to catch them. (Threshold velocity)
- The sensing matrix for the degree of freedom readout changes, as the fields in the interferometer change. (Dynamic Sensing Matrix)

### 5.1.1 Threshold Velocity

One of the main difficulties in lock acquisition is the idea of threshold velocity. Consider the control of a simple cavity with suspended mirrors, where a reflection PDH error signal is derived (see Section 3.2) and fed back to the mirror actuators to hold it on resonance. Generally, obtaining lock is as simple as closing the feedback loop. Off resonance the error signal has zero slope. When the cavity swings onto resonance, the linear zero crossing

region of the error signal is reached and the actuators provide a force which acts to catch the mirrors and hold the cavity on resonance.

However if the mirrors are swinging too fast, and the actuators can't supply a sufficient force to stop the mirrors within the linear range of the error signal then the cavity will fail to acquire lock. This scenario has led to the definition of the threshold velocity. The threshold velocity is the maximum velocity the mirrors can be swinging at for which the actuators can still catch them and hold the cavity on resonance.

To calculate the threshold velocity, it is assumed that the velocity of the mirror is constant over the linear range of the error signal. The range over which the actuators have to slow the mirror down to a stop is equal to half the cavity linewidth (from Equation 2.21), which is equal to the optical wavelength over four times the finesse of the cavity:

$$\Delta x = \frac{\lambda}{4\mathcal{F}} \quad (5.1)$$

The actuator force will be constant, as it saturates in its attempt to stop the mirror. From the equations of motion [86], the threshold velocity can be derived:

$$v_{th} = \sqrt{\frac{F_{max}\lambda}{2m\mathcal{F}}} \quad (5.2)$$

where  $F_{max}$  is the maximum force of the actuators and  $m$  is the mass of the mirror.

To demonstrate the idea of threshold velocity, the lock acquisition of a simple Fabry-Perot cavity was simulated using Simulink [87]. We set the Fabry-Perot cavity such that one of the mirrors was unmoveable, while the other was moving with velocity,  $v_{mirror}$ . The cavity had similar parameters as a LIGO arm cavity, i.e. the mass of the moveable mirror was 40kg and the finesse of the cavity was 400. The threshold velocity  $v_{th}$  was calculated from the chosen parameters and the simulation was run with  $v_{mirror} < v_{th}$  and then with  $v_{mirror} > v_{th}$ . In the simulation the feedback loop was engaged only when the cavity swung onto resonance through.

Figure 5.1 shows the results of this simulation for the two cases. The top plots show the displacement of the mirror over time, whereas the bottom plots show the force of the actuator and the error signal sent to the actuator. In Figure 5.1 (a) it can be seen that the locking system catches the mirror and holds the mirror on resonance, whereas in (b) the mirror is moving too fast for the system to catch it.

### 5.1.2 Dynamic Sensing Matrix

Due to the cross-coupling between the optical fields inside each cavity, the sensing matrix employed when the gravitational wave detector is locked, is invalid for the other states of the instrument.

There are two solutions to this problem. The first solution is to calculate the sensing matrix as it varies for different conditions of the interferometer, and diagonalise this dynamic sensing matrix to reconstruct the degree of freedom readouts throughout the lock acquisition process. This type of lock acquisition solution was employed in Initial LIGO and will be described briefly in the next section.

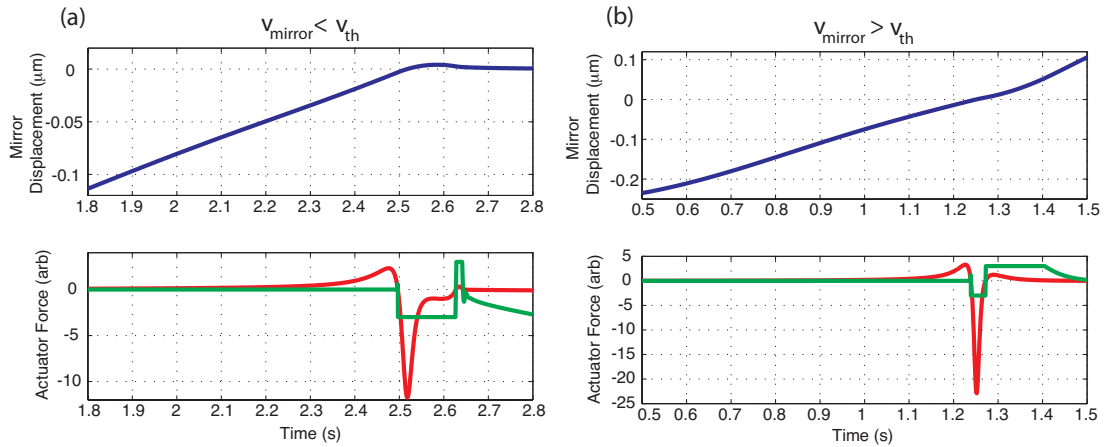


Figure 5.1: Shows the lock acquisition of a simple cavity when (a) the velocity of the mirror is less than the threshold velocity (b) the mirror velocity is greater than the threshold velocity. The top plots show the mirror displacement over time, whereas the bottom plots show the force applied by the actuator (green) and the error signal sent to the actuator (red).

The other solution is to use an alternative sensing scheme where the readouts for the degrees of freedom are already decoupled from each other and therefore there is no need to calculate the sensing matrix during the lock acquisition process. This type of lock acquisition will be adopted for Advanced LIGO and will be described in Section 5.3.

## 5.2 The Probabilistic Approach to Lock Acquisition in Initial LIGO

It is useful to look at how lock acquisition of a ground based gravitational wave detector has been carried out in the past. Here a summary of the lock acquisition process for Initial LIGO will be given [88, 89]. Recall that Initial LIGO is a power recycled Fabry-Perot Michelson and therefore has only four degrees of freedom (defined in Section 2.7.1) that need to be locked. The lock acquisition is split into five states, which are depicted in Figure 5.2 and described below.

1. In the first state the mirrors are swinging freely as none of the degrees of freedom are being controlled yet. In this state the elements of the sensing matrix are all zero.
2. In the second state the sidebands become resonant inside the power recycling cavity. The REFL error signals ( $I$  and  $Q$ ) are used in a  $2 \times 2$  sensing matrix to control PRCL and MICH. The sideband frequency and power recycling cavity length have been chosen such that the carrier anti-resonance coincides with the sideband resonance. As such the carrier is anti-resonant in the power recycling cavity in this state.
3. In the third state, due to the arm cavities being over-coupled, when each arm cavity becomes carrier resonant, the sign of the reflected carrier field off that cavity flips

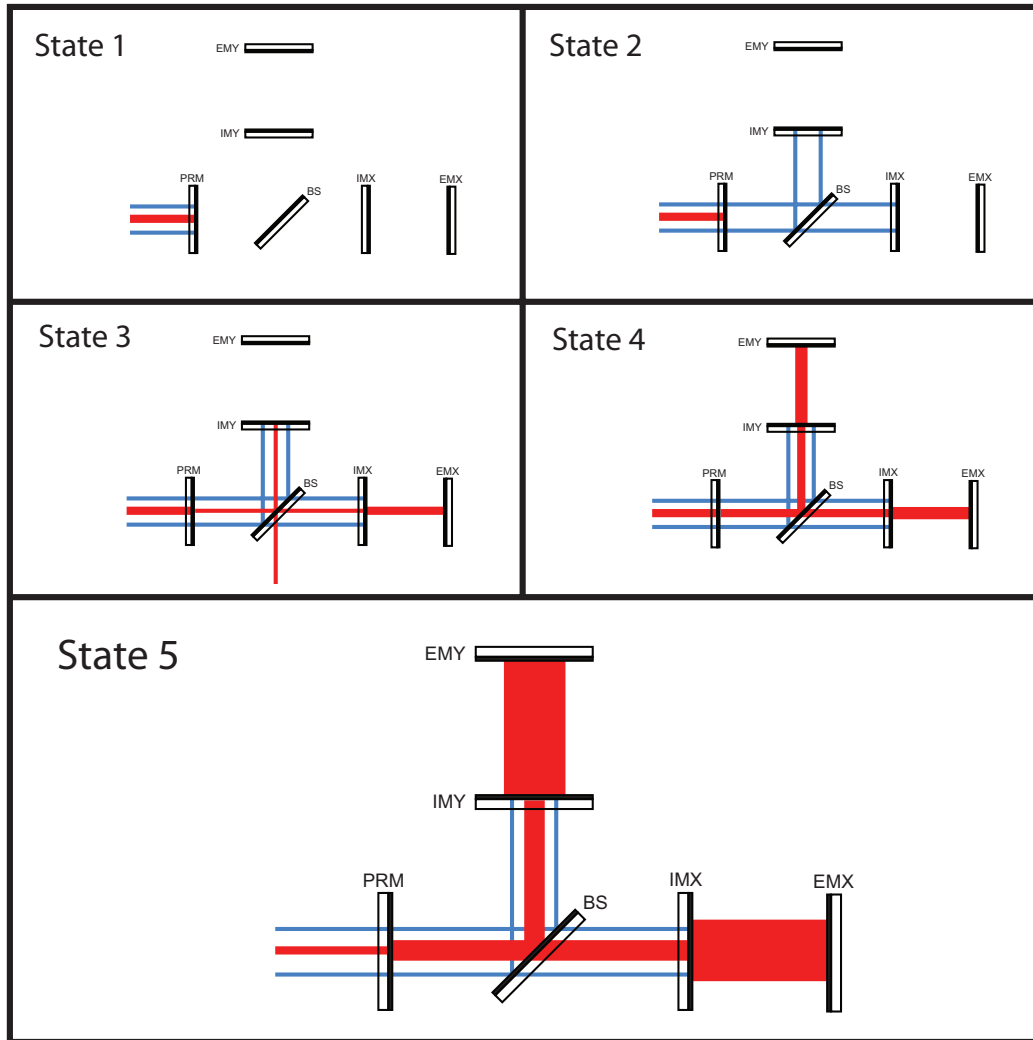


Figure 5.2: The five states of lock acquisition for Initial LIGO (see text for description of these states).

sign. After state 2 has held, if one of the arms flashes through carrier resonance, while the other one remains anti-resonant, the asymmetric port will become bright for the carrier. This arm cavity can be held on resonance, using a combination of the AS-Q error signal and the REFL-I error signal, and feeding back to CARM. The sensing matrix is 3x3 in this state.

4. In the fourth state, the as yet unlocked arm cavity swings through carrier resonance, causing a flip in the sign of the reflected carrier field. With both arm cavities on resonance with the carrier, the power recycling cavity also becomes resonant. Both CARM and DARM degrees of freedom are fed back to, using the REFL, POB and AS error signals to hold both arm cavities on resonance.
5. The final state of lock acquisition, is where the interferometer has survived in state 4 long enough for the power to build up in the coupled cavity (power recycling cavity and arm cavities).

The middle states (2 to 4) in the Initial LIGO lock acquisition are all unstable due to the unlocked degrees of freedom still swinging around, and for the interferometer to achieve full lock, the lock acquisition process needs to happen fast (on the order of a few seconds) so as not to stay in one of the unstable states too long. To do this, various scripts have been written to guide the instrument through the lock acquisition process.

This lock acquisition process is probabilistic, because it depends on certain uncontrollable conditions being met for it to work. One condition is that both of the arms catch lock (in states 3 and 4) as they swing through carrier resonance. If the control system fails to catch the mirrors, the calculated control matrix will be incorrect, and will push the other degrees of freedom off lock. The arms will fail to catch lock if the velocity of the mirrors surpasses the threshold velocity, which would occur at times of high seismic activity. In this respect the ocean driven double frequency microseism [90] is particularly troublesome.

### 5.3 The Deterministic Approach to Lock Acquisition in Advanced LIGO

The addition of the signal recycling mirror will add to the (already considerable) complexity of the control system for Advanced LIGO.

Recall from Section 2.7.2 that the maximum force that the Advanced LIGO actuators can apply to the test masses will be of the order of  $100 \mu\text{N}$  [64], which is considerably weaker than that of the Initial LIGO actuators ( $\sim 25\text{mN}$  [56]). The test masses weigh 40 kg. The threshold velocity is therefore calculated to be only  $\sim 60 \text{ nm/s}$ . The RMS motion of the mirrors (see Figure 2.15) is of the order of  $1 \mu\text{m/s}$ , which is 20 times that of the threshold velocity, meaning that the probability of the arms locking is low.

A probabilistic approach to lock acquisition was taken for Initial LIGO, because the probabilities were high enough to guarantee the lock of the interferometer. In Advanced

LIGO this will not be the case and therefore a more deterministic and robust approach based on a decoupled readout scheme will be implemented.

The main source of lock acquisition destabilisation is due to the arm cavities [91]. Therefore to acquire lock for Advanced LIGO a separate sensing scheme will be used to readout the arm cavities. This scheme will be used to hold the arms off resonance so that they act as perfect reflectors to the science beam. This reduces the lock acquisition problem for the central degrees of freedom to that of a dual recycled short Michelson.

The central degrees of freedom are also decoupled, using the relative field responses between the first and second order modulation sidebands to read out each degree of freedom. For details on this readout technique, referred to as the  $3f_m$  technique, the reader is directed to the technical document [92].

With the arms detuned from resonance and the central cavities locked using the  $3f_m$  technique, the carrier becomes resonant inside the central cavities. The 9 MHz sidebands (see Section 3.5) resonates inside the power recycling cavity only and the 45 MHz sidebands resonate inside the power recycling and the signal recycling cavities. The arm cavities are then tuned onto resonance, which changes the distribution of the carrier power throughout the interferometer dramatically, but as the five degrees of freedom are controlled using error signals mostly independent from the science carrier light<sup>1</sup> the lock remains stable. After the cavities are tuned onto resonance, the control of the interferometer is handed over to the readout scheme described in Section 3.5.

## 5.4 Arm Length Stabilisation

The system that will be used to hold each arm cavity off resonance during the lock acquisition of the central degrees of freedom and then tune them onto resonance, is referred to as the Arm Length Stabilisation (ALS) system. In addition to having to control the detuning of the cavity from resonance, the ALS system has to suppress the RMS fluctuations of the cavity length relative to the science laser frequency, to avoid random flashes though resonance, which are undesirable during the lock acquisition process. Thus the two main requirements [93] of the ALS system are:

1. Efficient control of the cavity tuning over an FSR.
2. Suppression of the RMS fluctuations of the cavity length (relative to the science laser frequency) to less than the line-width ( $\sim 1.3$  nm).

The rest of this section looks at three different techniques proposed for the Advanced LIGO ALS system. The techniques are: the implementation of a suspension point interferometer, digitally enhanced heterodyne interferometry and dual frequency PDH readout. The advantages and disadvantages of each technique are discussed.

---

<sup>1</sup>The carrier to third order interaction has a negligible effect

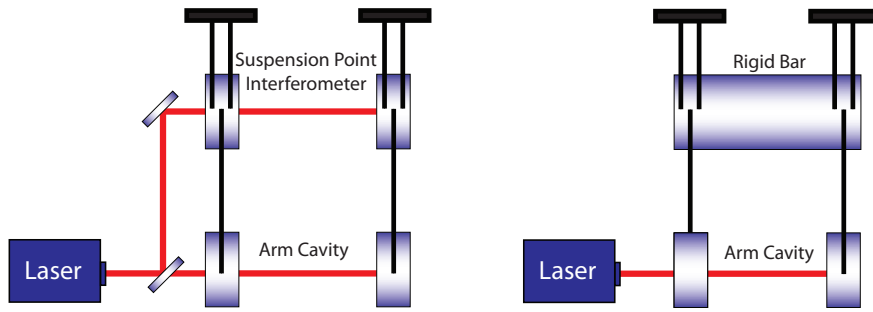


Figure 5.3: The basic idea behind the Suspension Point Interferometer

#### 5.4.1 The Suspension Point Interferometer

A suspension point interferometer (SPI) [94] refers to an auxiliary interferometer made of mirrors from which the gravitational wave interferometer mirrors are suspended from. The standard PDH readout techniques are used to sense the distance between the suspension points of the input and end mirrors in each arm cavity. This PDH readout is fed back to the suspension points, to force the arm cavities of the SPI into resonance. This correlates the motion of the input mirror and end mirror suspension points, thus suppressing the relative motion between the suspension points within the bandwidth of the locking servo. Conceptually, the SPI can be thought of as forming a rigid bar between the suspension points of the arm cavity mirrors.

To meet the ALS requirements, the laser beam used to probe the SPI would need to be phase coherent and offset in frequency with the science laser. To meet the first ALS requirement the optical frequency difference between the auxiliary laser used to interrogate the SPI and the science laser would need to be controllable. To meet the second requirement the auxiliary laser would need to be phase coherent with the science laser. Both requirements can be achieved by means of a phase-locked loop between the lasers or alternatively by sending a tap-off of the science laser light through an acousto-optic modulator (AOM). A simple diagram for one of the arm cavities for the suspension point interferometer is shown in Figure 5.3.

An advantage of an SPI system over the other two techniques is that it is an independent system, and can be run whenever required. It can potentially be run during science mode, and used to improve the seismically limited low frequency band of the detector. A disadvantage is that it requires extra optics to be mounted to the suspension chain, which is quite invasive.

#### 5.4.2 Digitally Enhanced Heterodyne Interferometry

Digitally enhanced heterodyne interferometry (DEHI) [95] is a relatively new technique that combines standard heterodyne interferometry with direct sequence spread spectrum modulation and demodulation using binary Pseudo Random Noise (PRN) codes.

The combination of these two techniques creates an interrogation process that allows

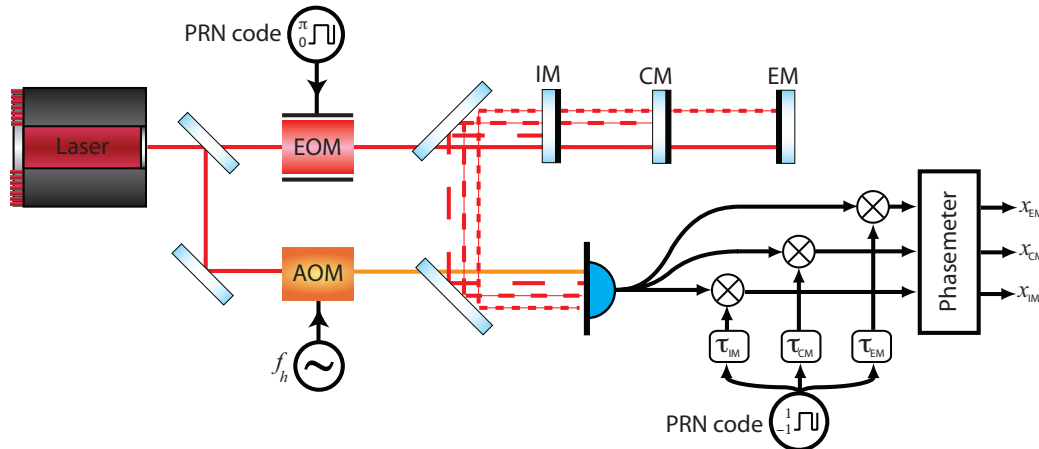


Figure 5.4: Schematic for Digitally Enhanced Heterodyne Interferometry. IM = Input Mirror, CM = Coupling Mirror, EM = End Mirror

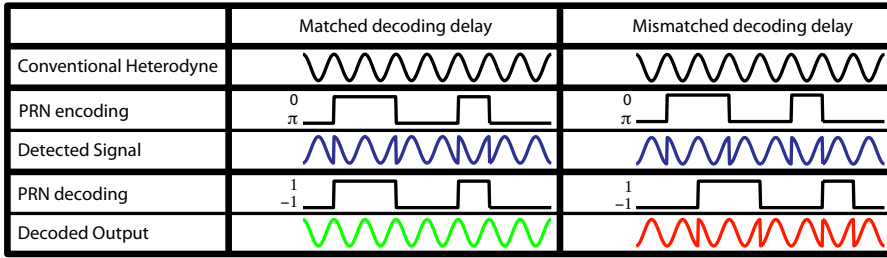


Figure 5.5: A table showing heterodyne signals for PRN encoding and decoding.

isolation of individual reflections based on their optical-electronic propagation delay while retaining the full interferometric sensitivity determined by the optical wavelength.

Consider the optical layout shown in Figure 5.4 for the case of three partial reflectors. The laser beam is split into a local oscillator and probe beam by the beamsplitter. The local oscillator is sent through an Acousto-Optic Modulator (AOM) where it receives a frequency shift,  $f_h$ , so that it can provide a heterodyne signal at the photodetector. The PRN sequence is encoded onto the light by an electro-optic modulator (EOM), which phase shifts the probe beam by either 0 or  $\pi$  before it is sent to interrogate the multi-mirror system. The reflected probe beam is combined with the LO beam to create the PRN encoded heterodyne signal.

The main difference from conventional heterodyne interferometry is the PRN modulation. Without PRN modulation the heterodyne signal is determined by the vector sum of the reflections from all three mirrors and information about the individual mirror positions is lost. With the PRN modulation, the signal from each mirror will possess a time-varying phase shift unique to its time of flight from the EOM.

The effect of the PRN encoding and decoding on the measured signals can be seen in Figure 5.5. Let's consider only the encoding and decoding of the reflection signal from the input mirror. The first row shows the conventional heterodyne signal (no PRN encoding).

The PRN code (2nd row) randomly flips the sign of the amplitude of the heterodyne signal, producing the chopped sine wave (3rd row). For channel 1, the photodetector output is multiplied by the PRN code with a delay ( $\tau_{IM}$ ) matched to the path time from the EOM off the input mirror to the mixer. This matched decoding (4th row), recovers the full heterodyne signal. The phase of this heterodyne signal gives a readout of the mirror displacement.

For channel 2, the decoding delay is matched to the path for the CM reflected beam. The decoding of the encoded signal for the IM reflection in this channel, yields another chopped sine wave, which appears as broadband noise background to the measurement. This broadband noise can be strongly rejected by appropriate filtering and averaging in the phasemeter. It has been demonstrated [95] that each signal can be isolated by adjusting the decoding delay to match the total optical-electronic propagation delay for each optic. An error signal for each cavity can be derived by taking the difference between the measurement for each mirror in the cavity. This error signal can then be fed back to the mirror to suppress the cavity fluctuations relative to the PRN laser.

The DEHI readout technique measures the phase of each mirror directly and as such the error signal is linear over a large range (multiple FSRs). The first ALS requirement can therefore be met by simply injecting an offset into the feedback control loop. The second requirement is met by phase-locking the PRN laser to the science laser.

An advantage of DEHI system is that multiple cavity lengths can be read out using one simple metrology system meaning that it has the potential to handle the whole lock acquisition for a gravitational wave detector and not just the lock of the arms.

A disadvantage of this technique is that it is largely untested.

#### 5.4.3 Dual Frequency Pound Drever Hall

The dual frequency PDH readout scheme involves probing the arm cavity using light from an auxiliary laser at a different optical frequency to that of the science laser. Using light at a different wavelength ensures that it is not detected on the interferometers main port photo-detectors, which are optimised for 1064 nm light.

The relative fluctuations between the frequency of auxiliary laser light and the length of the cavity are read out using the PDH sensing technique. The PDH error signal is fed back to the frequency actuator of the auxiliary laser to lock it to the cavity. The frequency of the auxiliary laser tracks the cavity length and acts as reference. A measurement of the cavity length relative to the science laser can therefore be obtained by measuring the relative frequency fluctuations between the auxiliary and science lasers.

An optical wavelength of 532 nm (green light) is the ideal choice for the auxiliary laser, as it can be generated by frequency doubling 1064 nm light (the wavelength of the science laser light) by means of a second harmonic generator (SHG). This is important in obtaining the relative frequency measurement, as the frequency difference in frequency between 532 nm light and 1064 nm is too fast for any existing photodiode to detect. The 532 nm beam is inherently phase coherent with the 1064 nm beam it is derived

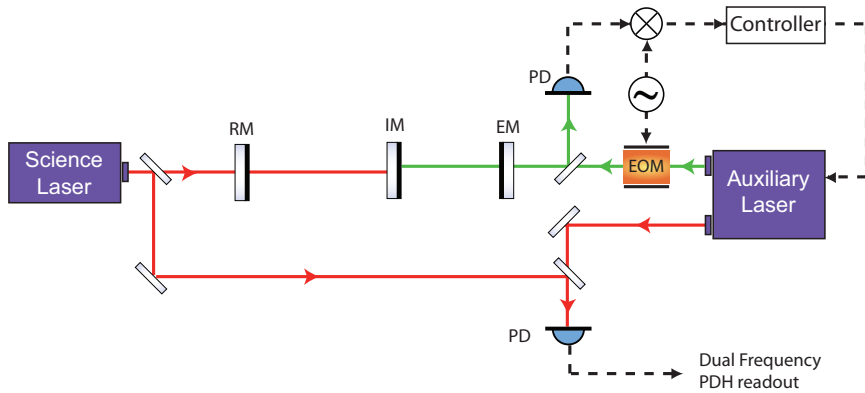


Figure 5.6: The dual frequency PDH readout scheme.

from. Therefore a measurement of the frequency difference between the science laser and the auxiliary laser's 1064 nm beams provides a measurement of the relative fluctuations between the science laser frequency and the cavity length.

Figure 5.6 shows this dual frequency PDH scheme where 532 nm light is injected via the end mirror. The green light is injected through the end mirror to avoid adding more input optics to the interferometer that may impede the standard science PDH scheme. A disadvantage of this scheme is that by choosing to send the auxiliary light through the end mirror, the two lasers will be 4 km apart. As such a comparison between the two beams requires that one of them has to travel 4km to the other station. This can be achieved by sending the science laser beam through an optical fibre, however the fibre may add noise to the science laser frequency and degrade the relative frequency measurement. The transfer of an optical frequency through a fibre is the subject of Chapter 7.

Another disadvantage is that the cavity mirror coatings need to be altered so that they are highly reflective for 532nm light. It was thought that this change to the mirror coatings might increase coating thermal noise, however this was found not to be an issue [96].

The main advantage of this scheme is that the various techniques that make it up, such as PDH, heterodyne detection and second harmonic generation, are well tested.

## 5.5 Summary

This chapter discussed the theory behind the lock acquisition of a gravitational wave detector. The concepts of threshold velocity and a dynamic sensing matrix were introduced and identified as the main difficulties associated with acquiring lock. The probabilistic lock acquisition scheme of Initial LIGO was looked at, followed by a more deterministic lock acquisition scheme suggested for Advanced LIGO.

Importantly this led to the introduction to the Arm Length Stabilisation system, which provides the motivation for the work presented in the remaining chapters of this thesis. In Chapter 6 the results of an experiment testing an ALS system based on dual frequency

PDH readout are presented. In Chapter 7 the transfer of a frequency reference through a fibre is explored.



## Chapter 6

# Dual Frequency PDH Stabilisation Experiment

The following chapter describes an experimental demonstration of an Arm Length Stabilisation (ALS) system using dual frequency PDH readout. This ALS system was used to stabilise a Fabry-Perot cavity formed from two of the Tip Tilt mirrors from Chapter 4.

The dual frequency PDH readout of the cavity length fluctuations relative to the science laser consists of two segments. The first is a feedback control system that locks the frequency of an auxiliary laser to the suspended cavity. The second is a frequency meter that measures the relative frequency between the auxiliary laser and the science laser. Once the dual frequency readout is obtained it is fed back to the cavity length actuator to actively suppress the relative cavity fluctuations. The setup of the experiment can therefore be divided into four steps:

- setting up the cavity.
- implementing a control loop to lock the auxiliary laser to the cavity.
- measuring the relative frequency between the science and auxiliary lasers.
- setting up the the ALS control loop to stabilise the cavity to the science laser.

These steps will be described in the following sections. At the end of the chapter we present results characterising the performance of this dual frequency PDH based ALS system in terms of the cavity tuneability and stability requirements (see Section 5.4). We also present results showing a successful transfer of the control of the cavity between the dual frequency PDH readout and science laser PDH readout. The bench-top configuration of the experiment can be seen in Figure 6.1.

### 6.1 Suspended Test Cavity

The test cavity was formed using two dichroic mirrors (for green and infra-red reflectivity), which were suspended from two of the Tip Tilt stages. The cavity was much shorter than

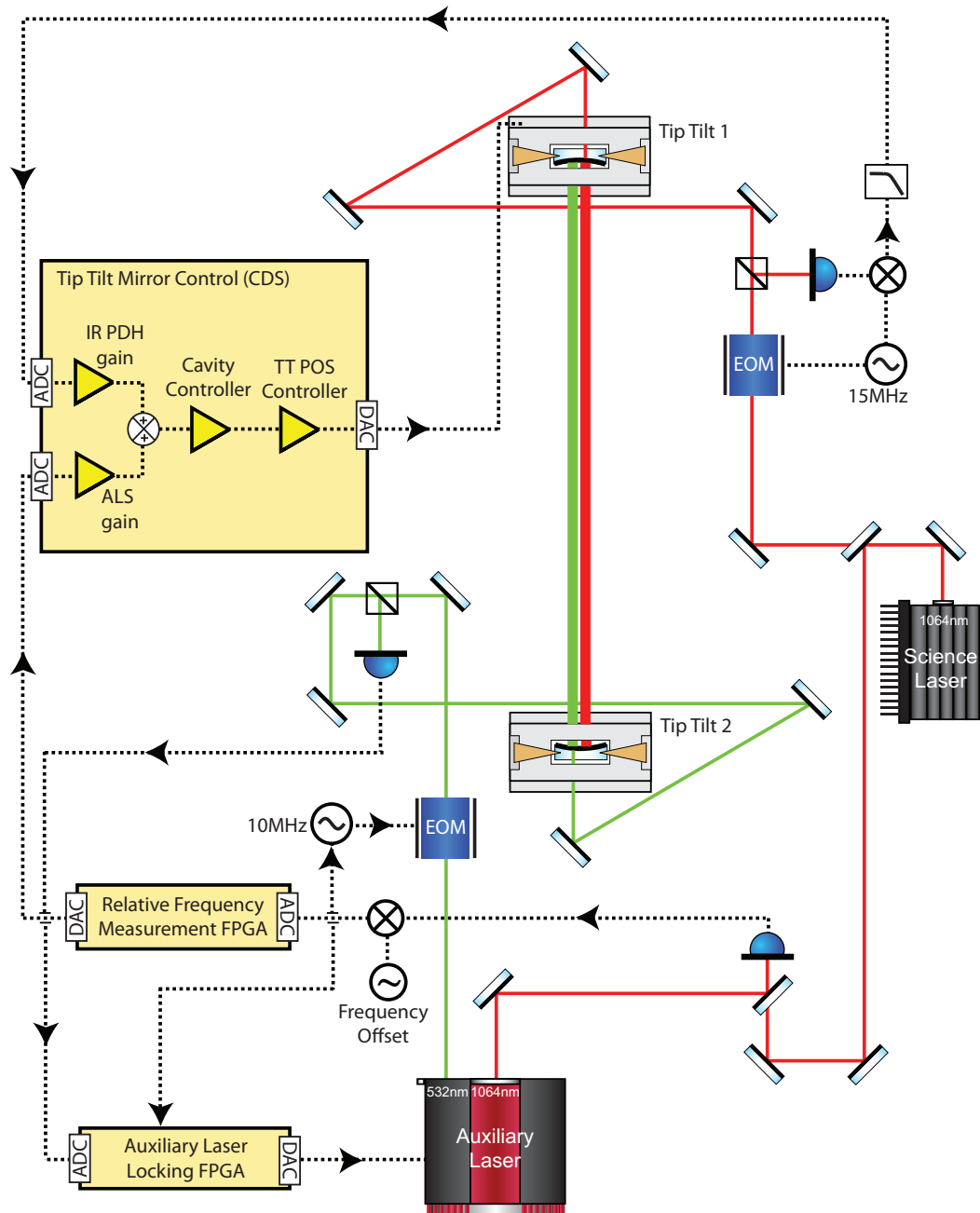


Figure 6.1: The configuration of the experiment for testing the Arm Length Stabilisation scheme using dual frequency PDH readout.

Parameter	Value
Cavity Length	1.3 m
Free Spectral Range	115.3 MHz
Radius Of Curvature TT1	4 m
Radius Of Curvature TT2	4 m
Waist Radius 532nm	499.9 $\mu$ m
Waist Radius 1064nm	706.9 $\mu$ m
Reflectivity 532nm TT1	0.99
Reflectivity 532nm TT2	0.95
Finesse 532nm	102.4
Reflectivity 1064nm TT1	0.98
Reflectivity 1064nm TT2	0.999
Finesse 1064nm	296.3

Table 6.1: The parameters of the Fabry-Perot cavity.

the Advanced LIGO arm cavity, with a length of 1.3m. A disadvantage of having a much shorter cavity is that the free spectral range is considerably larger, at 115.3 MHz, meaning that the cavity resonance needed to be tuned over a much larger frequency range. These issues are discussed further in later sections.

Each mirror had a radius of curvature of 4 m, which was chosen to meet the cavity stability criterion [97], and also to make sure that the higher order Hermite-Gaussian modes don't overlap in frequency with the fundamental Gaussian mode. The Hermite-Gaussian modal spacing is 30.5 MHz. This choice of mirror curvature yields cavity waist radii of 499.9  $\mu$ m and 706.9  $\mu$ m for optical wavelengths of 532 nm and 1064 nm respectively. The science laser's 1064 nm beam and the auxiliary laser's 532 nm beam were both aligned and mode-matched into the cavity via the input optics.

The reflectivities of the cavity mirrors were chosen so that the cavity finesse and therefore the cavity length line-widths would be comparable to that of the Advanced LIGO arm cavity. Specifically the cavity finesse were 102.4 for the 532 nm beam, and 296.3 for the 1064 nm beam. The cavity parameters are listed in Table 6.1.

### 6.1.1 Science PDH readout

A PDH scheme (see Section 3.2) was implemented to provide a direct readout of the cavity length fluctuations relative to the science laser, so that the performance of the dual frequency PDH stabilisation could be evaluated.

The science laser was a diode-pumped solid state laser (JDSU 126), which generated radiation at 1064nm, via a non-planar ring oscillator (NPRO) crystal made of neodymium-doped yttrium aluminium garnet (Nd:YAG) [98]. Phase modulation sidebands were imposed onto the science laser light by sending it through an electro-optic modulator (New

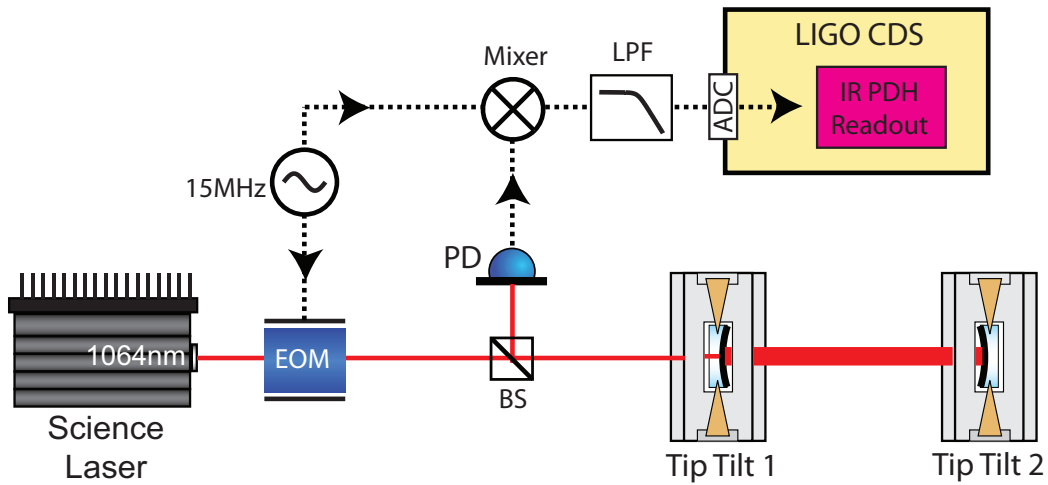


Figure 6.2: Simplified diagram of the Tip Tilt cavity and PDH scheme.

Focus 4003), which was driven at 15 MHz by a signal generator (Agilent 33220A). This phase modulated light was mode-matched and steered into the cavity through Tip Tilt 1, where relative phase shifts were imparted onto the carrier and sideband fields reflected off the cavity.

The reflected light was then detected on a high speed photodetector. The photodetectors RF output was sent to an analog electronic mixer, to be demodulated at 15 MHz by the same signal generator before being passed through a Low Pass Filter with a corner frequency of 20 MHz to remove the  $2\omega_m$  terms. The resulting analog error signal was then digitised and sent into the CDS system (described in Section 4.3).

The error signal (measured in digital counts) at resonance needed to be calibrated to give a readout of cavity length. Typically this is done by linearly scanning the cavity length over at least one FSR (half the optical wavelength) and using the FSR to calibrate the slope of the error signal. This method relies on the assumption that the rate of change of cavity length is constant (constant velocity) and that the displacement noise of the cavity is negligible compared to the scan. These assumptions are invalid with our suspended cavity, where the cavity noise is on the order of  $1 \mu\text{m}$  (twice the FSR), and a linear scan with the Tip Tilt actuators is difficult.

Instead the higher linearity laser frequency actuator was scanned with a triangular signal at 5 Hz, which is faster than the pendulum resonance frequency of the suspended mirrors ( $\sim 1.3$  Hz) where most of the cavity displacement noise occurs. A ten second trace of the error signal was recorded and is shown in Figure 6.3(a). To show the characteristic shape of the error signal around carrier and sideband resonances, a zoomed in trace is shown in Figure 6.3(b).

Although, the frequency scan is approximately linear, the displacement noise of the cavity, still means that the rate of change over an FSR is likely to be non-linear. The scan over the carrier and sideband resonances is more linear, and since the spacing between each sideband and the carrier is known to be 15 MHz (the modulation frequency), the

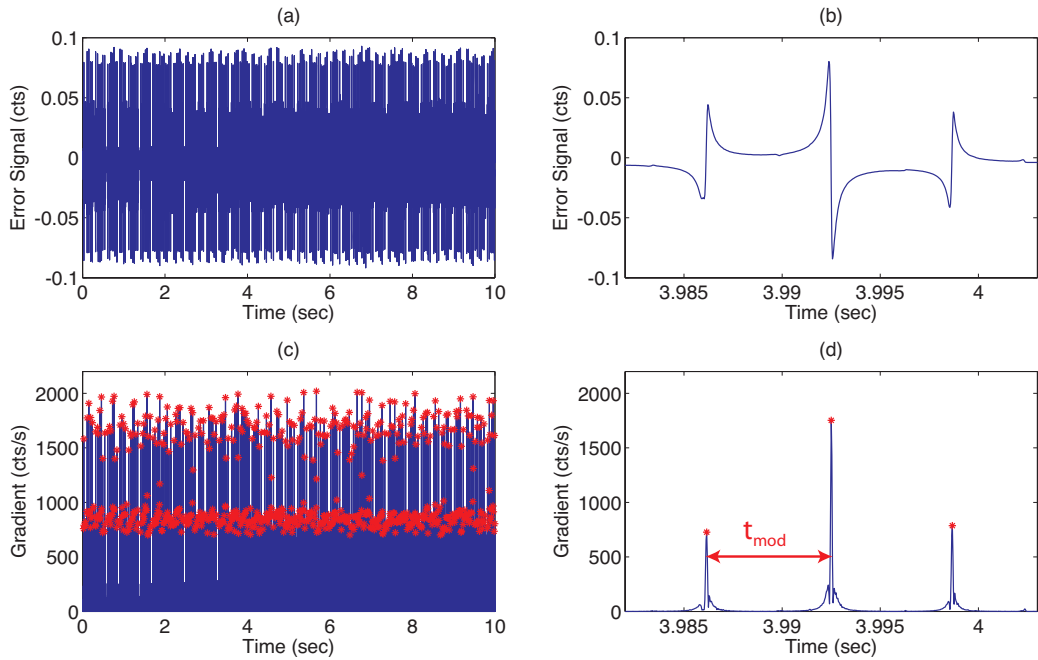


Figure 6.3: Calibration of the error signal. (a) full 10s trace of the error signal (b) zoomed in error signal around the carrier and sideband resonance (c) the absolute gradient of the error signal over 10s and (d) the absolute gradient of the zoomed in error signal.

slope in counts/Hz can be calculated from the following equation:

$$S_\nu = \left( \frac{d\varepsilon}{d\nu} \right) = \left( \frac{d\varepsilon}{dt} \right) \times \left( \frac{t_{mod}}{\nu_{mod}} \right) \quad (6.1)$$

where  $t_{mod}$  is the time taken to sweep between the carrier and sideband, and  $\nu_{mod} = 15$  MHz is the modulation frequency.

A calibration script was written in Matlab [87], that calculated and plotted the absolute gradient (with respect to time) of the uncalibrated error signal (see Figure 6.3(c)). The script used a peak finding algorithm to find the various resonances which correspond to maxima in the error signal gradient. The carrier and sideband resonances were found based on their relative spacings (see Figure 6.3(c)), in that if the spacing between the carrier and lower sideband differed from that of the carrier and upper sideband by more than some threshold value, then they were rejected from the analysis. The gradient of the remaining carrier resonances were calibrated in terms of frequency (counts/Hz) and averaged. Using this calibration code the error signal slope at resonance was found to be:

$$S_\nu = 6.33 \times 10^{-7} \text{ cts/Hz} \quad (6.2)$$

The calibration in terms of cavity displacement (counts/m) and cavity roundtrip phase (counts/rad) are easily calculated from the frequency to error signal calibration, using the cavity roundtrip phase. They were found to be:

$$S_L = 1.37 \times 10^8 \text{ cts/m} \quad (6.3)$$

$$S_\phi = 11.6 \text{ cts/rad} \quad (6.4)$$

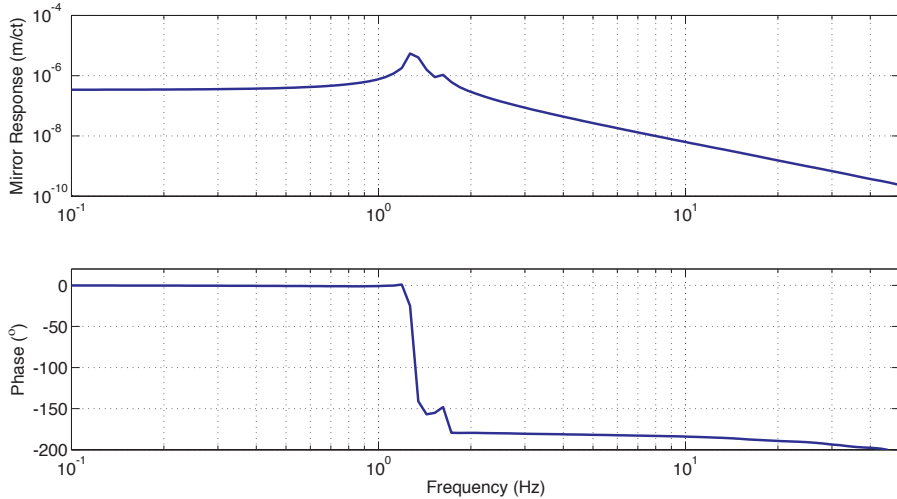


Figure 6.4: The position response of Tip Tilt 1 to a signal from the CDS.

The standard deviation in the above values found from the calibration code was approximately 9 %.

### 6.1.2 Tip Tilt actuation

The actuation of the cavity length was carried out by varying the position of Tip Tilt 1 via the voice coil actuators. This Tip Tilt was not the same as the prototype Tip Tilt characterised in Chapter 4 and therefore its position response was re-measured using the methods from Section 4.4.2. The position to shadow sensor readout was found to be:

$$S_{sspos} = 81 \times 10^6 \text{ cts/m} \quad (6.5)$$

The difference between this value and that of the prototype Tip Tilt (see Equations 4.7) is due to a difference in the gain of each trans-impedance stage. The measured position response is shown in Figure 6.4. It follows the typical pendulum response, remaining flat below the pendulum resonance ( $\sim 1.3$  Hz), and rolling off as  $f^{-2}$  above it.

## 6.2 Locking the Auxiliary Laser to the Cavity

The first part of the dual frequency PDH readout scheme is to lock the auxiliary laser to the cavity, so that the frequency fluctuations follow the cavity length fluctuations. This involves setting up a feedback control system where the cavity roundtrip phase is sensed using the PDH technique and fed back to the frequency actuator of the auxiliary laser via a controller, which filters and amplifies the signal. This auxiliary-laser locking loop is depicted in Figure 6.5.

The auxiliary laser locking loop in Figure 6.5 can be represented by a block diagram shown in Figure 6.6. Here  $\Delta L_{cav}(\omega)$  represents frequency dependent fluctuations in the cavity length,  $\Delta\nu_{aux,gr}(\omega)$  represents the fluctuations in the frequency of the green light from the auxiliary laser,  $\Delta\phi_{crt}(\omega)$  represents the fluctuations in the cavity roundtrip phase,

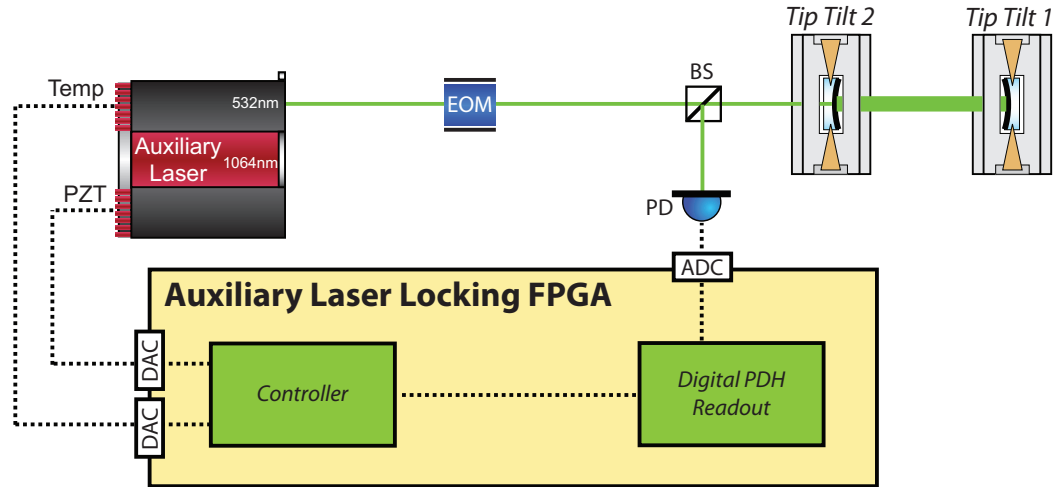


Figure 6.5: Schematic of the auxiliary laser locking loop.

$\Delta\epsilon(\omega)$  represents the fluctuations in the PDH error signal and  $\Delta\eta_{aux,gr}(\omega)$  represents all external disturbances to the auxiliary laser's frequency. The main components are the PDH sensor represented by  $S_\phi(\omega)$ , the controller for the auxiliary laser locking loop represented by  $C_{all}(\omega)$  (the negative sign represents negative feedback) and the actuator of the auxiliary laser's frequency (for the green laser) represented by  $A_{aux,gr}(\omega)$ .

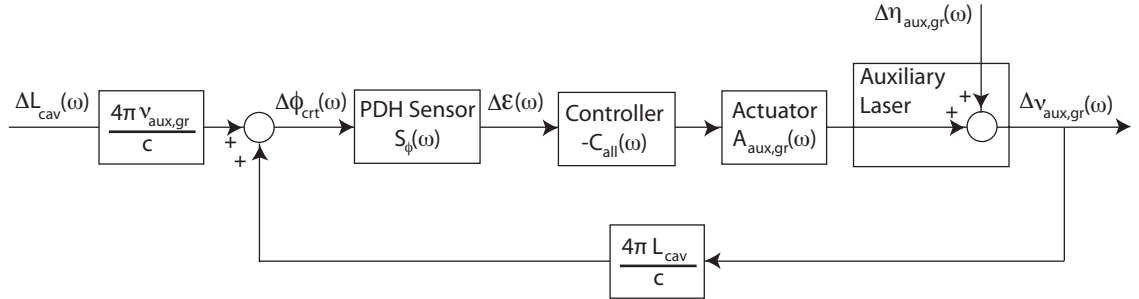


Figure 6.6: Block diagram of the auxiliary laser locking loop. The various components and signals are described in the text.

For small variations in the cavity round-trip phase near resonance, the dependence of the PDH error signal is approximately linear. This is represented by the equation:

$$\Delta\epsilon = S_\phi \Delta\phi_{crt} \quad (6.6)$$

where  $S_\phi$  is the response of the error signal to the roundtrip phase on resonance. Note that when the control loop is closed properly, the feedback signal (PDH error signal) will be suppressed to some small value ensuring that the variations in the round-trip phase are sufficiently small. Variations of the cavity roundtrip phase are a result of fluctuations in the laser frequency and the cavity length via the equation:

$$\Delta\phi_{crt}(\omega) = \frac{4\pi}{c} (L_{cav} \Delta\nu_{aux,gr}(\omega) + \nu_{aux,gr} \Delta L_{cav}(\omega)) \quad (6.7)$$

where  $L_{cav}$  is the length of the cavity,  $\nu_{aux,gr}$  is the frequency of the green light from the auxiliary laser and a preceding ‘ $\Delta$ ’ represents fluctuations of that parameter. When the auxiliary locking loop is closed, the fluctuations in the laser frequency  $\Delta\nu_{aux,gr}$ , will be related to the fluctuations in the cavity length  $\Delta L_{cav}$  and the external disturbance  $\Delta\eta_{aux,gr}$ , via the following equation:

$$\begin{aligned}\Delta\nu_{aux,gr}(\omega) = & \left( \frac{-\frac{4\pi}{c}S_\phi(\omega)C_{all}(\omega)A_{aux,gr}(\omega)}{1 + \frac{4\pi}{c}S_\phi(\omega)C_{all}(\omega)A_{aux,gr}(\omega)L_{cav}} \right) \nu_{aux,gr}\Delta L_{cav}(\omega) \\ & + \left( \frac{1}{1 + \frac{4\pi}{c}S_\phi(\omega)C_{all}(\omega)A_{aux,gr}(\omega)L_{cav}} \right) \Delta\eta_{aux,gr}(\omega)\end{aligned}\quad (6.8)$$

The total gain of the various stages in the loop can be represented by the open loop gain ( $OLG$ ) for the auxiliary locking loop, given by:

$$OLG_{all}(\omega) = \frac{4\pi}{c}L_{cav}S_\phi(\omega)C_{all}(\omega)A_{aux,gr}(\omega)\quad (6.9)$$

Equation 6.8 can be simplified by representing it in terms of the open loop gain:

$$\begin{aligned}\Delta\nu_{aux,gr}(\omega) = & \left( \frac{-OLG_{all}(\omega)}{1 + OLG_{all}(\omega)} \right) \left( \frac{\nu_{aux,gr}}{L_{cav}} \right) \Delta L_{cav}(\omega) \\ & + \left( \frac{1}{1 + OLG_{all}(\omega)} \right) \Delta\eta_{aux,gr}(\omega)\end{aligned}\quad (6.10)$$

In the high open loop gain limit ( $OLG_{all}(\omega) \gg 1$ ), Equation 6.10 approximates to:

$$\Delta\nu_{aux,gr}(\omega) = -\left( \frac{\nu_{aux,gr}}{L_{cav}} \right) \Delta L_{cav}(\omega)\quad (6.11)$$

Therefore provided the open loop gain is sufficiently high, the feedback loop will force the auxiliary laser frequency to track the cavity length fluctuations. Generally this occurs at frequencies below the unity gain frequency of the control loop.

Since the auxiliary laser needed to act as a reference for the cavity length fluctuations at frequencies for which we wished to stabilise the cavity to the science laser, the unity gain frequency of the auxiliary locking loop needed to be much higher than that of the ALS loop. This was achieved by implementing the PDH readout and controller digitally on a Field Programmable Gate Array (FPGA). The FPGA is readily re-programmable hardware that provides high speed processing making it ideal for low latency feedback control systems. The bandwidth achievable with a similar digital PDH locking scheme has been demonstrated to be 20 kHz [99], making it suitable for our auxiliary locking loop. The same bandwidth could have been achieved with an analog system, however the FPGA’s flexibility and automation made it a more convenient choice for this experiment.

### 6.2.1 Auxiliary Laser

The auxiliary laser (Innolight Prometheus) used in the experiment was another diode-pumped (Nd:YAG) laser. The infrared radiation at 1064 nm produced by the Nd:YAG

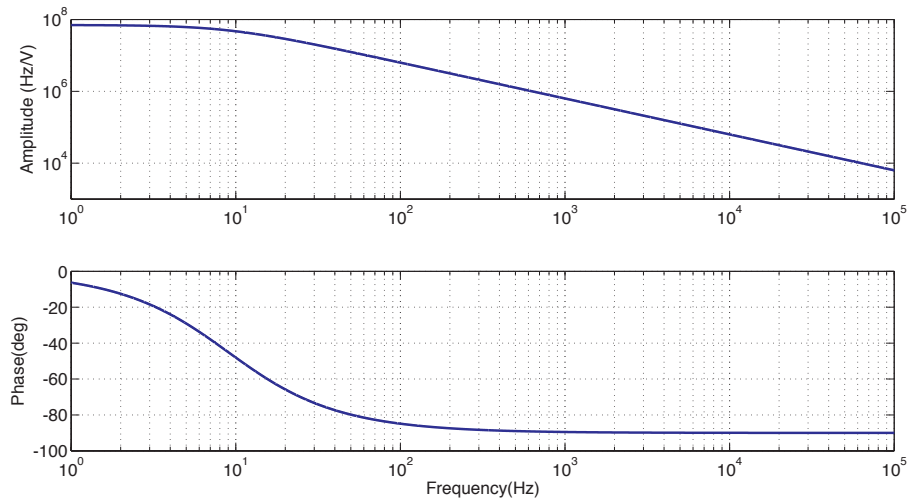


Figure 6.7: The frequency response of the auxiliary laser’s green frequency to a voltage sent through the high voltage amplifier into the auxiliary laser PZT.

crystal was focused into a second harmonic generator (SHG) to also produce green radiation at 532nm. The Prometheus therefore produces dual frequency radiation that is intrinsically phase related.

The laser frequency is controlled by two actuators. Fast (up to a 100 KHz) but short range frequency actuation is handled by a piezo-electric transducer (PZT), which exerts pressure on the Nd:YAG crystal. Slow but large range frequency actuation, is achieved by controlling the temperature of the crystal. The temperature actuator was used only to correct for drifts on timescales of 100 seconds or more, (less than 0.01 Hz), ensuring that the PZT didn’t saturate.

The laser frequency to PZT voltage coefficient’s are:

$$C_{aux-ir} = 1.85 \text{ MHz/V} \quad (6.12)$$

$$C_{aux-gr} = 3.70 \text{ MHz/V} \quad (6.13)$$

where  $C_{aux-ir}$  is the infra-red frequency’s coefficient, and  $C_{aux-gr}$  is the green frequency’s coefficient, which is simply twice that of the infra-red.

The PZT can take an input of  $\pm 100$  V, however the output from the DAC of the digital controller has a range of  $\pm 10$  V. A high voltage (HV) amplifier was therefore included after the DAC and before the laser PZT input, to increase the frequency range. This HV amplifier provided a gain of 20 and also contained a low pass filter with a corner frequency of 9 Hz, which was included to help roll off the open loop gain and reduce noise related to the glitch energy of the DAC. A bode plot of the modelled gain of the laser’s infra-red frequency response to the voltage input of the HV amplifier is provided in Figure 6.7.

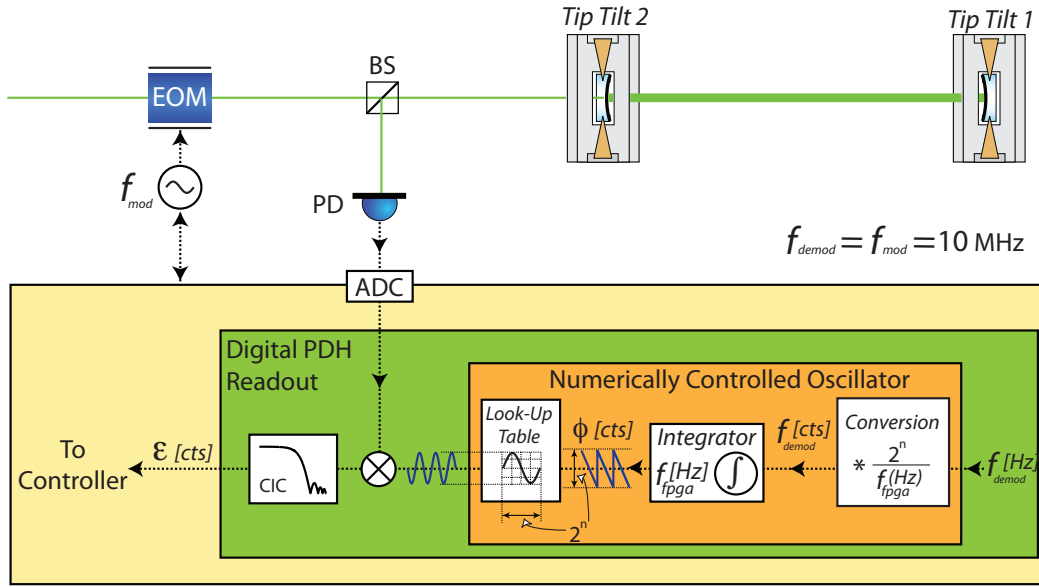


Figure 6.8: Diagram showing the digital PDH readout.

### 6.2.2 Digital PDH readout

The digital PDH scheme for readout of the auxiliary laser's frequency relative to the cavity length is shown in Figure 6.8. The green laser light was sent through an electro-optic modulator, driven by a signal generator (Agilent 33250A) at a modulation frequency of  $f_{mod} = 10 \text{ MHz}$ , before being injected into the cavity through Tip Tilt 2 (the opposite end to the science laser beam). The reflected modulated light was then shone onto a high speed photo-detector.

The photo-detector output was digitised by an Analog to Digital Converter (ADC) which sampled the signal at a frequency of 40 MHz. This digitised signal was sent to an FPGA (NI-PXI-7833R) where the demodulation and filtering was carried out. A LabVIEW interface was used to program the FPGA, which was run at 40 MHz, to match the ADC sampling frequency.

On the FPGA, the digitised signal was mixed with a numerically controlled oscillator (NCO), also at 10 MHz, to demodulate the signal and bring it down to base-band. The NCO (shown in Figure 6.8) was produced by sending a frequency value to an integrator, which gives out a phase value that is fed into a look up table (LUT) of a sine wave. Provided the input frequency value was calibrated correctly the produced signal would oscillate at the given frequency. The calibration was given by:

$$f(\text{cts}) = \frac{2^n(\text{cts})}{f_{\text{fpga}}(\text{Hz})} f(\text{Hz}) \quad (6.14)$$

where  $n$  is the bit depth of the phase register, and  $f_{\text{fpga}}$  is the frequency of the FPGA. For correct demodulation down to baseband, the NCO needed to be synchronised with the signal generator that provided the modulation frequency. This was achieved by phase-locking the FPGA master clock to the signal generator clock using the 10 MHz reference

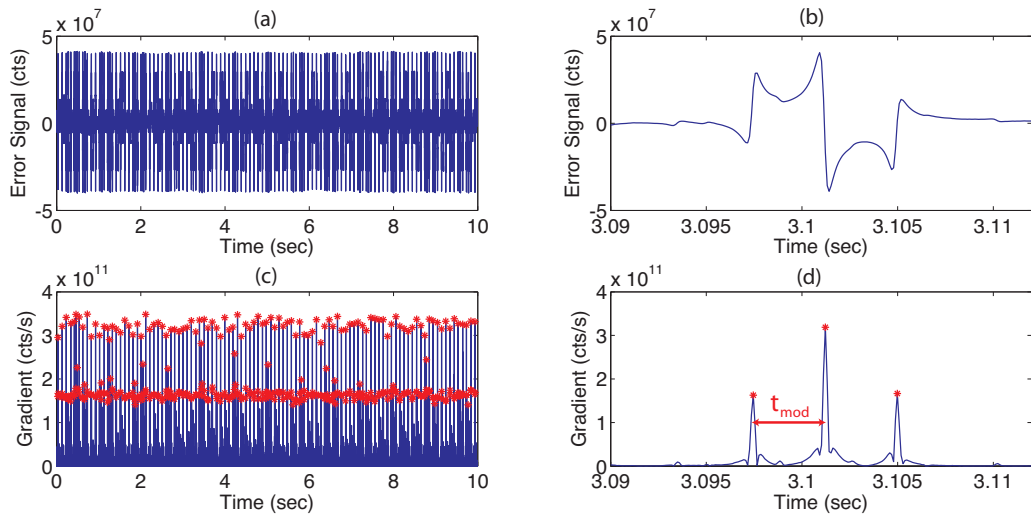


Figure 6.9: Calibration of the digital PDH error signal. (a) full 10 second trace of the error signal (b) zoomed in error signal around the carrier and sideband resonance (c) the absolute gradient of the error signal over the full 10 seconds and (d) the absolute gradient of the zoomed in error signal.

clock.

The output of the mixer was sent through a 40 point cascaded integrator comb (CIC) filter. The CIC would integrate the input for 40 samples, and then output the integrated value. It therefore decimated the 40 MHz sampled signal down to 1 MHz, which was the output frequency of Digital to Analog Converter (DAC). In the frequency domain the CIC is a sinc function, and therefore acts simultaneously as a low pass filter, which is important for removing the  $2f_{mod}$  terms that are present from the mixing process.

The on-resonance digital PDH error signal was calibrated using the method discussed in the science laser PDH section (Section 6.1.1). The auxiliary laser frequency was scanned and a time series of the error signal was taken. The traces of the error signal and error signal gradient are plotted in Figure 6.9. The digital PDH error signal responses to the laser frequency, roundtrip phase and cavity length were:

$$S_\nu = 120 \text{ cts/Hz} \quad (6.15)$$

$$S_\phi = 2.20 \times 10^9 \text{ cts/rad} \quad (6.16)$$

$$S_L = 5.20 \times 10^{16} \text{ cts/m} \quad (6.17)$$

### 6.2.3 Auxiliary Laser Locking Controller

The auxiliary laser control loop was completed by feeding the digital PDH error signal to the auxiliary laser PZT actuator via the digital controller, and thereby locking the frequency of the auxiliary laser to the cavity length. The controller for the auxiliary locking loop was based on the digital PDH error signal slope and auxiliary laser PZT frequency response, and designed to give a loop bandwidth on the order of 10 kHz, (known to be

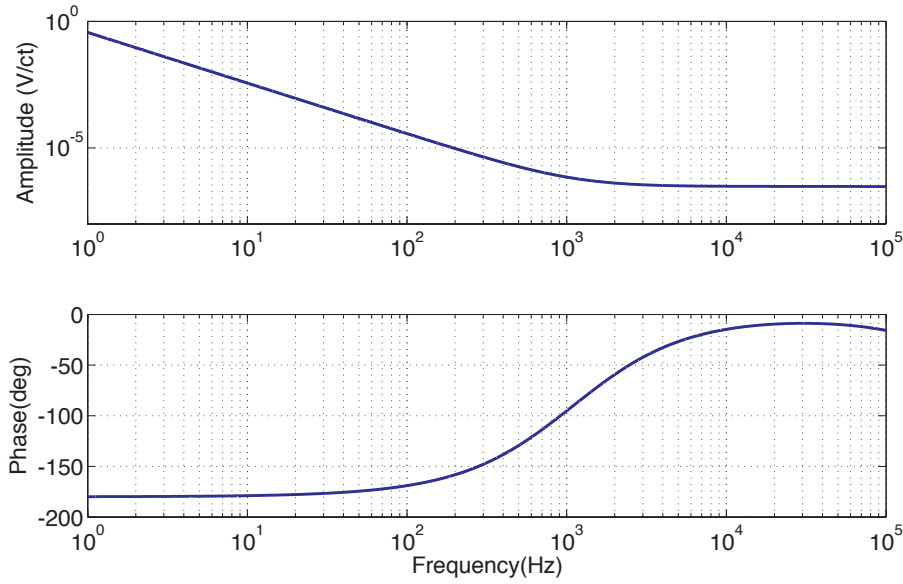


Figure 6.10: The gain of the controller for the auxiliary locking loop. The DAC conversion is included in the gain of the controller.

achievable from [99]), and high gain at DC. To achieve large gain at lower frequencies while ensuring that the loop gain rolled off as  $1/f$  through the desired unity gain frequency, two proportional-integrator stages in series were employed with corner frequencies of approximately 450 Hz and 900 Hz respectively. The gain of the controller was modelled in Matlab [87] and is plotted in Figure 6.10. This response incorporates the DAC conversion from counts to volts. The phase rolls back up near  $0^\circ$  above 10 kHz, allowing for the  $-90^\circ$  provided by the low pass filter in the HV amplifier, so as to provide enough phase margin for a stable locking system.

The total open loop gain was modelled based on the error signal, controller and actuator; and measured using a spectrum analyser (Stanford Research Systems SR787). To obtain the measurement, the spectrum analyser was used to send a swept sine signal into the loop and measure the ratio between the output signal before and after the input signal, while the loop was closed. The gain of the loop is high at low frequencies, which resulted in the output signal measured after the input, being suppressed below the electronic noise floor of the spectrum analyser. As such the gain could only be measured accurately for frequencies above 500 Hz.

The measured and modelled open loop gains are plotted in Figure 6.11 (a). The latency of the modelled open loop was fitted, so that the phase roll off would match that of the measurement. This latency was found to be  $5.7\mu\text{sec}$ . The unity gain frequency of the loop was measured at 12.6 kHz, the phase margin was  $50^\circ$  and the gain margin 9.7 dB.

From Equation 6.10, the open loop gain, the cavity length and the frequency of the auxiliary laser, the response of the auxiliary laser frequency to fluctuations in the cavity length can be calculated. We define this response as  $G_{all}$ , which from Equation 6.10 is

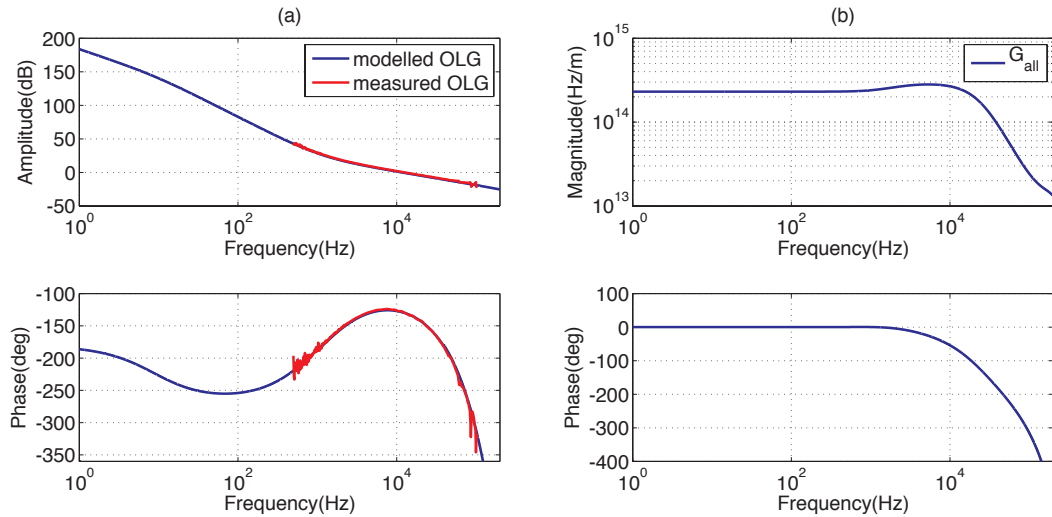


Figure 6.11: Bode plots for (a) the modelled and measured open loop gain (OLG) for the auxiliary laser locking loop and (b) the modelled response of the auxiliary laser frequency to the cavity length.

given by:

$$G_{all} = \frac{OLG_{all}}{1 + OLG_{all}} \frac{\nu_{aux,ir}}{L_{cav}} \quad (6.18)$$

Note that this is the response of the infrared frequency to the cavity length and not that of the green frequency. This response has been modelled and is plotted in Figure 6.11(b), and it shows that the auxiliary laser frequency should reference the cavity length fluctuations for frequencies up to approximately 10 kHz, which will be sufficient for the ALS system.

### 6.3 Relative Frequency Measurement

The second part of the dual frequency PDH readout scheme is to sense the relative frequency fluctuations between the science and auxiliary laser. As the auxiliary laser frequency is sufficiently locked to the cavity length, this readout is an indirect measurement of the cavity length fluctuation relative to the science laser frequency.

As mentioned in Chapter 5, for Advanced LIGO, measuring the relative frequency between the lasers is non-trivial due to the large distance between the lasers. In our bench-top experiment however we did not have the complication of having to send light from one of the lasers over 4 km, as the two lasers were co-located.

To measure the relative frequency between the two lasers, the infra-red light from each laser was interfered on a common photo-detector to produce a heterodyne signal, as depicted in Figure 6.12. This photo-detector was built in house [100] and had a flat frequency response up to 600 MHz. The frequency of the resulting heterodyne signal is given by:

$$\nu_{het}(\omega) = \nu_{sci}(\omega)e^{-i\omega\tau_{sci}} - \nu_{aux}(\omega)e^{-i\omega\tau_{aux}} + \nu_{op,sci}(\omega) - \nu_{op,aux}(\omega) \quad (6.19)$$

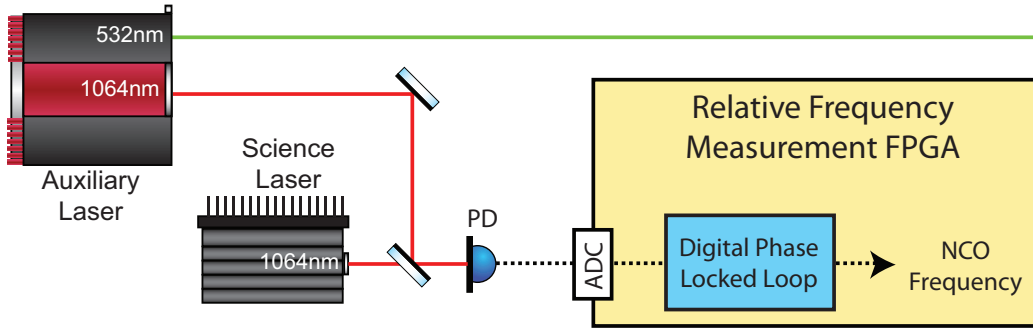


Figure 6.12: The setup for obtaining the relative frequency measurement between the two lasers.

where  $\tau_{sci}$  and  $\tau_{aux}$  are the travel times from the lasers to the photo-detector.  $\nu_{op,sci}$  and  $\nu_{op,aux}$  represent frequency modulations incurred onto the two light fields from fluctuations in the optical paths of the two lasers to the photo-detector.

For our experiment the travel times from the lasers to the photodetector are relatively short ( $\approx 1$  ns), which is much less than the inverse of the Fourier frequency range of interest ( $\approx 1$  ms), meaning that the  $e^{-i\omega\tau}$  terms approximate to unity. We also assume that the fluctuations in the optical path are negligible. Equation 6.19 therefore reduces to:

$$\nu_{het}(\omega) = \nu_{sci}(\omega) - \nu_{aux}(\omega) \quad (6.20)$$

meaning that a measurement of the frequency of the heterodyne signal, equates to a measurement of the relative frequency between the two lasers.

### Digital Phase Locked Loop

The heterodyne frequency was read-out by a frequency meter based on a digital phase locked loop (DPLL). A diagram showing the basic components of the DPLL is shown in Figure 6.13. The DPLL which is implemented on an FPGA, essentially works by phase-locking an NCO (like the one described in section 6.2) to the digitised heterodyne signal. The measurable frequency of the NCO tracks that of the heterodyne signal and therefore provides a readout of the heterodyne frequency.

The two signals are multiplied, and then low pass filtered using an 80 point CIC filter, to produce a quadrature error signal  $\varepsilon_Q$ , which is equal to:

$$\varepsilon_Q = S_{mix} \sin(\phi_{het} - \phi_{nco}) \quad (6.21)$$

where  $S_{mix}$  equals the amplitudes of the digitised heterodyne and NCO signals (in counts), and the CIC filter response.  $\phi_{het}$  is the phase of the heterodyne signal and  $\phi_{nco}$  is the phase of the NCO. Note that the phase of a signal is the integral of the frequency of that signal. In the frequency domain the phase of the heterodyne and NCO signals are given by:

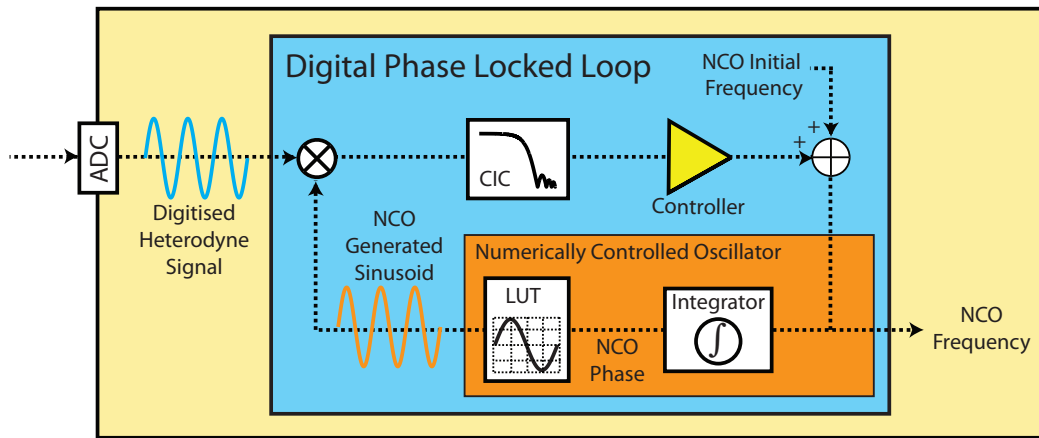


Figure 6.13: Diagram of the Digital Phase Locked Loop

$$\phi_{het}(\omega) = \frac{2\pi}{i\omega} \nu_{het}(\omega) \quad (6.22)$$

$$\phi_{nco}(\omega) = \frac{2\pi}{i\omega} \nu_{nco}(\omega) \quad (6.23)$$

where  $\phi_{het}$  and  $\phi_{nco}$  have units of radians and  $\nu_{het}$  and  $\nu_{nco}$  have units of Hertz. Provided the frequencies are the same and the phase difference is small ( $\phi_{het} \approx \phi_{nco}$ ), the small angle approximation means that the quadrature error signal in Equation 6.21 reduces to something proportional to the phase difference:

$$\varepsilon_Q = S_{mix}(\phi_{het} - \phi_{nco}) \quad (6.24)$$

The frequency of the NCO is controllable and can be set to equal the frequency of the heterodyne signal, however the frequency of the heterodyne signal varies as the frequency of each laser fluctuates (especially the auxiliary laser which is locked to the cavity). So to ensure that the frequency of the NCO tracks that of the heterodyne signal, the quadrature error signal is fed back via a controller as a correction to the NCO frequency. This also drives the phase difference to a small value and ensures that the small angle approximation is met. The controller is just a simple Proportional-Integral stage. A block diagram representing the DPLL is drawn in Figure 6.14 to depict just how the output tracks the frequency of the heterodyne signal.

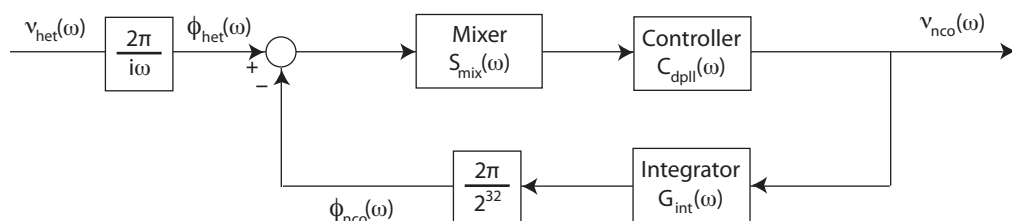


Figure 6.14: A block diagram of the DPLL

$C_{dpll}$  is the gain of the proportional-integrator controller.  $G_{int}$  is the gain of the 80 MHz integrator which can be approximated for  $\omega \ll \omega_s$  by the equation:

$$G_{int}(\omega) \approx \frac{80 \times 10^6}{i\omega} \quad (6.25)$$

The factor of  $2\pi/2^{32}$  represents the mapping of the 32-bit integer to the one cycle of a sine wave contained in the LUT. An equation for the frequency of the NCO in terms of the heterodyne frequency can be written:

$$\nu_{nco}(\omega) = \left( \frac{S_{mix}(\omega)C_{dpll}(\omega)}{1 + S_{mix}(\omega)C_{dpll}(\omega)G_{int}(\omega) \left( \frac{2\pi}{2^{32}} \right)} \right) \left( \frac{2\pi}{i\omega} \right) \nu_{het}(\omega) \quad (6.26)$$

The open loop gain of the DPLL is given by the gains of all the blocks in the control loop in Figure 6.14:

$$OLG_{dpll}(\omega) = S_{mix}(\omega)C_{dpll}(\omega)G_{int}(\omega) \left( \frac{2\pi}{2^{32}} \right) \quad (6.27)$$

Substituting Equation 6.27 into Equation 6.26, gives:

$$\nu_{nco}(\omega) = \left( \frac{OLG_{dpll}(\omega)}{1 + OLG_{dpll}(\omega)} \right) \left( \frac{2^{32}}{G_{int}(\omega)} \right) \left( \frac{1}{i\omega} \right) \nu_{het}(\omega) \quad (6.28)$$

And substituting the integrator response from Equation 6.25 into Equation 6.28, yields:

$$\nu_{nco}(\omega) = \left( \frac{OLG_{dpll}(\omega)}{1 + OLG_{dpll}(\omega)} \right) \left( \frac{2^{32}}{80 \times 10^6} \right) \nu_{het}(\omega) \quad (6.29)$$

The open loop gain of the DPLL was modelled in Matlab [87] based on the known gains of the various stages. The bode plot is provided in Figure 6.15 (a) along with a bode plot of the closed loop response ( $OLG_{dpll}/(1 + OLG_{dpll})$ ). The unity gain frequency of the loop was found to be 63 kHz, the gain margin was 12.3 dB and the phase margin was 58°. The frequency meter gain is defined as the response of the NCO frequency readout to the heterodyne frequency, and is given by:

$$G_{fm} = \left( \frac{OLG_{dpll}(\omega)}{1 + OLG_{dpll}(\omega)} \right) \left( \frac{2^{32}}{80 \times 10^6} \right) \quad (6.30)$$

The frequency meter response was measured by locking the NCO to a sine wave generated from a signal generator. A swept sine from the SR787 spectrum analyser was used to modulate the frequency of this sine wave and the frequency meter output was read out. The calibrated response is plotted in Figure 6.15 (b) along with the modelled frequency meter response obtained from the DPLL open loop gain model. The latency of the modelled frequency meter had to be fitted. Apart from this fitted latency, there was excellent agreement between the measurement and model. The frequency meter response in Figure 6.15 (b) shows that for closed loop operation the fluctuations in the relative frequency can be measured up to  $\sim 10$  kHz with phase delay of less than or equal to 19°. This is more than sufficient for dual frequency PDH readout.

A 10 second trace of the relative frequency between the two lasers was recorded, while the auxiliary laser was locked to the cavity. This trace is plotted in Figure 6.16 and

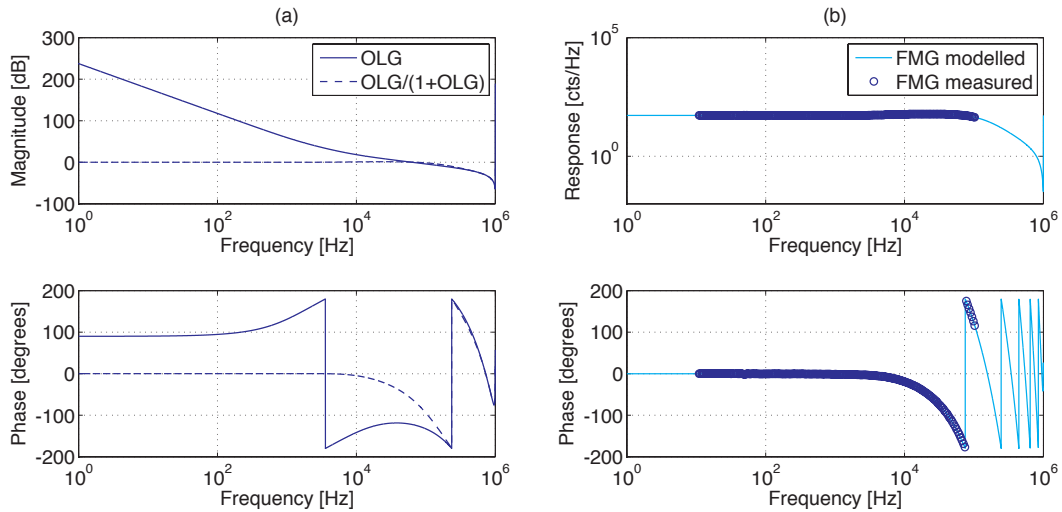


Figure 6.15: (a) The modelled open loop gain (OLG) of the DPLL and (b) The modelled and measured frequency-meter gain.

shows large fluctuations predominantly at around 1 Hz. This corresponds to the Tip Tilt longitudinal resonance frequency which is the dominant source of cavity noise. Therefore as expected, the relative frequency measurement between the lasers, provides an indirect measurement of the cavity displacement relative to the science laser. The acquisition of the relative frequency measurement completes the dual frequency PDH scheme.

## 6.4 ALS Control Loop

To complete the ALS control system, the frequency meter output was compared with *frequency meter offset*, and the difference fed back to the Tip Tilt actuator, via a cavity controller implemented on the CDS network (see Section 4.3). This feedback scheme is shown in Figure 6.17. The frequency meter offset was for setting the heterodyne frequency when the ALS loop was closed and could also be used to tune the cavity length. The difference between the frequency meter output and the offset was sent out of the FPGA via the 1 MHz DAC and into the CDS network via an ADC. On the CDS it was sent to cavity controller which consisted of gain and filter stages. The cavity controller fed this signal to the Tip Tilt 1 position actuator (see section 6.1.2).

A block diagram showing the frequency dependent components of the completed ALS loop is shown in Figure 6.18. The loop consists of the auxiliary laser locking loop, the frequency meter, the cavity length stabilisation controller and the Tip Tilt actuator.

From Section 6.2 the auxiliary laser locking loop forces the auxiliary laser to track the cavity length with a response given by  $G_{all}(\omega)$  (Equation 6.18), which was plotted in Figure 6.11(b). From Section 6.3 the frequency meter (based on the DPLL) measures the relative frequency between the science and auxiliary laser with a response given by  $G_{fm}(\omega)$  (Equation 6.30), which was plotted in Figure 6.15(b). The Tip Tilt actuator transfer function is represented by  $A_{tt}(\omega)$  and was plotted in Figure 6.4. The cavity

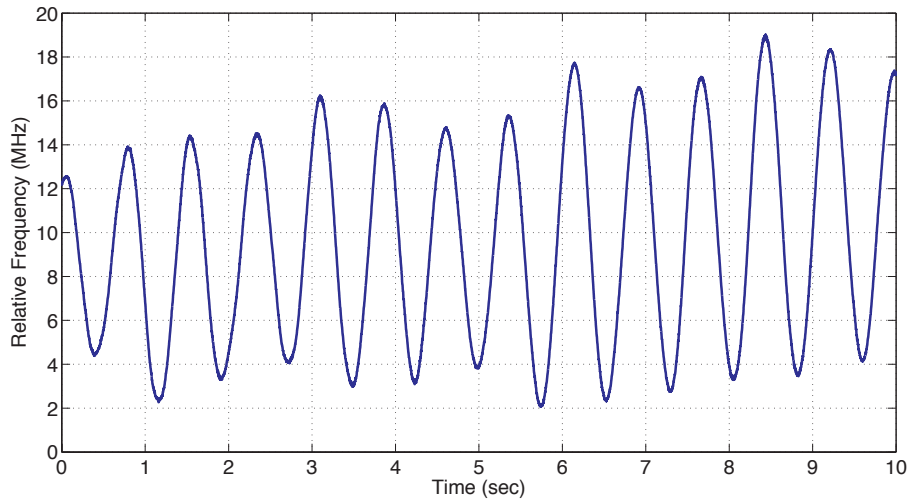


Figure 6.16: A time trace of the frequency difference between the two lasers, as measured by the DPLL.

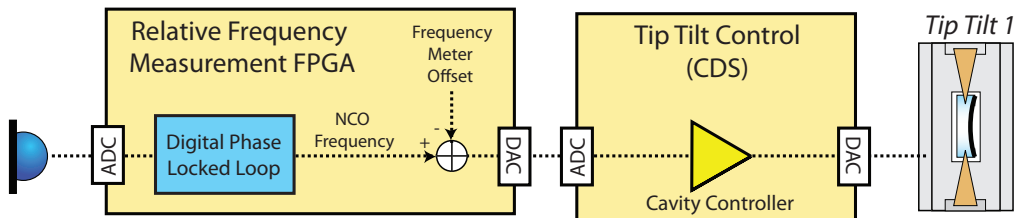


Figure 6.17: Feedback to the Tip Tilt mirror via the CDS system.

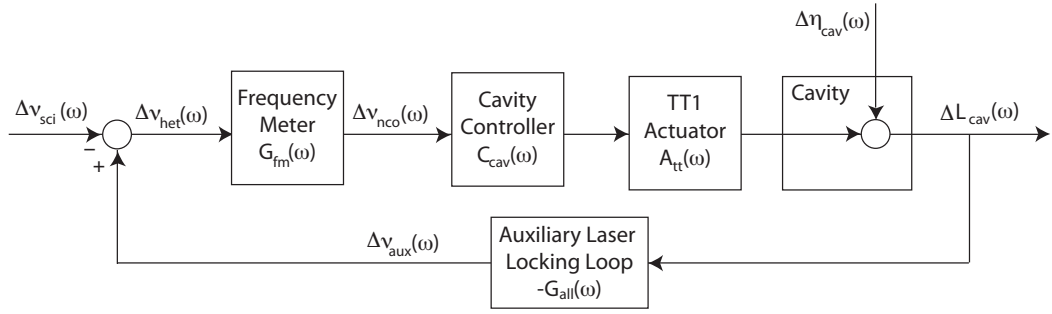


Figure 6.18: Block diagram of the ALS control loop

controller is represented by the transfer function  $C_{cav}(\omega)$  and was designed based on the known transfer functions of the other components in the loop and to ensure a stable and robust ALS control system.

$\Delta L_{cav}(\omega)$  represents the cavity length fluctuations, and are equal to the sum of the changes brought on by the actuator and the external disturbances (seismic, acoustic) represented by  $\Delta\eta_{cav}(\omega)$ . When the loop is closed the cavity length fluctuations will be related to the science laser frequency and the external disturbances via the equation:

$$\begin{aligned}\Delta L_{cav}(\omega) = & - \left( \frac{G_{fm}(\omega)C_{cav}(\omega)A_{tt}(\omega)}{1 + G_{fm}(\omega)C_{cav}(\omega)A_{tt}(\omega)G_{all}(\omega)} \right) \Delta\nu_{sci}(\omega) \\ & + \left( \frac{1}{1 + G_{fm}(\omega)C_{cav}(\omega)A_{tt}(\omega)G_{all}(\omega)} \right) \Delta\eta_{cav}(\omega)\end{aligned}\quad (6.31)$$

The open loop gain of the ALS loop is equal to the response of the frequency meter, auxiliary locking loop, Tip Tilt actuator and controller:

$$OLG_{als}(\omega) = G_{fm}(\omega)C_{cav}(\omega)A_{tt}(\omega)G_{all}(\omega) \quad (6.32)$$

The cavity length fluctuations in terms of the open loop gain of the ALS loop is therefore:

$$\Delta L_{cav}(\omega) = - \left( \frac{OLG_{als}(\omega)}{1 + OLG_{als}(\omega)} \right) \left( \frac{1}{G_{all}(\omega)} \right) \Delta\nu_{sci}(\omega) + \left( \frac{1}{1 + OLG_{als}(\omega)} \right) \Delta\eta_{cav}(\omega) \quad (6.33)$$

In the high loop gain limit ( $OLG_{als} \gg 1$ ) the cavity length fluctuations become:

$$\Delta L_{cav}(\omega) = - \left( \frac{L_{cav}}{\nu_{aux,ir}} \right) \Delta\nu_{sci}(\omega) \quad (6.34)$$

Therefore the cavity length fluctuations will be suppressed relative to the frequency of the auxiliary laser. Note that in the high loop gain limit, the auxiliary laser locking response has been reduced to  $G_{all} = \nu_{aux,ir}/L_{cav}$ .

Based on transfer functions of the other components in the ALS control loop the cavity controller was designed to ensure a stable, robust control loop to suppress the cavity length fluctuations. This controller was implemented on the CDS system and was a basic filter, that incorporated a zero at 20 Hz to change the  $f^{-2}$  response (from the Tip Tilt pendulum response) above this frequency to a  $f^{-1}$  response. Below the pendulum resonance a boost and integrator stage were employed to give the loop higher gain at low frequencies.

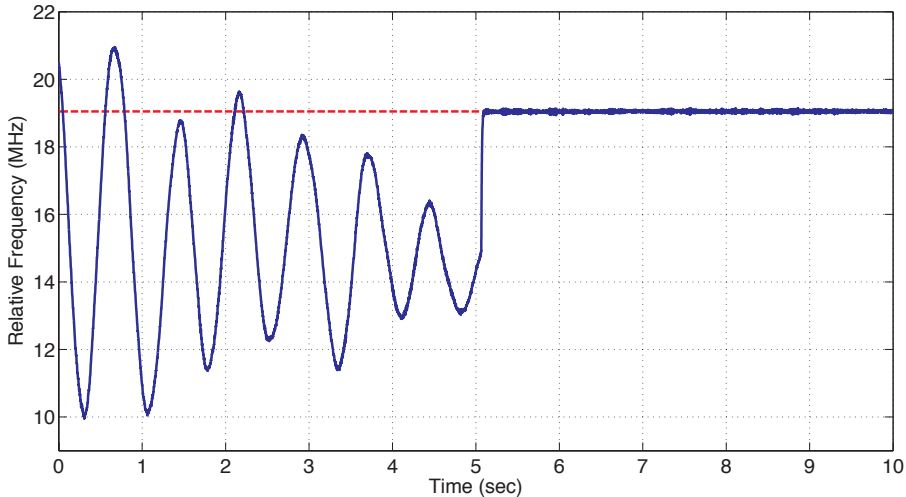


Figure 6.19: A time trace of the relative frequency between the two lasers, when the measurement is fed back to the Tip-Tilt actuators.

The bandwidth of the PDH control loop was limited by the latency of the CDS system which was measured to be about 0.3 ms. From the  $f^{-1}$  response and the CDS latency a unity gain frequency of 300 Hz was calculated to give a phase margin of about  $60^\circ$ , which would correspond to a sufficiently stable ALS control loop.

With ALS controller designed and implemented, the auxiliary laser locked to the cavity and the frequency meter reading out the relative frequency fluctuations between the two lasers, the cavity could be stabilised to the science laser. This was achieved by first tuning the cavity so as to bring the heterodyne frequency within the frequency meter offset (calibrated in Hertz) and then closing the loop to suppress the apparent cavity length fluctuations. A time series of the relative frequency during this process is shown in Figure 6.19. As can be seen, when the feedback is engaged (just after 5 seconds) there is a noticeable suppression of the relative frequency fluctuations, and the heterodyne frequency locks to the frequency meter offset (which was set to 19 MHz). This suppression of the relative frequency corresponds to a suppression of the cavity length fluctuations since the auxiliary laser was locked to the cavity and the relative frequency measurement was dominated by changes in the cavity length.

The initial calculation of the phase margin was only an approximation. Once a stable lock was achieved the loop gain was optimised to ensure a phase margin of  $60^\circ$  was achieved. A measurement of the open loop gain between 10 and 300 Hz was obtained by sending a swept sine into the control loop and measuring the negative ratio between the output signal before and after the injection point of the input signal. This open loop gain is plotted in Figure 6.20 along with a model using the components of the loop. The unity gain frequency was 128 Hz, with a phase margin of  $58^\circ$  and gain margin of 13 dB.

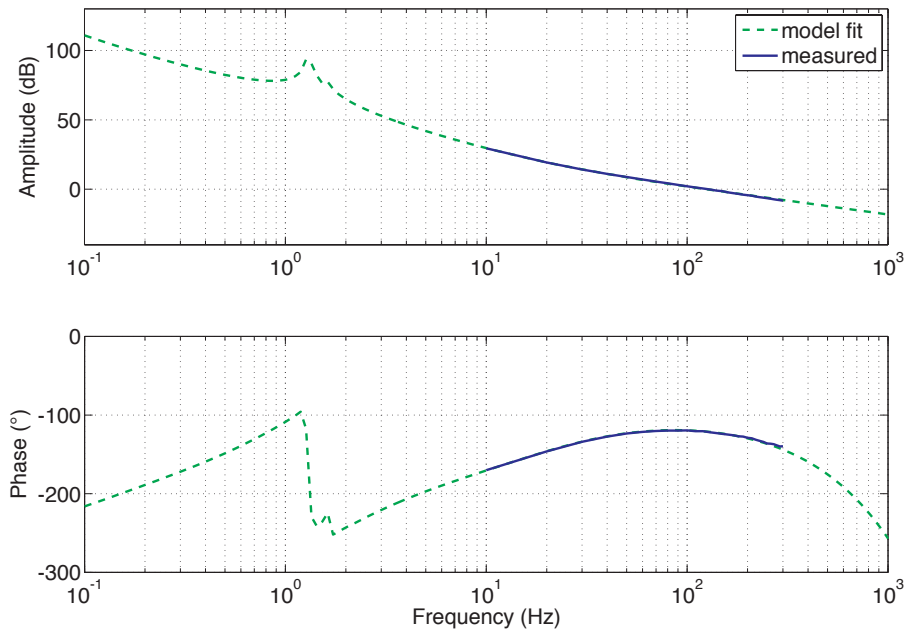


Figure 6.20: Measured and modelled ALS open loop gain

## 6.5 Tuneability of the Cavity

The first requirement of the ALS system was to gain control of the tuning of the cavity length over an FSR with respect to the science laser. To achieve this a controllable offset needed to be injected into the ALS control loop.

The obvious choice for this offset was the frequency meter offset which was already implemented to control the heterodyne frequency. Since the auxiliary laser at this point is locked to the cavity, tuning the heterodyne frequency corresponds to the tuning of the cavity length relative to the science laser. However the frequency range of this tuning is limited by the sampling of the heterodyne signal into the FPGA. From sampling theory [66] the maximum frequency that the heterodyne signal can change by without being aliased by the ADC is the Nyquist frequency. This is equal to half the sampling frequency of the ADC. The sampling rate of the ADC was 80 MHz, and so the heterodyne frequency could only be tuned over a range of 40 MHz. This approximately corresponds to only one third of the range required to tune the cavity by a full FSR.

To be able to tune the cavity over the full FSR, a method for injecting an offset into the ALS loop before the ADC, had to be devised. Since at this point in the loop the cavity length information is encoded onto the frequency of the heterodyne signal, the offset had to be injected via the frequency of another sinusoid. A signal generator (Hewlett Packard E4400B) with a frequency range of 250 kHz to 1 GHz was used to generate this sinusoid which was then mixed with the RF output from the heterodyne PD, as illustrated in Figure 6.21. Recall from Section 3.1 that a multiplication in the time domain corresponds to a convolution in the frequency domain, resulting in the heterodyne frequency being shifted both up and down by the frequency of the signal generator. A low pass filter was

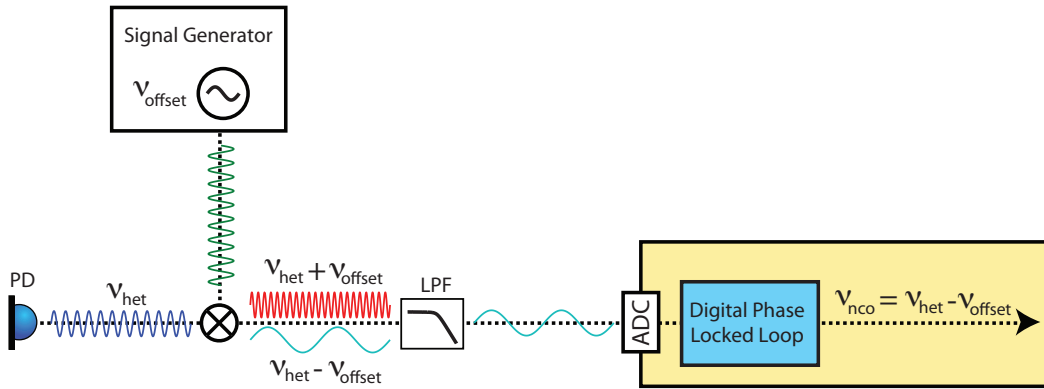


Figure 6.21: Schematic for the tuning of the relative frequency between the lasers and therefore the tuning of the cavity length.

used to eliminate the up-converted component, allowing the down-converted signal to pass to the DPPLL. The frequency of the NCO  $\nu_{nco}$  was therefore equal to the difference between the heterodyne frequency  $\nu_{het}$  and the signal generator offset frequency  $\nu_{sgo}$ :

$$\nu_{nco} = \nu_{het} - \nu_{sgo} \quad (6.35)$$

Upon feedback, this value is driven to frequency meter offset  $\nu_{fmo}$ , meaning that the heterodyne frequency equals:

$$\nu_{het} = \nu_{sgo} + \nu_{fmo} \quad (6.36)$$

Therefore the heterodyne frequency and thus the cavity could be tuned by controlling the frequency offset of the signal generator. From here on we will refer to the offset of the signal generator simply as the offset frequency.

The offset frequency was tuned over a range of 160MHz, to cover a full FSR of the cavity, and the transmitted science laser power was measured. The transmitted power of the auxiliary laser's green beam and the science laser PDH error signal were also measured. These measurements are plotted in Figure 6.22.

The top plot in Figure 6.22 shows the normalised cavity transmitted power for the science infrared laser. As can be seen, the cavity passes through two resonances as the offset is tuned, clearly demonstrating the ALS system's capacity to tune the cavity over a full FSR. The bottom trace shows the normalised cavity transmission of the auxiliary green laser and demonstrates the high stability and robustness of the auxiliary locking loop while the cavity is tuned. The middle plot shows the science laser PDH error signal. From the transmitted infra-red measurement the FSR was measured to be 115.3 MHz, in direct agreement with the design value from Table 6.1. The noise introduced to the ALS loop from the addition of the mixer was found to be negligible.

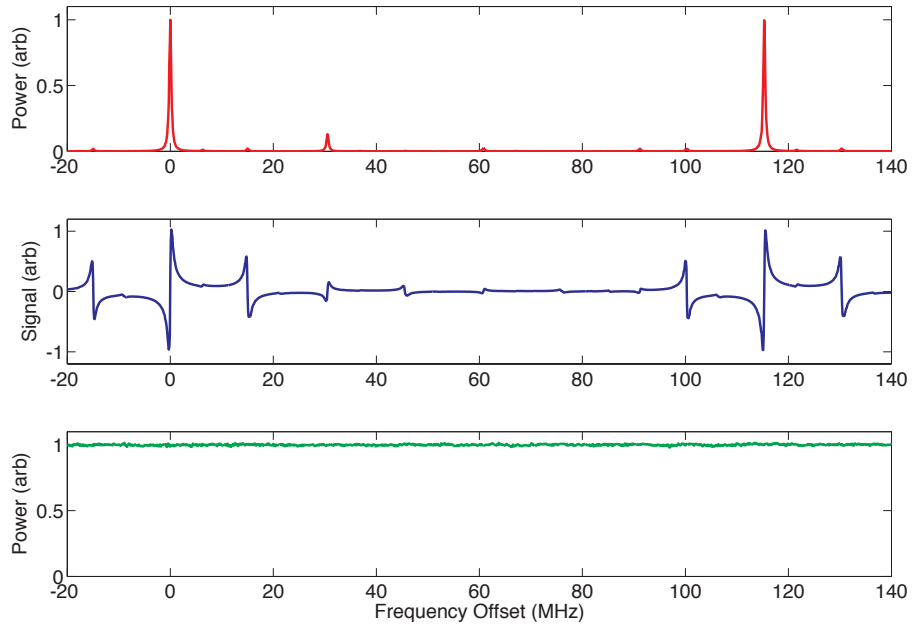


Figure 6.22: Tuning of the frequency offset over 160 MHz. Top - Normalised cavity transmission of the science infrared laser, Middle - Science PDH error signal, Bottom - Normalised cavity transmission of the auxiliary green laser.

## 6.6 Cavity Stability

The second requirement of the ALS system was to stabilise the RMS fluctuations of the arm cavity length to within one line-width relative to the science laser.

The performance of the ALS system in regard to this cavity stabilisation requirement was first tested by tuning the cavity onto resonance with the science laser and monitoring the transmitted infrared power. A 100 second time domain measurement of the normalised infrared transmission was recorded and is plotted in Figure 6.23, along with a time domain measurement of the normalised green transmission. The fluctuations of the infrared transmission from maximum power are less than 10%, indicating that the cavity length is stabilised to a level less than the line-width.

The science laser PDH readout was used as an out of loop sensor, allowing for a more quantitative measurement of the cavity stability. A 100 second trace of the science PDH readout was recorded and calibrated in terms of equivalent displacement using Equation 6.3. The in-loop ALS signal was also measured and calibrated in terms of equivalent displacement using the frequency meter gain and the FPGA to CDS conversion. The spectra of the calibrated science PDH and in-loop ALS measurements are plotted in Figure 6.24.

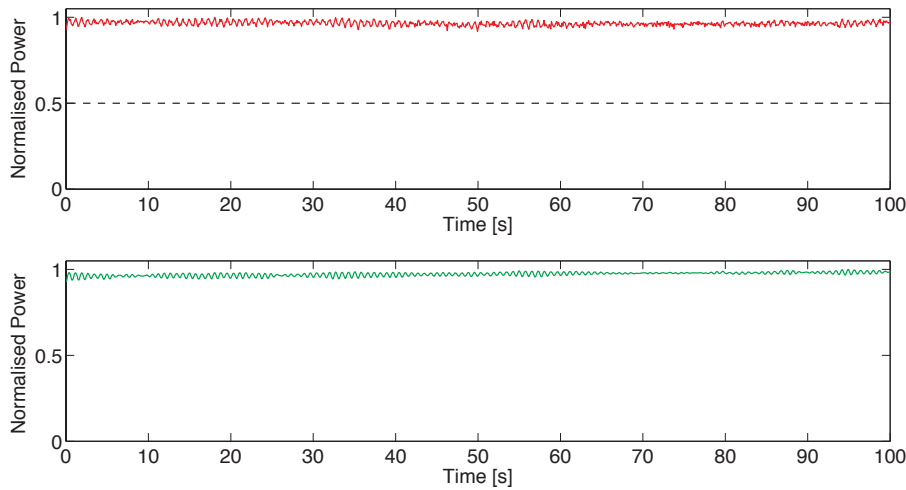


Figure 6.23: The transmitted infra-red power (top plot) with the newly optimised ALS setup and the transmitted green power (bottom plot) for comparison.

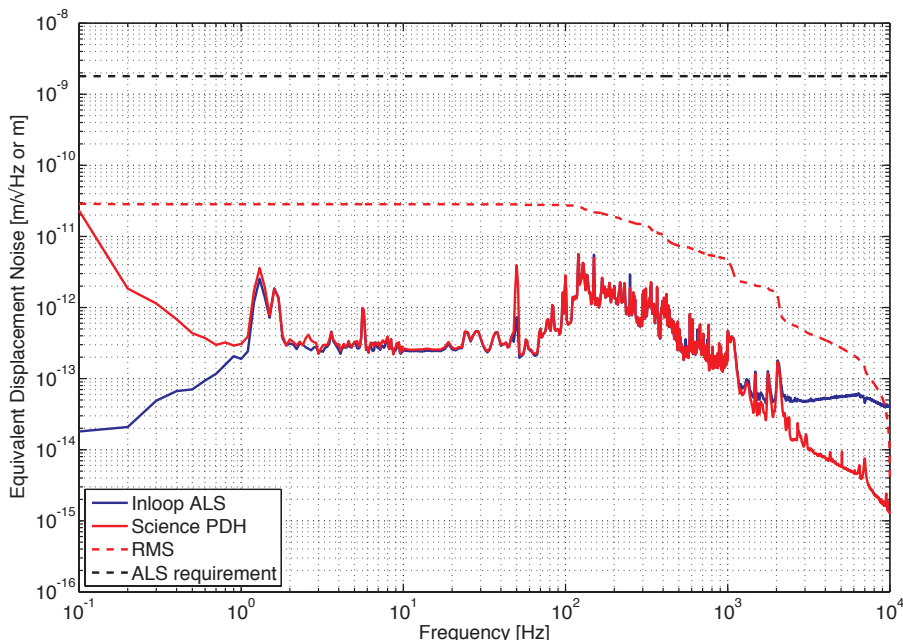


Figure 6.24: The displacement noise of the cavity measured using the science laser PDH, and the in-loop ALS. The ALS stability requirement and the integrated RMS of the science PDH measurement have also been included.

The line-width of the Tip Tilt cavity for infra-red light is:

$$\begin{aligned}\delta_{1064} &= \frac{\lambda}{2\mathcal{F}} \\ &= \frac{1064 \text{ nm}}{2 \times 296.3} \\ &\approx 1.8 \text{ nm}\end{aligned}\tag{6.37}$$

The integrated RMS fluctuations were obtained from the science PDH spectra and are also plotted in Figure 6.24 along with the ALS requirement. As can be seen the RMS motion is 30.2 pm, meeting the requirement by almost two orders of magnitude (a factor of 60).

Ideally, the science PDH and in-loop ALS spectra should be equal at all frequencies, as they are both measurements of the suppressed cavity length fluctuations. This is the case for frequencies between 1 Hz and 1 kHz.

Between 1 and 10 Hz there are a few noticeable spikes in both spectra, which are due to the modes of the cavity mirrors being excited. The Tip Tilt pendulum resonance can be seen in the spectra at 1.3 Hz. There is also a spike near 1.6 Hz which could be either the pitch or the yaw resonance or a combination of both. The spike at about 5.5 Hz is most likely the Tip Tilt vertical bounce mode.

Above 1 kHz the in-loop ALS spectra is flat, whereas the science PDH continues to decreases approximately as  $f^{-2}$ , following the Tip Tilt pendulum response. The extra noise in the in-loop ALS is due to electronic noise from the FPGA DAC. This noise is above the unity gain frequency of the ALS loop and therefore is not fed back to the cavity length, hence why it doesn't corrupt the science PDH measurement.

Below 1 Hz the science PDH spectra is noisier than the in-loop ALS spectra. It remains unclear what this low frequency noise is due to. The discrepancy could be due to the green and infrared light probing slightly different lengths. The cavity is contained in air and so air turbulence provides a mechanism for which this discrepancy in cavity lengths could come about, through refractive index changes or the different volumes occupied by the spatial modes of the two intra-cavity beams. The discrepancy could also be due to fluctuations of alignment of the beams into the cavity.

## Optimisation

In achieving the level of stability shown in Figure 6.24 the experiment had to be optimised by identifying and measuring possible noise sources and where necessary reducing them. Figure 6.25 shows a summary of the measured noise sources. The initial and optimised spectra of the in-loop ALS and science PDH has also been plotted.

The initial science PDH spectra shows a larger level of noise below 10 Hz, compared to the in-loop ALS. This noise was due to a discrepancy between the cavity length fluctuations that the green and infrared beams were seeing, which was caused by air turbulence through the intra-cavity beam. There are two mechanisms through which this could occur. The first mechanism is through the wavelength dependent refractive index of air. Green and

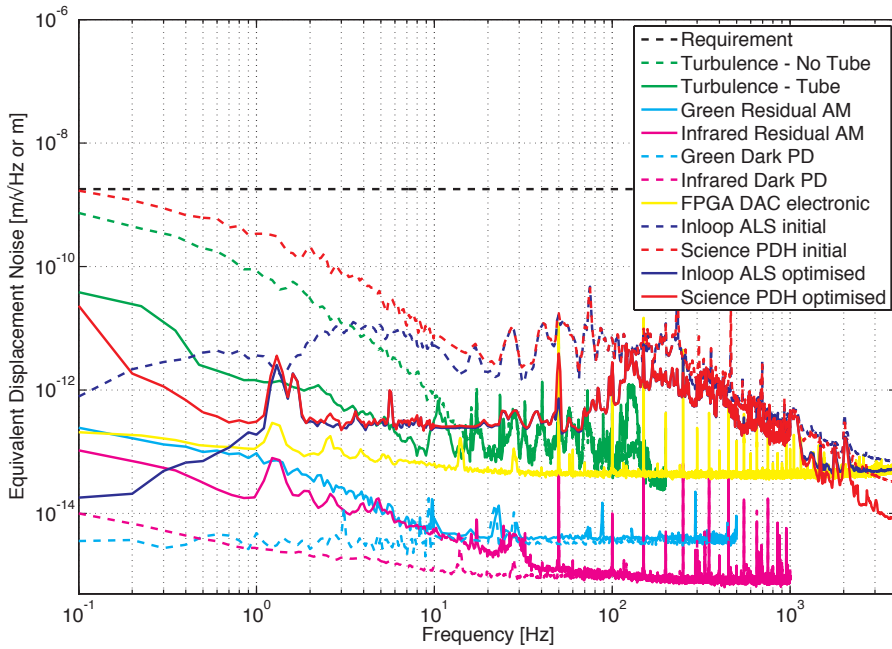


Figure 6.25: The initial stability performance, optimised performance and all measured noise sources.

infrared light experience different air refractive indices and therefore different optical path lengths. Density changes brought on by air turbulence result in changes in the refractive index. These changes result in different optical path length changes seen by the infrared and green beams. The second mechanism is through the difference in volume occupied by the green and infra-red beams in the cavity.

Air turbulence through the cavity was reduced by enclosing the beam in a perspex tube. The spectra labeled ‘turbulence’ in Figure 6.25 is for a measurement of the difference between the infrared and green measurements of the length changes. The dashed (green) line shows this measurement with no beam tube. The noise at low frequencies has the same shape and is almost at the same level as the initial science PDH spectra. The solid (green) line shows the reduction of the low frequency noise when the beam tube is included. To see how this measurement was taken and for more on air turbulence effects, see Appendix C.

The initial spectra of the in-loop ALS and science PDH measurements show bumps and spikes between 10 Hz and 100 Hz. These resonances were suspected to be due to the structural modes of the optical table and were minimised by floating the table on its gas legs.

The EOM used for phase modulation in the experiment can also impose amplitude modulation (AM) onto the light [101]. The light passing through the EOM needs to be vertically polarised. Any deviation from this results in polarisation modulation at the modulation frequency of the EOM. The polarisation beam splitter used to reflect the cavity reflected light onto the reflected PD, converts this polarisation modulation to amplitude modulation. Since this amplitude modulation occurs at the modulation frequency, it is demodulated at the mixer and registers as noise in the PDH measurement. To measure

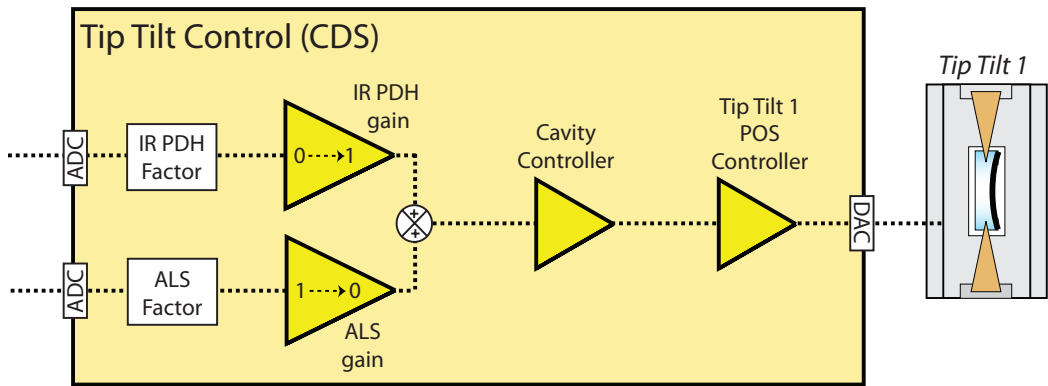


Figure 6.26: Diagram showing the basic scheme for transferring the control of the cavity from the ALS feedback to the science PDH feedback.

the level of this noise, the cavity was blocked and the calibrated error signal read out. This was done for both PDH schemes. The spectra for these measurements are plotted as ‘green residual AM’ and ‘infrared residual AM’ in Figure 6.25. The calibrated spectra for when the reflected PD was blocked has also been plotted and is labelled as ‘green dark PD’ and ‘infrared dark PD’.

Other forms of noise that have not been measured here but could have degraded the stability include alignment noise and phase noise introduced by the SHG of the auxiliary laser.

## 6.7 Control Transfer

The two requirements of the ALS system are needed to ensure smooth cavity tuning and efficient control transfer between the two sensing schemes. As such a final test of the ALS system was carried out to handover the control of the cavity from dual frequency PDH feedback to the standard science laser PDH feedback. Figure 6.26 shows the basic setup on the CDS network that was used to facilitate this control transfer.

The IR PDH and ALS factors were used to normalise the feedback signals. These factors were calculated based on the calibrations obtained for the science PDH and ALS signals, and ensured that the response to the cavity here would be equal for each signal. The normalised feedback signals were then each passed through gain stages that multiplied the signal by a number ranging from 0 to 1. After these gain stages the two signals are added together and fed back to the cavity controller.

While the cavity is under control from the ALS system, the ALS gain is 1 while the IRPDH gain is 0. To hand over the control from the ALS to the science PDH, the ALS gain is decreases linearly with time from 1 to 0, while the IRPDH gain is increased linearly from 0 to 1. A simple python script was written to handle and ensure a smooth control transfer.

Figure 6.27 shows a successful hand-over from ALS to the science PDH control, after the cavity has been tuned onto resonance. The top plot shows the normalised cavity

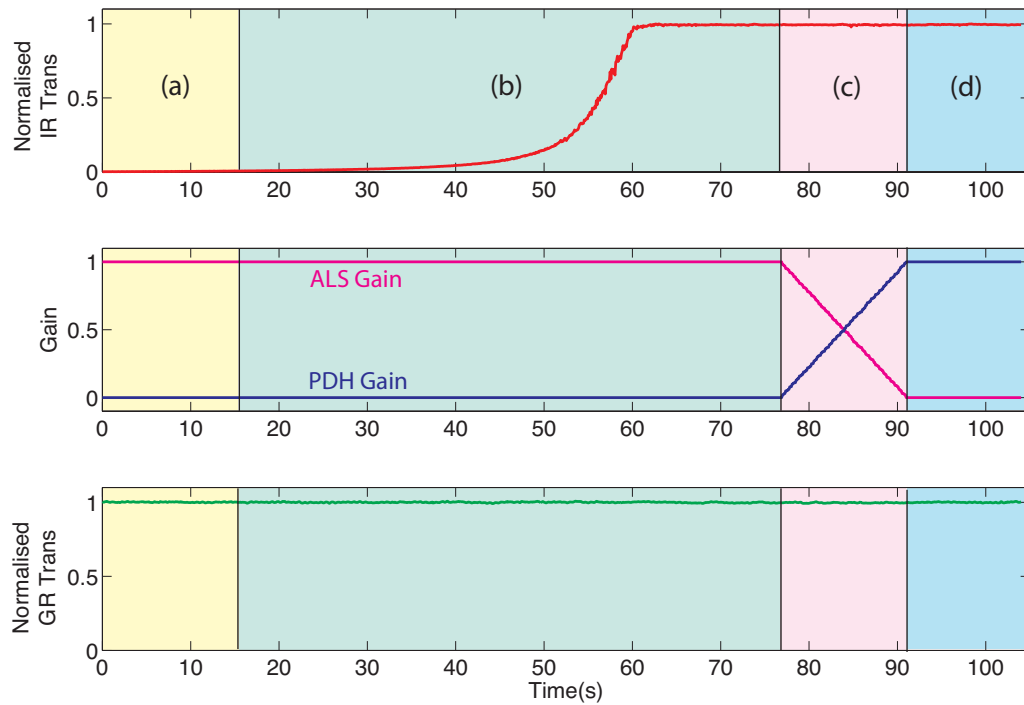


Figure 6.27: Time traces of the transmitted science laser power (top), the ALS and science PDH gains (middle), and the transmitted auxiliary green laser power, during the handoff procedure.

transmitted infra-red power to show the infrared resonance state of the cavity during the hand-over. The middle plot shows the ALS and IRPDH gains. The bottom plot shows the normalised transmitted green power to show the stability of the auxiliary locking loop during the hand-over. The traces are divided into four shaded regions, which represent the different stages of the transfer:

- (a) The cavity was initially stabilised at a point far from resonance by the ALS system.
- (b) The cavity was tuned onto resonance by adjusting the offset frequency of the down-converting signal generator. The infrared power in the cavity slowly increased with the tuning until it reached maximum, at which point the offset was no longer tuned. The ALS system maintained the cavity on resonance.
- (c) Control over the cavity length was transferred from the ALS system to the science PDH. This was done by running the Python script that increased the PDH gain while decreasing the ALS gain.
- (d) The cavity length was stabilised and under the control of the science PDH signal alone.

## 6.8 Discussion

The results presented in this chapter have shown the successful tuning of a cavity over an FSR by the ALS, and the suppression of the residual motion of the cavity to less than a cavity line-width. Despite meeting requirements, these results need to be considered in context. Any extrapolation of the work presented in this chapter to a kilometre scale interferometer should take into account the differences in environment and optical configuration.

The LIGO arm cavities are enclosed in beam tubes which have been evacuated down to a pressure less than  $1 \times 10^{-9}$  torr [102] and as such the ALS won't be limited by residual gas effects such as air turbulence and temperature induced density drifts.

The FSR for the LIGO arm cavities is 37.5 kHz, a factor of 4000 smaller than the FSR of our Tip Tilt cavity, due to the length being a factor of 4000 larger. The limit on the range of tune-ability that we initially encountered should not be an issue for the Advanced LIGO ALS. However this means that the ALS will be more sensitive to laser frequency noise from the science laser. Fortunately the science laser in LIGO is pre-stabilised to a reference cavity, unlike our free running science laser.

Differences in test mass actuation and site noise also need to be considered, however recent simulation work [103] predicts that, taking these differences in to account, the ALS stability requirement can still be met.

## 6.9 Summary

In this chapter the viability of the ALS system based on the dual frequency PDH readout was demonstrated using a single cavity made of Tip Tilt mirrors. The setup of the ALS experiment was divided into four steps - setting up the cavity, locking the auxiliary laser to the cavity, measuring the relative frequency between the auxiliary and science lasers and the feedback of the relative frequency measurement to the cavity. The implementation of each step was described in detail.

Using the implemented ALS system, the cavity's residual motion was stabilised down to an RMS value of 30.2 pm which was less than one cavity linewidth as per the ALS stability requirement. The ALS system was also used to tune the cavity over a full FSR (115 MHz) as per the ALS tuning requirement. The smooth control handover between the ALS and science laser PDH systems was also demonstrated.



## Chapter 7

# Stable Transfer of an Optical Frequency Through A Fibre

In Section 5.4.3 it was briefly discussed that to obtain a heterodyne measurement of the relative frequency, light from the science laser needed to be sent over 4km to the auxiliary laser.

One option for achieving this is to send the light through an optical fibre. The field of fibre-optic dissemination of optical frequencies has grown over the last few decades. This growth is due mostly to the invention of ultra-precise laser frequency stabilisation techniques, such as the optical frequency comb [104, 105], and the fact that these techniques are complex, expensive and not very portable, necessitating methods for distributing them over long distances. Fibre optic based transmission is generally the preferred technique due to its relatively easy installation, flexibility and the fact that it can yield high fractional frequency stabilities [106, 107].

In this chapter we discuss the technical difficulties that arise with sending an optical frequency over a kilometre scale optical fibre. We then present a novel technique based on phase-locked loops, for the stable transfer of an optical frequency reference over a fibre. At the end of the chapter, the results of an experiment testing this technique are presented. The technique and results have been published in [108].

### 7.1 Heterodyning via a 4km Fibre

Consider the setup in Figure 7.1, which shows the relative frequency measurement scheme that was introduced in Section 6.3. Here the science laser beam is sent through an optical fibre, to transfer it over a large distance.

There are two main issues with trying to obtain a heterodyne measurement of the relative frequency between two lasers after one has been sent over a large distance through an optical fibre.

1. The first issue is that the optical path length through the fibre can vary substantially, through temperature and mechanical fluctuations that couple into the refractive

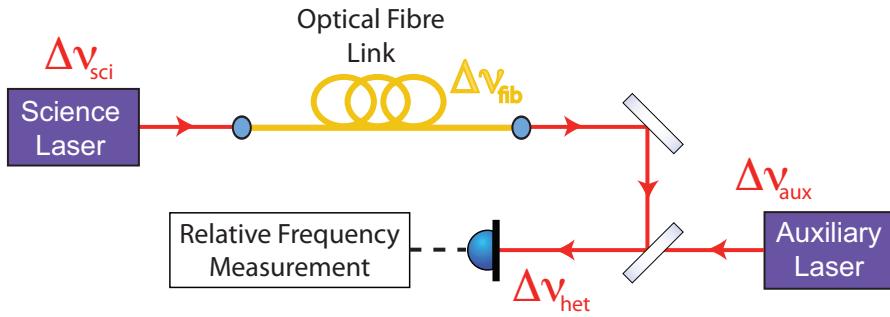


Figure 7.1: Relative frequency measurement scheme when the science laser is sent through an optical fibre.

index and physical length of the fibre.

2. The second issue is that the transferred laser beam takes some finite time to travel over this distance.

The variations in the heterodyne frequency (derived from Equation 6.19) are given by:

$$\Delta\nu_{het}(\omega) = \Delta\nu_{sci}(\omega)e^{-i\omega\tau} + \Delta\nu_{fib}(\omega) - \Delta\nu_{aux}(\omega) \quad (7.1)$$

where  $\Delta\nu_{sci}$  and  $\Delta\nu_{aux}$  are the absolute frequency fluctuations of the science and auxiliary lasers,  $\tau$  is the delay time through the fibre, and  $\Delta\nu_{fib}$  is the equivalent frequency noise induced by the optical path length fluctuations through the fibre. The fibre induced frequency noise is related to the optical path length fluctuations  $\Delta L_{op}$  via the equation:

$$\Delta\nu_{fib}(\omega) = i\omega \frac{2\pi}{\lambda} \Delta L_{op}(\omega) \quad (7.2)$$

The delay of the frequency through the fibre is represented in the frequency domain by multiplication with the exponential term  $e^{-i\omega\tau}$ . Effectively the noise in the fibre and the delay through the fibre corrupt the heterodyne measurement, from which we only desire to measure the frequency difference between the two lasers.

In the Arm Length Stabilisation (ALS) scheme the auxiliary laser is locked to the science laser indirectly via the cavity. To simplify the analysis we ignore the cavity and assume the heterodyne measurement is fed directly to the auxiliary laser. This scheme, which is common in the field of fibre optic dissemination, is shown in Figure 7.2. A phase-locked loop (PLL) like the one from Section 6.3 is used to read out the heterodyne frequency. We refer to this PLL as the ‘End Station PLL’. Another PLL is used to measure the true frequency fluctuations between the auxiliary laser and the science laser (assume that the lasers and ends of the fibre are co-located). We refer to this PLL as the ‘Truth PLL’. In the high loop gain limit, feedback to the auxiliary laser drives the frequency fluctuations of the heterodyne measurement from Equation 7.1 to zero, and therefore the auxiliary laser fluctuations equal the delayed science laser fluctuations plus the fibre fluctuations:

$$\Delta\nu_{aux}(\omega) = \Delta\nu_{sci}(\omega)e^{-i\omega\tau} + \Delta\nu_{fib}(\omega) \quad (7.3)$$

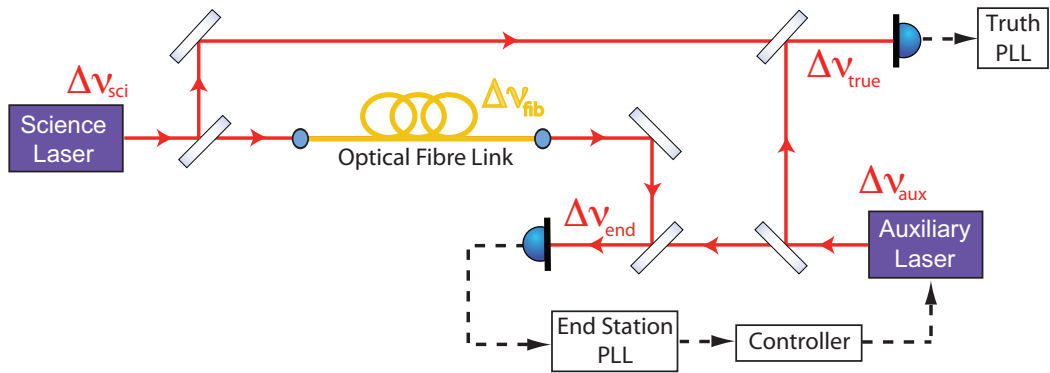


Figure 7.2: Feedback of the fibre transfer corrupted heterodyne to the auxiliary laser frequency.

The measurement of the frequency difference between the two lasers obtained from the Truth PLL is given by:

$$\begin{aligned}\Delta\nu_{true} &= \Delta\nu_{sci}(\omega) - \Delta\nu_{aux}(\omega) \\ &= (1 - e^{-i\omega\tau}) \Delta\nu_{sci}(\omega) - \Delta\nu_{fib}(\omega)\end{aligned}\quad (7.4)$$

Ideally we want this true measurement to be zero, as this would indicate that the auxiliary laser frequency tracks the science laser. As evident from the above equation, this is not the case. Equation 7.4 represents the contributions of the fibre induced noise and the science laser's absolute frequency fluctuations to the relative frequency noise between the science and auxiliary lasers.

The transfer function from these contributions to the truth measurement were modelled in Matlab [87] for a fibre length of  $L = 4.6$  km and a refractive index of  $n = 1.5$ , which gave a delay through the fibre of  $\tau = 23\mu s$ . These values were chosen to be consistent with the experiment discussed at the end of the chapter (see Section 7.3). These transfer functions are plotted in Figure 7.3.

The response of the truth measurement to the fibre noise contribution (Figure 7.3 (a)) simply has unity gain. For fourier frequencies much less than the inverse of the fibre delay ( $f \ll 1/\tau$ ), the response of the truth measurement to the science laser's absolute frequency fluctuations increases linearly with  $f$ . Effectively this response is a high pass filter.

## 7.2 A Novel Technique for Fibre Frequency Noise Suppression

Current techniques for transferring frequency standards over fibre links [109, 110, 106] all implement a common scheme, first suggested by Ma et al [111], where an acousto-optic modulator (AOM) is used to counter-act the fibre induced phase fluctuations (see Appendix D for an analysis of this technique). Here we present a novel AOM independent

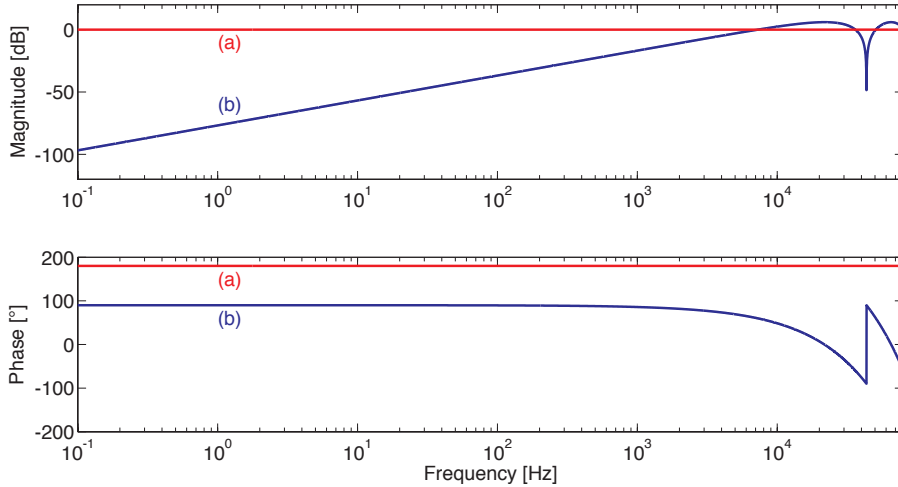


Figure 7.3: Transfer functions from (a) the fibre induced frequency fluctuations to the truth measurement and (b) the science laser frequency to the truth measurement.

technique that is also capable of cancelling relative frequency noise introduced by fibre fluctuations and the delay through the fibre.

If one could delay the auxiliary laser by the same delay that the science laser experiences before combining the two beams on a photo-detector, the delay induced noise could be nullified. The obvious way to do this would be to send the auxiliary laser light through a fibre of the same length as the fibre used to transfer the science laser light to the end station. The problem here is the new fibre would introduce frequency noise to the auxiliary laser beam.

However, if the auxiliary laser was sent down the same optical fibre used to transfer the science laser light but in the opposite direction, and combined with the prompt science laser beam in the corner station, then this heterodyne signal would have the same fibre induced fluctuations as the end station signal. With the correct linear combination of the two signals, the fibre noise could be cancelled out. A similar scheme has been used in the LISA (Laser Interferometric Space Antennae) backlink experiment [112]. This technique assumes that the fibre noise is the same in both directions and varying on a time-scale less than the delay through the fibre.

Consider the diagram in Figure 7.4, which shows this technique. Light from the science laser is sent down the optical fibre to be combined with promptly emitted light from the auxiliary laser on the end station photo-detector. The resulting heterodyne signal is read out by the End Station PLL. The auxiliary laser light is also sent down the optical fibre in the opposite direction to the corner station, where it is combined on a photo-detector with promptly emitted light from the science laser. The Corner Station PLL reads out the frequency fluctuations of this heterodyne signal.

The frequency fluctuations measured by the End Station PLL,  $\Delta\nu_{end}$ , and Corner

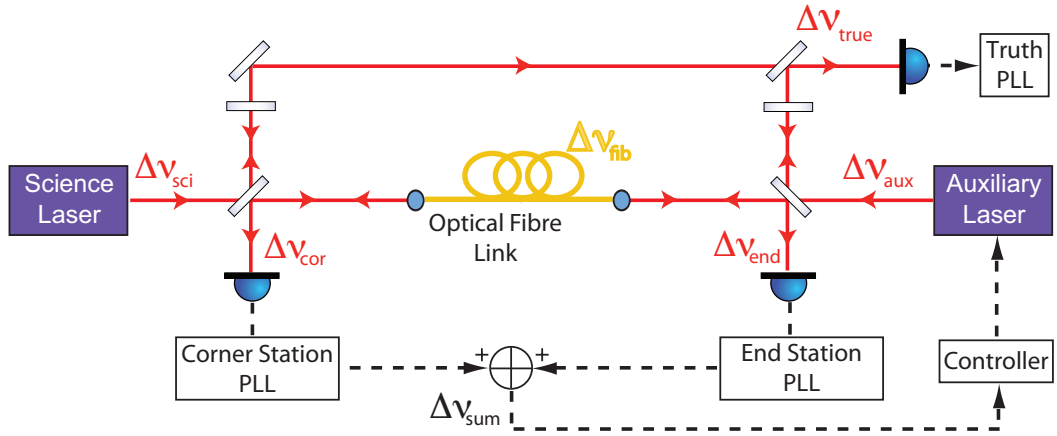


Figure 7.4: Basic layout of the technique where the sum of the phasemeter readouts are fed back to the auxiliary laser to cancel out fibre induced phase noise.

Station PLL,  $\Delta\nu_{cor}$ , are given by:

$$\Delta\nu_{cor}(\omega) = \Delta\nu_{sci}(\omega) - \{\Delta\nu_{aux}(\omega)e^{-i\omega\tau} + \Delta\nu_{fib}(\omega)\} \quad (7.5)$$

$$\Delta\nu_{end}(\omega) = \{\Delta\nu_{sci}(\omega)e^{-i\omega\tau} + \Delta\nu_{fib}(\omega)\} - \Delta\nu_{aux}(\omega) \quad (7.6)$$

The fibre noise is anti-correlated in the two measurements and therefore a fibre noise free measurement can be obtained by adding the two signals together. The corner and end station measurements occur 4km apart and therefore one of the signals would need to be sent electronically to the other station, introducing another delay. To simplify analysis, imagine that both signals are delayed by the same amount of time before being added. This delay will be represented by  $\epsilon$ , and should be comparable to  $\tau$ . The sum of the corner and end station heterodyne frequencies is given by:

$$\Delta\nu_{sum}(\omega) = \Delta\nu_{cor}(\omega)e^{-i\omega\epsilon} + \Delta\nu_{end}(\omega)e^{-i\omega\epsilon} \quad (7.7)$$

Substituting Equation 7.5 and Equation 7.6 into Equation 7.7 yields:

$$\Delta\nu_{sum}(\omega) = \{\Delta\nu_{sci}(\omega) - \Delta\nu_{aux}(\omega)\} \{1 + e^{-i\omega\tau}\} e^{-i\omega\epsilon} \quad (7.8)$$

This signal gets driven to zero when fed back to the auxiliary laser and therefore the auxiliary laser frequency will track the science laser frequency.

$$\Delta\nu_{aux}(\omega) = \Delta\nu_{sci}(\omega) \quad (7.9)$$

Note that this is only true for frequencies lower than the bandwidth of the control loop, where the gain is much greater than unity. The  $\{1 + e^{-i\omega\tau}\}e^{-i\omega\epsilon}$  term in Equation 7.8 limits the bandwidth. The bode diagram of this term is plotted in Figure 7.5, using a value of  $\epsilon = 26\mu\text{s}$  which was chosen to be slightly longer than the fibre delay time  $\tau$ . The unity gain frequency of the control loop is limited to the inverse of the fibre and electronic delays, i.e.  $f_{ugf} \ll \tau^{-1}, \epsilon^{-1}$ .

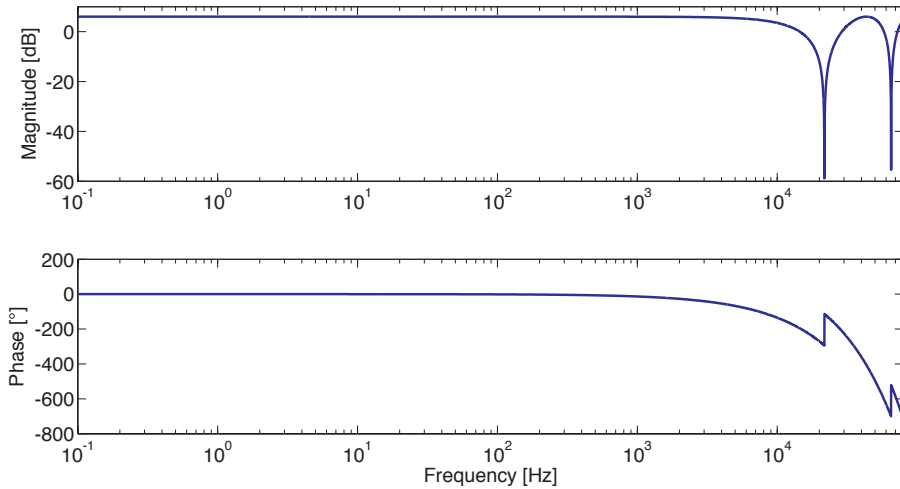


Figure 7.5: Transfer function from the relative frequency between the auxiliary and science laser to the summed heterodyne signal.

## 7.3 Experiment

An experiment was set up to test the technique from the previous section. A diagram of the layout can be seen in Figure 7.6. Much of the setup from the experiment in Chapter 6 was utilised. The Prometheus Nd:YAG laser again played the role of the auxiliary laser, and the Lightwave Nd:YAG laser played the role of the science laser.

The optical fibre link used in the experiment was 4.6 km long and single mode for 1064 nm. The fibre link had the potential to introduce other non-linear forms of noise to our experiment, such as stimulated brillouin scattering and Rayleigh back scattering. We minimised these effects by reducing the optical power of the light going into the fibre down to 50  $\mu$ W. The fibre was also non-polarisation maintaining and as such the polarisation of the light passing through the fibre would drift, causing the amplitude of the heterodyne signal to also drift. However the digital phase locked loops (DPLLs) had an amplitude to phase coupling of about 0.06  $\mu$ radians/% and therefore the deviation of the amplitude due to polarisation drift was not a factor.

A flipper mirror was placed just before each input coupler of the fibre, giving the option of bypassing the fibre so that an estimate of the noise floor could be obtained.

Our corner and end station photo-detectors were of the same design as the in-house built photo-detector [100] from Section 6.3. The RF outputs were each sent through an anti-aliasing filter, to a 40 MHz ADC. The digital outputs of the ADCs were then sent to the DPLLs, which were again implemented on an FPGA. The End Station DPLL measured the frequency of the heterodyne signal on the End Station photodetector and contained information shown in Equation 7.6. At the same time the Corner Station DPLL measurement (represented in Equation 7.5) was sent to the End Station DPLL via a digital link. For this bench-top demonstration, both DPLLs were co-located.

The two DPLL output signals were summed together so that the fibre-induced fluctuations would be cancelled as shown in Equation 7.8. This  $\Delta\nu_{sum}$  signal was then sent

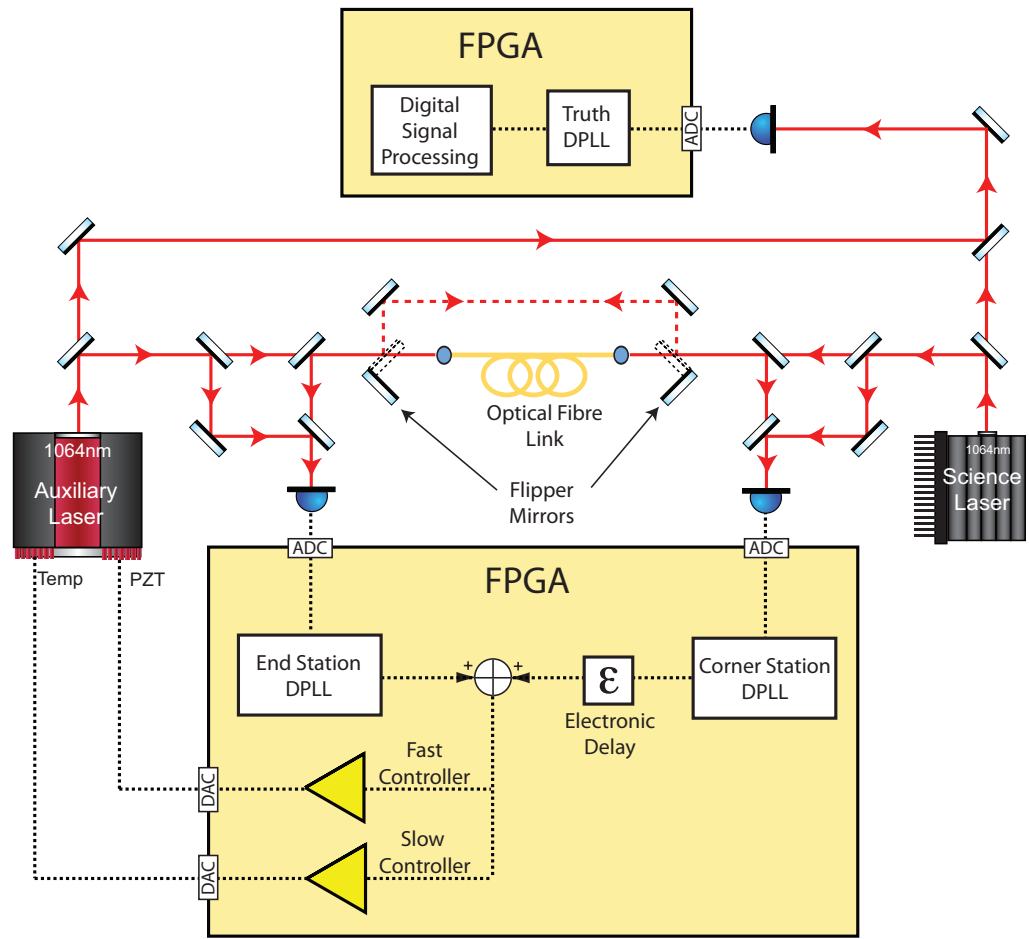


Figure 7.6: Bench-top experiment configuration to test out the technique.

through the digital controller and fed back to the auxiliary laser by the digital-to-analog converter (DAC) outputs. For fast frequency control one DAC output was fed back to a piezo-electric transducer (PZT) that exerted pressure on the laser crystal. A second DAC output was fed back to the temperature of the laser crystal to provide larger range feedback.

Light from each laser was tapped off before entering the fibre and combined on another photodetector. The RF signal from this photodetector was sent through another anti-aliasing filter and digitised by an ADC, before being provided to a third DPLL which measured the true instantaneous frequency fluctuations between the two lasers.

## 7.4 Results

To characterise our fibre noise cancellation technique, we first used the flipper mirrors in front of each fibre coupler to direct the beams around the fibre link. The auxiliary laser was then phase-locked to the science laser. A time domain measurement of the relative frequency noise between the two lasers was recorded from the truth DPLL with a 100 kHz sampling rate. With such a high sampling rate, only ten seconds of data was recorded. An amplitude spectral density of this time series was calculated and is plotted in Figure 7.7 (a). This plot provides the measurement noise floor for our experiment and was due to the relative motion of the sensing optics at both ends.

The fibre was then included in the optical path, and the auxiliary laser locked up with end station signal feedback (Equation 7.6) only. Another ten second trace of the truth DPLL was recorded, and the corresponding spectrum has been plotted in Figure 7.7 (b). This plot provides a measurement of the frequency noise that results from the fibre noise and/or the delay through the fibre, represented by the transfer function in Equation 7.4.

Finally the corner station signal was added to the end station signal, and the resulting signal fed back to suppress any fibre induced noise. Another ten second trace was taken, and the spectrum is plotted in Figure 7.7 (c). Note that the gain settings were kept the same for all three cases.

In the noise floor measurement in plot (a) of Figure 7.7, the spectra is flat from a few hertz to a few tens of hertz. Above this, to about a kilohertz the spectra rolls up as  $f^2$ . The noise below a few tens of hertz is due to the relative motion of the sensing optics at both ends. The noise above this is gain limited, in that the free-running relative frequency noise between the two lasers rolls down as  $f^{-1}$ , and the digital controller response has a  $f^{-3}$  slope in this frequency range.

In plot (b) of Figure 7.7 the relative frequency is considerably noisier than the measurement noise floor, more than or equal to two orders of magnitude below 100 Hz. As the only difference between these two measurements is the inclusion of the 4.6 km fibre, it can be deduced that sending the light through the fibre is what results in the extra noise. At the end of Section 7.1 we showed that the response of the truth measurement to the science laser frequency noise would be proportional to  $f$  (for  $f \ll 1/\tau$ ). The science laser was free-running in our experiment, and therefore the frequency noise rolls off as  $1/f$ , and

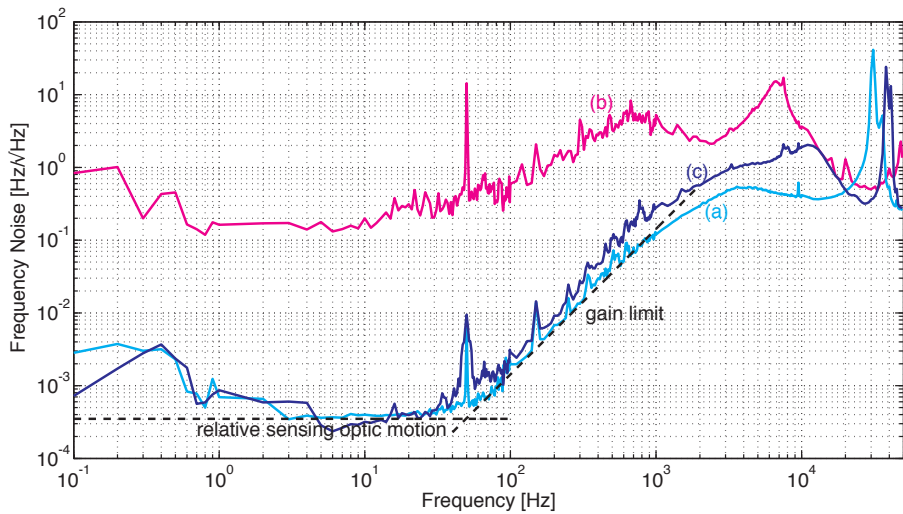


Figure 7.7: The true measurement of the relative frequency noise between the two lasers when the auxiliary laser is phase locked to the science laser for the case where: (a) the fibre is bypassed, (b) the fibre is included and the remote signal used for feedback and (c) the fibre is included and the equal delay sum of the local and remote signals fed back to the laser

is approximately 10 to 100  $\text{Hz}/\sqrt{\text{Hz}}$  at 100 Hz [113]. Therefore, we expect the science laser frequency noise contribution here to be approximately 0.1 to 1  $\text{Hz}/\sqrt{\text{Hz}}$ . As can be seen, this is the level of the noise measured.

Plot (c) of Figure 7.7, shows that the addition of the corner station signal to the feedback, results in two orders of magnitude suppression (below 100 Hz) of the relative frequency noise in plot (b), down to the measurement noise floor in plot (a). This noise is less than  $3 \text{ mHz}/\sqrt{\text{Hz}}$  below 100 Hz. The fractional frequency stability of this noise is simply the noise over the optical frequency ( $3 \times 10^{14} \text{ Hz}$ ). The fractional frequency stability reaches a level of approximately  $2 \times 10^{-18}/\sqrt{\text{Hz}}$  between 1 and 30 Hz.

## 7.5 Discussion

Recall that a bandwidth of 120 Hz was sufficient for our ALS control loop, and it should also be sufficient for the Advanced LIGO ALS loop, as the most of the residual displacement noise occurs well below this frequency (see Figure 2.15). This means that we need to only consider the noise induced onto the heterodyne measurement below this frequency. The instability for the case of no fibre correction (Figure 7.7(b)) is less than  $1 \text{ Hz}/\sqrt{\text{Hz}}$  below 100 Hz (excluding the 50 Hz AC mains spike). The instability imposed onto the LIGO arm cavity by an ALS system using this 4.6 km fibre to transfer the science laser

frequency reference would be:

$$\begin{aligned}\Delta L_{cav} &= \left(\frac{L}{\nu}\right) \Delta\nu_{true} \\ &= \left(\frac{4000 \text{ m}}{3 \times 10^{14} \text{ Hz}}\right) \times 1 \text{ Hz}/\sqrt{\text{Hz}} \\ &\approx 1.3 \times 10^{-11} \text{ m}/\sqrt{\text{Hz}}\end{aligned}\tag{7.10}$$

This is about two orders of magnitude less than the Advanced LIGO ALS requirement, and therefore appears not to be a concern. The 4.6 km fibre used in the experiment, was spooled and contained in standard laboratory conditions. At one of the LIGO sites a fibre connecting the corner station to the end station would be rolled out underground along the length of the arm cavity. Therefore we would expect that coupling of temperature and seismic fluctuations into this underground fibre would be greater than that of the fibre in our experiment.

Below 100 Hz our technique suppresses the induced frequency noise below  $3 \text{ mHz}/\sqrt{\text{Hz}}$ . In theory this technique should be able to suppress fibre induced fluctuations for a rolled out fibre down to the same level of stability. Assuming this is the case, the instability imposed onto the LIGO arm cavity by an ALS system using this technique would be:

$$\Delta L_{cav} = 4 \times 10^{-14} \text{ m}/\sqrt{\text{Hz}}\tag{7.11}$$

This may not be the case if the fibre induced noise is direction dependent, which is a phenomenon referred to as fibre non-reciprocity. It is difficult to predict how our technique would perform on a rolled out underground fibre. As such, implementation over an underground fibre network is the subject of future work.

## 7.6 Summary

This chapter discussed the stability of the transfer of an optical frequency reference through an optical fibre. This work was motivated by the need to send light from a laser over 4 km as part of ALS system. The two main sources of instability were identified - the first was from variations in the optical path length of the fibre due to mechanical and temperature disturbances, and the second was due to the finite travel time through the fibre. The main goal of the chapter was to introduce a new stabilisation technique based on PLLs. The details of an experiment to test this technique over a 4.6 km optical fibre were described. The main result of this experiment was the two orders of magnitude suppression of the fibre induced frequency noise down to the noise floor, at a level of  $3 \text{ mHz}/\sqrt{\text{Hz}}$ . A fractional frequency stability of  $2 \times 10^{-18}/\sqrt{\text{Hz}}$  was also reached between 1 and 30 Hz.

# Chapter 8

## Conclusion and Future Work

The work presented in this thesis was motivated by the Advanced LIGO upgrade. The majority of the work was specifically motivated by the Arm Length Stabilisation system which will be responsible for the initial stabilisation and tuning of the arm cavities during the lock acquisition of the interferometer.

The major outcomes of the thesis can be summarised as:

- The characterisation of a prototype Tip Tilt mirror which involved measuring the various eigenmodes of the mirror and its suspension structure. The frequencies of five of the six degrees of freedom were all measured to be less than 10 Hz and the corresponding quality factors were all measured to be less than 100 as per the Advanced LIGO requirement. The frequencies of the main mechanical modes of the Tip Tilt structure were also measured to be more than 150 Hz as per the requirement.
- The demonstration of the viability of the Arm Length Stabilisation (ALS) system based on dual frequency PDH readout using a Tip Tilt cavity. The ALS system was used to stabilise the cavity's residual motion to less than the cavity line-width and tune the cavity over an FSR as per the ALS requirements. The hand-over of the control of the cavity from the ALS to the science laser PDH was also demonstrated.
- The development and verification of a new technique, based on phase locked loops, for the stable transfer of an optical frequency reference over a 4.6 km fibre. The technique was used to suppress fibre induced noise imposed onto the relative frequency between two phase locked lasers by two orders of magnitude.

### 8.1 Double Pendulum Suspension for the Tip Tilt Mirrors

There are plans to improve the design of the Tip Tilt mirror by suspending the mirror via a double pendulum, like the one used to suspend the OMC [114]. This double pendulum suspension would give the mirror extra isolation above the two pendulum resonances, with a response that rolls off as  $f^{-4}$ . By suspending the mirror from the penultimate stage

with two wires on each side, the control of the mirror could be handled via actuation of the penultimate stage.

## 8.2 Digitally Enhanced Heterodyne Interferometry for Lock Acquisition

Digitally Enhanced Heterodyne Interferometry (DEHI) is a reasonably new and interesting technique that could also be used to readout the cavity length for an Arm Length Stabilisation system. DEHI is largely untested with the exception of an experiment where the displacement noise of a 3.75m cavity, locked to a laser using PDH technique, was readout to a level of  $5 \text{ pm}/\sqrt{\text{Hz}}$ .

At the time of the writing of this thesis, DEHI readout has not been used in feedback to control the length of a cavity. However a DEHI readout scheme has been implemented for the Tip Tilt cavity<sup>1</sup>[115] and there are plans to stabilise the cavity in a feedback control system.

Due to its multiplexing capabilities [116], the DEHI technique has the extra benefit that it could be used for readout of all five degrees of freedom of the dual recycled Fabry-Perot michelson and not just the arm cavities. Although the sensitivity would be much less than a system using the PDH technique, and therefore not viable for continued global control of the interferometer, DEHI would be ideal for lock acquisition.

## 8.3 Further Testing of the PLL Fibre Stabilisation Technique

The new technique presented in Chapter 7 was tested on a 4.6 km long spooled fibre contained in pristine lab conditions. The stability of the transfer of the free-running laser through this fibre was found to be limited by the transfer time and not the optical path length fluctuations in the fibre. It was only possible to put an upper limit on the fibre fluctuations.

For further verification of the technique presented in Chapter 7, it should be tested on a system limited by optical path length fluctuations. One simple way to do this is to use fibre stretchers on the spooled fibre to vary the optical path length at a known frequency, and use the technique to try to suppress it below the noise floor.

Another way is to try the technique on a fibre rolled out underground over some large distance. This is much more complicated as underground kilometre scale optical fibres are not that accessible. As part of an effort by a group of Australian research groups looking to create a National Timing and Frequency Network, our lab was connected to the Intra-government COmmunications Network (ICON)[117]. ICON is an underground system of dark optical fibres spread out over hundreds of kilometres around the Australian Capital Territory. Initially ICON will be used to test out techniques for disseminating a

---

<sup>1</sup>For an undergraduate honours project carried out by Silvie Ngo under the supervision of John Miller.

stable RF or microwave frequency standard over 100 km scales. However there are plans to transfer a stable optical frequency reference over this network which could be done using the technique presented here.



## Appendix A

# Feedback Control Systems

This appendix gives a very brief description of feedback control systems. Here we will describe some of the rules and notation, however the theory behind these rules will not be explained. Instead the reader is referred to [55], which provides a very good introduction to feedback control systems, sufficient enough to understand the control systems used in this thesis.

A feedback control system (FCS) is used to force a system to track a reference to a specified degree of accuracy. Figure A.1 shows a block diagram representing the main components and signals of a feedback control system.

This system that we wish to control is referred to as the *plant*. Ideally the output of the plant would be constant, however due to external factors the plant varies with time, i.e. it is free-running. One can think of the output of this plant as the sum of a steady (constant) output and a time-dependent disturbance. In practice the steady state cannot be measured independently of the disturbance, the distinction here is simply a mathematical convenience.

The output of the plant is measured by the *sensor* which depends on the output in some known way. Generally this dependence is approximately linear. The output of the sensor is then compared to a reference level to generate an *error signal*. The error signal is sent to the *controller* where it is filtered and amplified, before being fed to the *actuator* which modifies the plant and its output.

Each component of the FCS can be represented by a frequency dependent transfer function. Note that in this thesis we mostly consider control systems that have reached some steady state, and therefore Fourier transforms will suffice (no need for Laplacian transforms).

The output of the plant is equal to the disturbance plus the error signal that has passed through the controller and actuator, which is represented by:

$$o(\omega) = \eta(\omega) + A(\omega)C(\omega)\varepsilon(\omega) \quad (\text{A.1})$$

where  $\eta(\omega)$  is the frequency dependent disturbance,  $A(\omega)$  is the frequency dependent transfer function of the actuator,  $C(\omega)$  is the frequency dependent transfer function of the controller and  $\varepsilon(\omega)$  is the error signal. This error signal is the difference between the

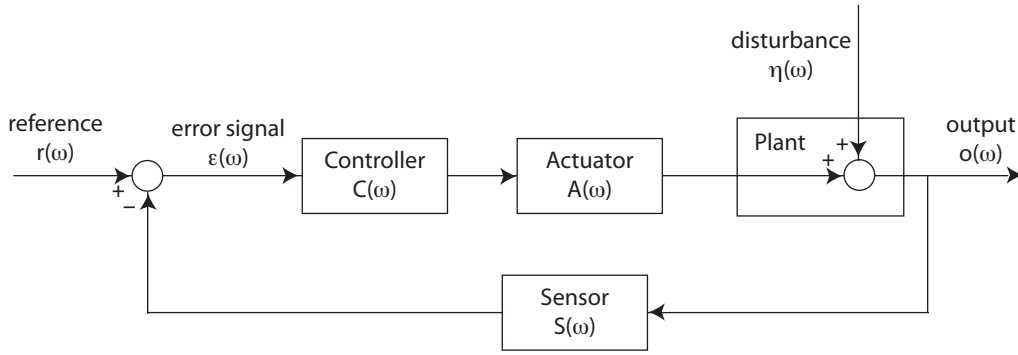


Figure A.1: A schematic of a feedback control system and all of its components.  $C(\omega)$ ,  $A(\omega)$ , and  $S(\omega)$  represent the frequency dependent transfer functions of the controller, actuator and sensor.  $r(\omega)$ ,  $\varepsilon(\omega)$  and  $o(\omega)$  represent the reference, error and output signals.

reference and the sensor of the plant output, which is given by:

$$\varepsilon(\omega) = r(\omega) - S(\omega)o(\omega) \quad (\text{A.2})$$

where  $r(\omega)$  is the reference and  $S(\omega)$  is the sensor transfer function. Substituting Equation A.2 into Equation A.1 gives a self consistent equation for the output of the plant:

$$o(\omega) = \eta(\omega) + A(\omega)C(\omega) [r(\omega) - S(\omega)o(\omega)e^{-i\omega\tau}] \quad (\text{A.3})$$

The  $e^{-i\omega\tau}$  term has been included to account for the finite delay time ( $\tau$ ) around the loop. The above self consistent equation can be solved to give the output in terms of the disturbance and the reference:

$$o(\omega) = \frac{1}{1 + A(\omega)C(\omega)S(\omega)e^{-i\omega\tau}}\eta(\omega) + \frac{A(\omega)C(\omega)}{1 + A(\omega)C(\omega)S(\omega)e^{-i\omega\tau}}r(\omega) \quad (\text{A.4})$$

The *open loop gain* is defined as the product of the transfer functions of the loop components, it is given by:

$$OLG(\omega) = A(\omega)C(\omega)S(\omega)e^{-i\omega\tau} \quad (\text{A.5})$$

Equation A.4 can be represented in terms of the open loop gain:

$$o(\omega) = \frac{1}{1 + OLG(\omega)}\eta(\omega) + \frac{OLG(\omega)}{1 + OLG(\omega)} \frac{r(\omega)}{S(\omega)e^{-i\omega\tau}} \quad (\text{A.6})$$

When the open loop gain is high ( $OLG(\omega) \gg 1$ ) the response of the output to the disturbance becomes very small ( $o(\omega)/\eta(\omega) \approx 1/OLG(\omega)$ ) and response of the output to the reference approximates to ( $o(\omega)/r(\omega) \approx 1/(S(\omega)e^{-i\omega\tau})$ ). Therefore the feedback control system forces the output of the plant to track the reference while suppressing the disturbance.

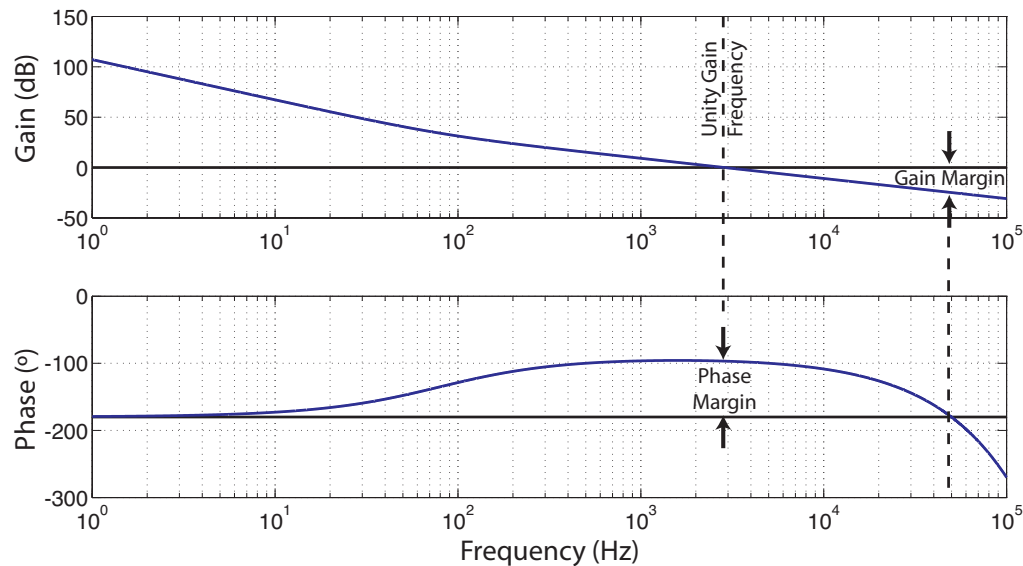


Figure A.2: A Bode plot of the open loop gain. The unity gain frequency, phase margin and gain margin are all shown.

### Loop Stability

From Equation A.5, one obvious area where the FCS can become unstable is for when the complex open loop gain is near -1 ( $OLG \approx -1$ ). For such an open loop gain the response of the output of the plant from Equation A.6 to the reference and disturbance becomes infinite. That is the FCS amplifies these terms. In practice the FCS will usually become unstable before this point is reached, as the actuator or sensor will saturate due to their finite range.

The rule for designing a stable FCS is referred to as the *Nyquist stability criterion* which states that the FCS is stable if the plot of the OLG on the complex plane has no clockwise encirclements of the (-1,0) point. Even if this condition is met, transients in the system can push the system to instability if the Nyquist plot comes too close to the (-1,0) point. Effectively the wider the area surrounding the (-1,0) region, the more robust the system will be.

This leads to the definition of the gain and phase margins which are shown in the Bode plot in Figure A.2. Gain margin and phase margin are a measure of how much area is around the Nyquist plot that includes the (-1,0) region. Hence larger gain and phase margins correspond to a more robust a system.



## Appendix B

# Tip Tilt to OMC Dither Locking

To measure and suppress the misalignments into the cavity, alignment error signals need to be derived. The technique used to do this in Advanced LIGO is Dither Locking.

Dither Locking is similar to PDH in that the degree of freedom being measured is modulated at some high frequency, which effectively upconverts the baseband noise to this frequency. And the error signal is derived by demodulating at this frequency. For dither locking the two Tip Tilt mirrors are dithered in Pitch and Yaw, at different modulation frequencies. This modulation is transferred to the angular and lateral misalignment in the cavity, and is therefore registered on the transmitted PD, see Equation 4.1. The PD output can then be demodulated at the dither frequency to obtain a readout of a linear combination of the lateral and angular misalignment.

To see how this works consider the schematic in Figure B.1 showing the alignment of the IFO beam into the OMC via the Tip Tilt mirrors (Note: the OMC has a bow tie configuration, however for simplicity we'll treat it as a linear cavity). For simplicity we'll only consider misalignments in the plane of the page, meaning that the Tip Tilts are dithered in yaw. Let the dither signals be given by:

$$\beta_n = \beta_{n0} \sin(\omega_{mn} t) \quad (\text{B.1})$$

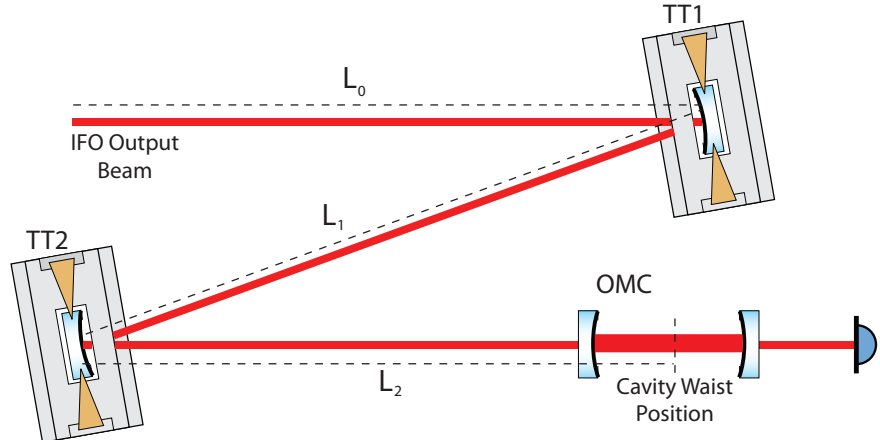


Figure B.1: Steering of the IFO beam into the OMC by the Tip Tilts.

where  $n = 1$  for Tip Tilt 1 and  $n = 2$  for Tip Tilt 2,  $\beta_{n0}$  is the amplitude of the dither signal, and  $\omega_{mn} = 2\pi f_{mn}$  is the angular modulation frequency. The lateral misalignment is given by:

$$x = x_\eta + 2(L_1 + L_2)\beta_{10} \sin(\omega_{m1}t) + 2L_2\beta_{20} \sin(\omega_{m2}t) \quad (\text{B.2})$$

where  $x_\eta$  represents the baseband noise in the lateral displacement, which includes the contributions from the interferometer output beam jitter, and the seismic noise coupling in through the Tip Tilts. The lengths  $L_1$  and  $L_2$  are defined in Figure 4.2. The angular cavity misalignment is given by:

$$\theta = \theta_\eta + 2\beta_{10} \sin(\omega_{m1}t) + 2\beta_{20} \sin(\omega_{m2}t) \quad (\text{B.3})$$

where  $\theta_\eta$  represents the baseband noise in the angular misalignment, again due to the interferometer beam jitter and seismic noise. From Equation 4.1 the transmitted power depends on the squares of the lateral and angular misalignments. This gives DC or baseband terms,  $2\omega_{m1,2}$  terms,  $\omega_{m1}\omega_{m2}$  and  $\omega_{m1,2}$  terms. The only terms of interest however are the  $\omega_{m1,2}$  terms as these contain information about the baseband noise. They can be isolated using a bandpass filter.

$$x^2(\omega_{m1,2}) = x_\eta (4(L_1 + L_2)\beta_{10} \sin(\omega_{m1}t) + 4L_2\beta_{20} \sin(\omega_{m2}t)) \quad (\text{B.4})$$

$$\theta^2(\omega_{m1,2}) = \theta_\eta (4\beta_{10} \sin(\omega_{m1}t) + 4\beta_{20} \sin(\omega_{m2}t)) \quad (\text{B.5})$$

The the transmitted power component at  $\omega_{m1}$  is:

$$P_t(\omega_{m1}) = 8P_0\beta_{10} \left( \frac{L_1 + L_2}{\omega_0^2} x_\eta + \frac{1}{\theta_0^2} \theta_\eta \right) \sin(\omega_{m1}t) \quad (\text{B.6})$$

The power component at  $\omega_{m2}$  is:

$$P_t(\omega_{m2}) = 8P_0\beta_{20} \left( \frac{L_2}{\omega_0^2} x_\eta + \frac{1}{\theta_0^2} \theta_\eta \right) \sin(\omega_{m2}t) \quad (\text{B.7})$$

These signals can be demodulated to obtain error signals that are linear combinations of the lateral and angular misalignment fluctuations. Provided the lengths, cavity waist size and divergence angle are known, a sensing matrix can be calculated and the readout of the lateral and angular misalignments can be obtained.

## Appendix C

# Air Turbulence Effects

Air turbulence was found to be a significant source of noise in our ALS experiment using the dual frequency PDH readout. Initially the intra-cavity beam was not enclosed inside a beam tube. Pressure changes brought on by anthropogenic sources, such as people moving around in the lab and talking, as well as the air conditioner, resulted in the fluctuations in the density of the air inside the cavity. These density fluctuations couple into the optical path length via the refractive index of air.

From Ciddor et. al [118] the refractivity of dry air is given by:

$$10^8(n_\lambda - 1) = \frac{\rho_a}{\rho_{axs}} A_\lambda (1 + 5.34 \times 10^{-7} (x_c - 450)) \quad (\text{C.1})$$

where  $\rho_a$  is the density of the air,  $\rho_{axs}$  is a value for the density of dry air at 15°C, 101.325 kPa and  $x_c$  is the fractional content of CO<sub>2</sub> in the air.  $\lambda$  is the optical wavelength. The constant  $A_\lambda$  is given by:

$$A_\lambda = \left[ \frac{a_1}{a_0 - (1/\lambda)^2} + \frac{a_3}{a_2 - (1/\lambda)^2} \right] \quad (\text{C.2})$$

where the constants  $a_0 = 238.0185 \mu\text{m}^{-2}$ ,  $a_1 = 5792105 \mu\text{m}^{-2}$ ,  $a_2 = 57.362 \mu\text{m}^{-2}$  and  $a_3 = 167917 \mu\text{m}^{-2}$  are from Ciddor et. al [118].

A change in the refractivity of dry air as a function of the change in density is given by:

$$\Delta n_\lambda = \frac{1 + 5.34 \times 10^{-6}(x_c - 450)}{\rho_{axs} 10^8} A_\lambda \Delta \rho_a \quad (\text{C.3})$$

Note that these refractive index variations are also wavelength dependent. The green and infrared beams will experience different refractivity fluctuations, which means that they will also experience different optical path length fluctuations. The optical path length variations for a beam with wavelength  $\lambda$  are given by:

$$\Delta L_\lambda = n_\lambda \Delta L + L \Delta n_\lambda \quad (\text{C.4})$$

where  $n_\lambda$  is the refractive index of the air for the given wavelength and  $L$  is the true length of the cavity. The discrepancy between the green and infra-red measurements is therefore given by:

$$\Delta L_{1064} - \Delta L_{532} = (n_{1064} - n_{532}) \Delta L + L(\Delta n_{1064} - \Delta n_{532}) \quad (\text{C.5})$$

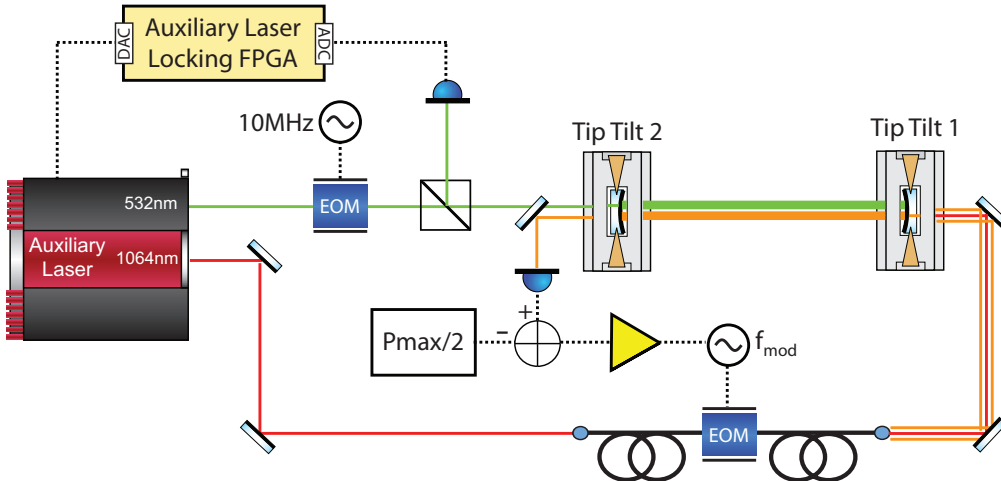


Figure C.1: The experimental setup to look at dispersive effects within the cavity.

The fluctuations of  $\Delta L$  are small ( $\sim 10^{-9}$  m) since the cavity is locked to the more stable science laser. The difference between the refractivities ( $n_\lambda - 1$ ) for green and infra-red light is around the order of  $10^{-6}$  [119], and therefore the contribution from the first term in Equation C.5 is negligible ( $\sim 10^{-15}$  m). Variations in the refractive index of air have been shown to be of the order of a few parts in  $10^9$  [120] and for a 1.3 m cavity the displacement equivalent noise resulting from such refractive index changes would have been significant ( $10^{-9}$  m).

Figure C.1 shows the setup for measuring the difference between the green and infrared. The Tip Tilt mirrors were clamped so that the green light from the auxiliary laser was locked to the cavity using the auxiliary locking loop. The infrared beam out of the auxiliary laser was sent through a broadband phase modulator (Photline NIR-MPX-LN-10 EOM), which imposed sidebands onto the light, which was then injected into the cavity. The broadband modulator was driven by a signal generator (Agilent N5181A) with a frequency range between 100 kHz and 3 GHz. The frequency of the signal generator was tuned to steer the sideband onto resonance. A feedback control loop was used to hold the sideband halfway up the fringe. This was done by feeding back the transmitted infra-red power to the sideband frequency with an offset equal to half the maximum power.

The loop controller was a low-pass filter and a proportional-integrator stage that gave a simple  $1/f$  response. The bandwidth of the loop was  $\sim 120$  Hz. In the high gain limit, the feedback correction signal to the auxiliary laser frequency when calibrated for displacement, would provide a measurement of the green optical path length fluctuations inside the cavity seen by the green laser, i.e.  $\Delta L_{532}$ . Also in this limit, the feedback correction signal to the infra-red sideband frequency when calibrated for displacement, would provide a measurement of the difference between the green and infrared optical path lengths, i.e.  $(\Delta L_{1064} - \Delta L_{532})$ .

Both feedback correction signals were recorded and calibrated for displacement. The spectra of these two signals are plotted in the top plot of Figure C.2. The ratio between

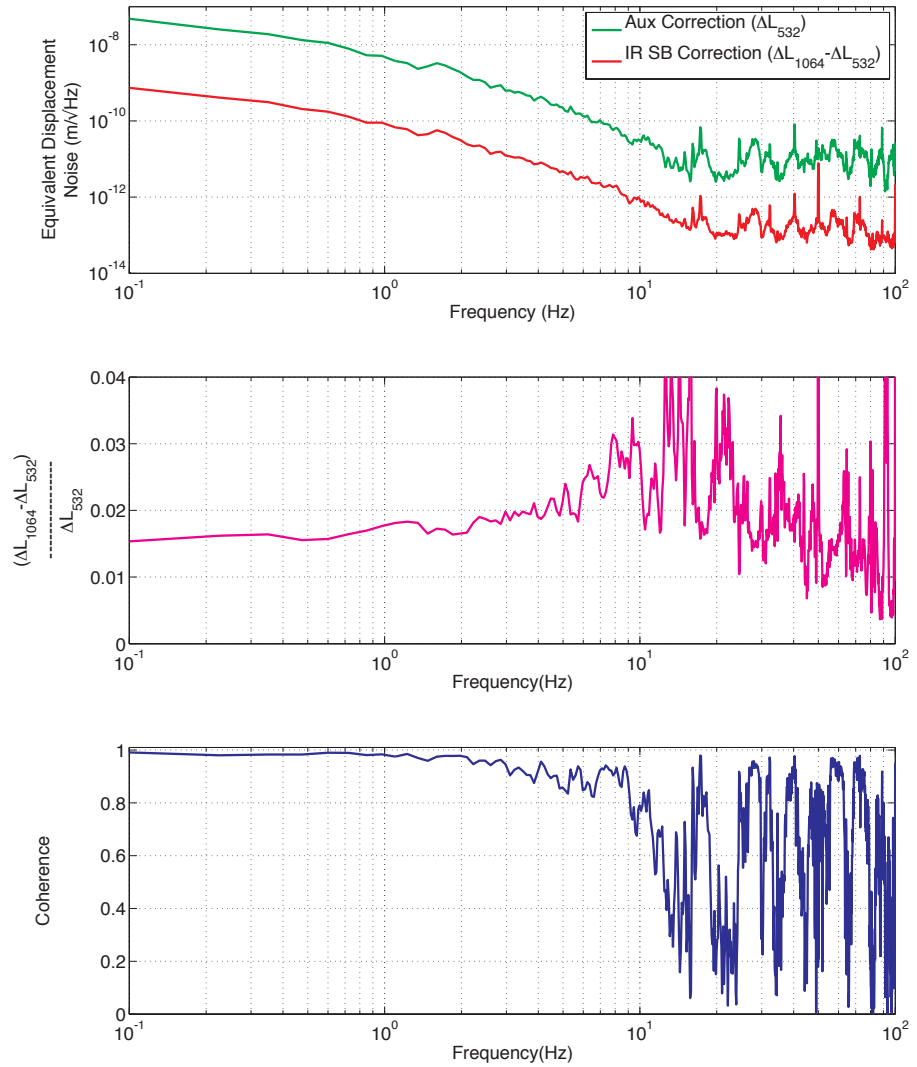


Figure C.2: Top: Spectra of the equivalent displacement noise for the auxiliary correction measurement and the infrared sideband measurement. Middle: The ratio between the two measurements. Bottom: The coherence between the two measurements.

the these two spectra was calculated and is plotted in the middle plot of FFigure C.2 and the coherence between the two spectra has also been plotted in the bottom plot.

The coherence between the two signals is approximately 1 below 1 Hz. The ratio between the two signals provides a measure of the fractional difference between infrared and green optical path lengths. At 0.1 Hz this is:

$$\left( \frac{\Delta L_{1064} - \Delta L_{532}}{\Delta L_{532}} \right)_{measured} = 0.0154 \quad (C.6)$$

This fractional difference can also be calculated using Equation C.5 (ignoring the  $\Delta L$

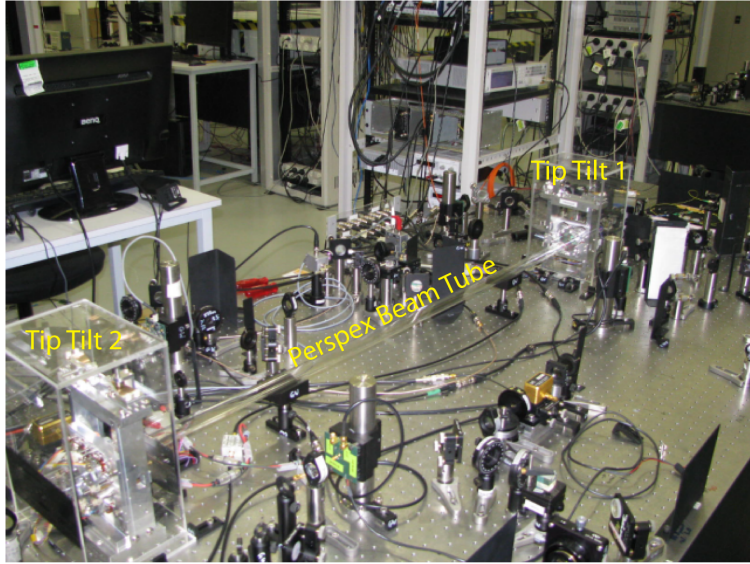


Figure C.3: The Tip Tilt cavity with the perspex beam tube enclosing the intra-cavity beams.

term, which we showed to be negligible), Equation C.3 and Equation C.2:

$$\begin{aligned}
 \left( \frac{\Delta L_{1064} - \Delta L_{532}}{\Delta L_{532}} \right)_{model} &= \left( \frac{\Delta n_{1064} - \Delta n_{532}}{\Delta n_{532}} \right)_{model} \\
 &= \frac{A_{1064}}{A_{532}} - 1 \\
 &= 0.0152
 \end{aligned} \tag{C.7}$$

The agreement between this value and the measured value in Equation C.6, indicates that the fluctuations are due to changes in the refractivity, most likely brought on by air turbulence. The induced difference between the infrared and green optical path length fluctuations inside the cavity (as indicated by the  $(\Delta L_{1064} - \Delta L_{532})$  spectra in Figure C.2) are at a significant level, where they will add noise to the cavity in the ALS system.

The air turbulence through the intra-cavity beam was reduced by enclosing the beam in a perspex tube (shown in Figure C.3). The measurements of the feedback correction signals were re-taken and are plotted against the open air results in Figure C.4. As can be seen, the inclusion of the beam tube results in an order of magnitude reduction of this noise.

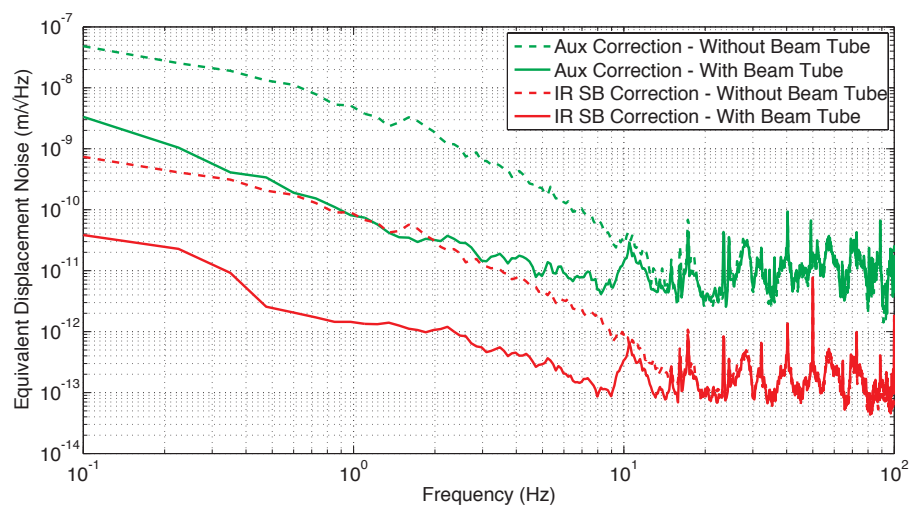


Figure C.4: The auxiliary correction measurement and the infrared sideband measurements with and without the perspex beam tube.



## Appendix D

# Common Fibre Suppression Technique

Here we explore one of the AOM based techniques [106] by applying it to our example from Section 7.1. The scheme for the technique is shown in Figure D.1.

The science laser light is first passed through an AOM, before being sent through the fibre. At the opposite end, the fibre transmitted light encounters a partial reflector. The reflected light passes back through the fibre and AOM where it is combined on a photodetector with some of the promptly emitted science laser light. A sine wave from a signal generator is used to drive the AOM. The AOM shifts the frequency of the light passing through by the frequency of the sine wave driving it.

A heterodyne measurement is produced at the photo-detector between the promptly emitted science laser beam and the frequency shifted science laser beam that has passed back and forth through the fibre and AOM. The frequency fluctuations of this heterodyne signal are measured with another PLL. This phase locked loop will be referred to as the corner station PLL. The frequency fluctuations of this corner station heterodyne signal are given by the frequency difference between the promptly emitted science laser beam and the delayed science laser beam that has completed a roundtrip through the AOM and

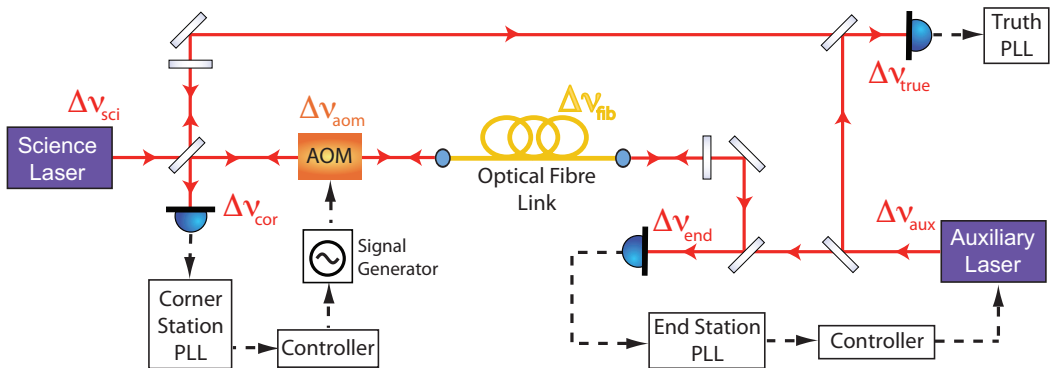


Figure D.1: The basic schematic for the AOM fibre noise suppression technique.

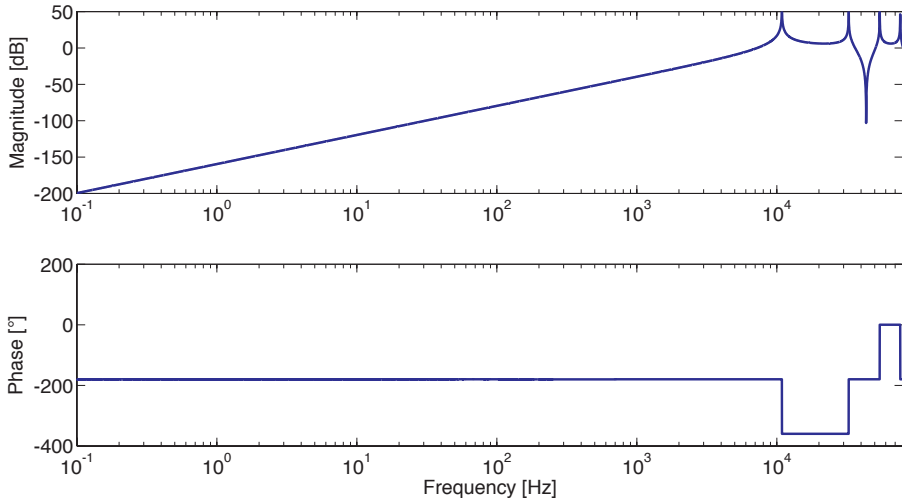


Figure D.2: Transfer functions from the equivalent fibre frequency fluctuations and the absolute science laser frequency fluctuations to the truth measurement, using the AOM technique.

fibre:

$$\begin{aligned}\Delta\nu_{cor}(\omega) &= [\Delta\nu_{sci}(\omega) + \Delta\nu_{aom}(\omega)] e^{-i2\omega\tau} + 2\Delta\nu_{fib}(\omega) + \Delta\nu_{aom}(\omega) - \Delta\nu_{sci}(\omega) \\ &= -\Delta\nu_{sci}(\omega) \{1 - e^{-i2\omega\tau}\} + \Delta\nu_{aom}(\omega) \{1 + e^{-i2\omega\tau}\} + 2\Delta\nu_{fib}(\omega)\end{aligned}\quad (\text{D.1})$$

This measurement is fed back to the AOM in a control loop, which drives the measurement to zero (for high open loop gain). The frequency fluctuations that the AOM imposes on the light are therefore given by:

$$\Delta\nu_{aom}(\omega) = \Delta\nu_{sci}(\omega) \left\{ \frac{1 - e^{-i2\omega\tau}}{1 + e^{-i2\omega\tau}} \right\} - \Delta\nu_{fib}(\omega) \left\{ \frac{2}{1 + e^{-i2\omega\tau}} \right\} \quad (\text{D.2})$$

The light that exits the fibre at the other end is the delayed AOM corrected science laser light with fibre induced fluctuations. The frequency of the end heterodyne measurement is equal to the difference between this light and the auxiliary laser light and is therefore given by:

$$\Delta\nu_{end}(\omega) = [\Delta\nu_{sci}(\omega) + \Delta\nu_{aom}(\omega)] e^{-i\omega\tau} + \Delta\nu_{fib}(\omega) - \Delta\nu_{aux}(\omega) \quad (\text{D.3})$$

Substitution of the AOM imposed frequency fluctuations from Equation D.2 into Equation D.3 yields:

$$\Delta\nu_{end}(\omega) = \Delta\nu_{sci}(\omega) \left\{ \frac{2e^{-i\omega\tau}}{1 + e^{-i2\omega\tau}} \right\} - \Delta\nu_{fib}(\omega) \left\{ \frac{(1 - e^{-i\omega\tau})^2}{1 + e^{-i2\omega\tau}} \right\} - \Delta\nu_{aux}(\omega) \quad (\text{D.4})$$

This heterodyne measurement is fed back to the frequency of the auxiliary laser, which drives it to zero, and the auxiliary laser frequency is therefore given by:

$$\Delta\nu_{aux}(\omega) = \Delta\nu_{sci}(\omega) \left\{ \frac{2e^{-i\omega\tau}}{1 + e^{-i2\omega\tau}} \right\} - \Delta\nu_{fib}(\omega) \left\{ \frac{(1 - e^{-i\omega\tau})^2}{1 + e^{-i2\omega\tau}} \right\} \quad (\text{D.5})$$

The true measurement of the relative frequency fluctuations between the two lasers is therefore:

$$\Delta\nu_{true}(\omega) = \{\Delta\nu_{sci}(\omega) - \Delta\nu_{fib}(\omega)\} \left\{ \frac{(1 - e^{-i\omega\tau})^2}{1 + e^{-i2\omega\tau}} \right\}, \quad (\text{D.6})$$

The transfer functions from the science laser absolute frequency fluctuations and the fibre noise to the truth measurement were modelled in Matlab [87] using the same fibre parameters from Section 7.1. These transfer functions are plotted in Figure D.2.

For frequencies well below the inverse of the fibre delay, the response in Figure D.2 is less than 1, has a frequency dependency of  $f^2$  and does not reach unity until near 10 kHz. At these frequencies the fibre induced noise is well suppressed by the AOM correction method.



# Bibliography

- [1] A. Einstein. On the electrodynamics of moving bodies. *Ann. Phys. (Berlin)*, 17(132), 1905.
- [2] A. Einstein. The foundation of the general theory of relativity. *Ann. Phys. (Berlin)*, 49(769), 1916.
- [3] A. Einstein. Approximate integration of the field equations of gravitation. *Preuss. Akad. Wiss. (Berlin)*, pages 688–696, 1916.
- [4] A. Einstein. Gravitational waves. *Preuss. Akad. Wiss. (Berlin)*, pages 154–167, 1918.
- [5] C. W. Misner, K. S. Thorne, and J. A. Wheeler. *Gravitation*. W.H. Freeman, San Francisco, 1973.
- [6] B. Schutz. *A First Course in General Relativity*. Cambridge University Press, 2nd edition, June 2009.
- [7] B. S. Sathyaprakash and B. F. Schutz. Physics, Astrophysics and Cosmology with Gravitational Waves. *Living Reviews in Relativity*, 12:2, March 2009.
- [8] B. S. Sathyaprakash and S. Dhurandhar. Choice of filters for the detection of gravitational waves from coalescing binaries. *Physical Review D*, 44:3819–3834, 1991.
- [9] R. A. Hulse and J. H. Taylor. Discovery of a pulsar in a binary system. *The Astrophysical Journal*, 195:L51–L53, January 1975.
- [10] J. M. Weisberg and J. H. Taylor. The Relativistic Binary Pulsar B1913+16: Thirty Years of Observations and Analysis. In F. A. Rasio & I. H. Stairs, editor, *Binary Radio Pulsars*, volume 328 of *Astronomical Society of the Pacific Conference Series*, page 25, July 2005.
- [11] B. Abbott et. al. Beating the spin-down limit on gravitational wave emission from the crab pulsar. *The Astrophysical Journal Letters*, 683(1):L45, 2008.
- [12] C. L. Fryer and K. C. B. New. Gravitational Waves from Gravitational Collapse. *Living Reviews in Relativity*, 14:1, January 2011.

- [13] E. Müller, M. Rampp, R. Buras, H. T. Janka, and D. H. Shoemaker. Toward gravitational wave signals from realistic core-collapse supernova models. *The Astrophysical Journal*, 603(1):221, 2004.
- [14] B. P. Abbott, R. Abbott, F. Acernese, R. Adhikari, P. Ajith, B. Allen, G. Allen, M. Alshourbagy, R. S. Amin, and S. B. et al. Anderson. An upper limit on the stochastic gravitational-wave background of cosmological origin. *Nature*, 460:990–994, August 2009.
- [15] P. R. Saulson. *Fundamentals of interferometric gravitational wave detectors*. World Scientific, Singapore, 1994.
- [16] J. Weber. Detection and generation of gravitational waves. *Physical Review*, 117:306–313, 1960.
- [17] J. Weber. Evidence for discovery of gravitational radiation. *Physical Review Letters*, 22:1320–1324, 1969.
- [18] G. E. Moss, L. R. Miller, and R. L. Forward. Photon-noise-limited laser transducer for gravitational antenna. *Applied Optics*, 10(11):2495–2498, Nov 1971.
- [19] R. L. Forward. Wideband laser-interferometer gravitational-radiation experiment. *Physical Review D*, 17:379–390, Jan 1978.
- [20] R. Weiss. Electromagnetically coupled gravitational wave antenna, 1972. Mass. Int. Technol. Res. Lab. Electron. Q. Rep., 105:54–76.
- [21] A. Abramovici, W. E. Althouse, R. W. P. Drever, Y. Gursel, S. Kawamura, F. J. Raab, D. Shoemaker, L. Sievers, R. E. Spero, K. S. Thorne, R. E. Vogt, R. Weiss, S. E. Whitcomb, and M. E. Zucker. Ligo: the laser interferometer gravitational-wave observatory. *Science*, 256:325, 1992.
- [22] A. Brillet et al. Virgo proposal to cnrs and infn. unpublished, 1989.
- [23] H. Lück et. al. The status of geo600. *Gravitational Waves: Third Edoardo Amaldi Conference, Pasadena*. ed S. Meshkov, page 119, 2000.
- [24] B. Willke et. al. The geo 600 gravitational wave detector. *Classical and Quantum Gravity*, 19(7):1377, 2002.
- [25] M. Ando, K. Tsubono, and the TAMA collaboration. Tama project: design and current status. *Gravitational Waves: Third Edoardo Amaldi Conference, Pasadena*. ed S. Meshkov, page 128, 2000.
- [26] J. R. Smith (for the LIGO Scientific Collaboration). The path to the enhanced and advanced ligo gravitational-wave detectors. *Classical and Quantum Gravity*, 26(11):114013, 2009.

- [27] F. Acernese et al. Virgo upgrade investigations. *J. Phys.: Conf. Ser.*, 32(1):223, 2006.
- [28] B. Willke et al. The geo-hf project. *Classical and Quantum Gravity*, 23(8):S207, 2006.
- [29] K. Kuroda and the LCGT Collaboration. Status of lcgt. *Classical and Quantum Gravity*, 27(8):084004, 2010.
- [30] O. Jennrich. Lisa technology and instrumentation. *Classical and Quantum Gravity*, 26(15):153001, 2009.
- [31] J. Alnis, A. Matveev, N. Kolachevsky, Th. Udem, and T. W. Hänsch. Subhertz linewidth diode lasers by stabilization to vibrationally and thermally compensated ultralow-expansion glass fabry-pérot cavities. *Physical Review A*, 77:053809, May 2008.
- [32] H. B. Callen and T. A. Welton. Irreversibility and generalized noise. *Physical Review*, 83(1):34–40, Jul 1951.
- [33] H. B. Callen and R. F. Greene. On a theorem of irreversible thermodynamics. *Physical Review*, 86(5):702–710, Jun 1952.
- [34] P. R. Saulson. Thermal noise in mechanical experiments. *Physical Review D*, 42:2437–2445, Oct 1990.
- [35] A. Gillespie and F. Raab. Thermal noise in the test mass suspensions of a laser interferometer gravitational-wave detector prototype. *Physics Letters A*, 178(5-6):357–363, 1993.
- [36] G. M. Harry, A. M. Gretarsson, P. R. Saulson, S. E. Kittelberger, S. D. Penn, W. J. Startin, S. Rowan, M. M. Fejer, D. R. M. Crooks, G. Cagnoli, J. Hough, and N. Nakagawa. Thermal noise in interferometric gravitational wave detectors due to dielectric optical coatings. *Classical and Quantum Gravity*, 19:897, 2002.
- [37] G. M. Harry, H. Armandula, E. Black, D. R. M. Crooks, G. Cagnoli, J. Hough, P. Murray, S. Reid, S. Rowan, P. Sneddon, M. M. Fejer, R. Route, and S. Penn. Thermal noise from optical coatings in gravitational wave detectors. *Applied Optics*, 45:1569, 2006.
- [38] C. M. Caves. Quantum-mechanical radiation-pressure fluctuations in an interferometer. *Physical Review Letters*, 45:75–79, Jul 1980.
- [39] W A Edelstein, J Hough, J R Pugh, and W Martin. Limits to the measurement of displacement in an interferometric gravitational radiation detector. *Journal of Physics E: Scientific Instruments*, 11(7):710, 1978.

- [40] G. M. Harry and the LIGO Scientific Collaboration. Advanced ligo: the next generation of gravitational wave detectors. *Classical and Quantum Gravity*, 27(8):084006, 2010.
- [41] D. R. Herriott and H. J. Schulte. Folded optical delay lines. *Applied Optics*, 4(8):883–889, Aug 1965.
- [42] D. Shoemaker, R. Schilling, L. Schnupp, W. Winkler, K. Maischberger, and A. Rüdiger. Noise behavior of the garching 30-meter prototype gravitational-wave detector. *Physical Review D*, 38:423–432, Jul 1988.
- [43] Ch. Fabry and A. Perot. On a new form of interferometer. *The Astrophysical Journal*, 13:265–272, 1901.
- [44] R. W. P. Drever. *Interferometric detectors of gravitational radiation*, in, *Gravitational Radiation*, by N. Deruelle and T. Piran. North-Holland Pub. Co., 1983.
- [45] B. J. Meers. Recycling in laser-interferometric gravitational-wave detectors. *Physical Review D*, 38:2317–2326, Oct 1988.
- [46] D. Schnier, J. Mizuno, G. Heinzel, H. Lück, A. Rüdiger, R. Schilling, M. Schrempel, W. Winkler, and K. Danzmann. Power recycling in the garching 30 m prototype interferometer for gravitational-wave detection. *Physics Letters A*, 225:210, 1997.
- [47] B. J. Meers. The frequency response of interferometric gravitational wave detectors. *Physics Letters A*, 142:465 – 470, 1989.
- [48] M. B. Gray, A. J. Stevenson, H.-A. Bachor, and D. E. McClelland. Broadband and tuned signal recycling with a simple michelson interferometer. *Applied Optics*, 37:5886, 1998.
- [49] D. Shoemaker. Advanced ligo anticipated sensitivity curves. Technical Report LIGO-T00900288-v3, LIGO Laboratory, January 2009.
- [50] Best strain sensitivities for the ligo interferometers - comparison among s1-s5 runs. Technical Report LIGO-G060009-03, LIGO Laboratory.
- [51] G. Gonzalez. Suspensions thermal noise in the ligo gravitational wave detector. *Classical and Quantum Gravity*, 17(21):4409, 2000.
- [52] Joseph Giaime, Partha Saha, David Shoemaker, and Lisa Sievers. A passive vibration isolation stack for ligo: Design, modeling, and testing. *Review of Scientific Instruments*, 67(1):208–214, 1996.
- [53] R. L. Savage, P. J. King, and S. U. Seel. A highly stabilized 10-watt nd:yag laser for the laser interferometric gravitational wave observatory (ligo). *Laser Physics*.

- [54] B. Abbott et. al. Detector description and performance for the first coincidence observations between ligo and geo. *Nuclear Instruments and Methods in Physics Research Section A: Accelerators, Spectrometers, Detectors and Associated Equipment*, 517:154 – 179, 2004.
- [55] A. Abramovici and J. Chapsky. *Feedback Control Systems: A fast-track guide for scientists and engineers*. Kluwer academic publishers, 2000.
- [56] R. Adhikari. *Sensitivity and Noise Analysis of 4 km Laser Interferometric Gravitational Wave Antennae*. PhD thesis, Massachusetts Institute of Technology, 2004.
- [57] F Acernese et. al. Environmental noise studies in virgo. *Journal of Physics: Conference Series*, 32(1):80, 2006.
- [58] Kazuhiro Yamamoto, Shigemi Otsuka, Masaki Ando, Keita Kawabe, and Kimio Tsubono. Study of the thermal noise caused by inhomogeneously distributed loss. *Classical and Quantum Gravity*, 19(7):1689, 2002.
- [59] G Manson and G Hoffmann de Visme. The frequency spectrum of barkhausen noise. *Journal of Physics D: Applied Physics*, 5(8):1389, 1972.
- [60] J. A. Giaime, E. J. Daw, M. Weitz, R. Adhikari, P. Fritschel, R. Abbott, R. Bork, and J. Heefner. Feedforward reduction of the microseism disturbance in a long-base-line interferometric gravitational-wave detector. *Review of Scientific Instruments*, 74(1):218–224, 2003.
- [61] R Abbott, R Adhikari, G Allen, S Cowley, E Daw, D DeBra, J Giaime, G Hammond, M Hammond, C Hardham, J How, W Hua, W Johnson, B Lantz, K Mason, R Mittleman, J Nichol, S Richman, J Rollins, D Shoemaker, G Stapfer, and R Stebbins. Seismic isolation for advanced ligo. *Classical and Quantum Gravity*, 19(7):1591, 2002.
- [62] J. Kissel. Advanced ligo active seismic isolation. Technical Report LIGO-G1100431, LIGO Laboratory, April 2011.
- [63] M. Evans. Seismic noise spectra for sei and sus. Technical Report LIGO-T1200155-v1, LIGO Laboratory, 2012.
- [64] J. Miller, M. Evans, L. Barsotti, P. Fritschel, M. MacInnis, R. Mittleman, B. Shapiro, J. Soto, and C. Torrie. Damping parametric instabilities in future gravitational wave detectors by means of electrostatic actuators. *Physics Letters A*, 375(3):788 – 794, 2011.
- [65] A. Yariv. *Optical Electronics in Modern Communications*. Oxford University Press, New York, 6 edition, 2007.
- [66] S. W. Smith. *The Scientist and Engineer's Guide To Digital Signal Processing*. California Technical Publishing, 1997.

- [67] R. W. P. Drever, J. L. Hall, F. V. Kowalski, J. Hough, G. M. Ford, A. J. Munley, and H. Ward. Laser phase and frequency stabilization using an optical resonator. *Appl. Phys. B*, 31:97, 1983.
- [68] E. D. Black. An introduction to pound–drever–hall laser frequency stabilization. *Am. J. Phys.*, 69(1):79–87, 2001.
- [69] E. Hecht. *Optics*. Addison-Wesley, Reading, 2 edition, 1987.
- [70] M. W. Regehr, F. J. Raab, and S. E. Whitcomb. Demonstration of a power-recycled michelson interferometer with fabry–perot arms by frontal modulation. *Optics Letters*, 20(13):1507–1509, Jul 1995.
- [71] R. Flaminio and H.h Heitmann. Longitudinal control of an interferometer for the detection of gravitational waves. *Physics Letters A*, 214:112 – 122, 1996.
- [72] M. Ando, K. Kawabe, and K. Tsubono. Signal-separation technique for a power-recycled interferometric gravitational wave detector. *Physics Letters A*, 237:13 – 20, 1997.
- [73] L. Schnupp. unpublished, workshop on Gravitational Wave detectors, Munich, 1988.
- [74] R L Ward, R Adhikari, B Abbott, R Abbott, D Barron, R Bork, T Fricke, V Frolov, J Heefner, A Ivanov, O Miyakawa, K McKenzie, B Slagmolen, M Smith, R Taylor, S Vass, S Waldman, and A Weinstein. dc readout experiment at the caltech 40m prototype interferometer. *Classical and Quantum Gravity*, 25(11):114030, 2008.
- [75] T. Fricke, N. Smith-Lefebvre, R. Abbott, R. Adhikari, K. L. Dooley, M. Evans, P. Fritschel, V. Frolov, K. Kawabe, J. S. Kissel, and S. Waldman. DC readout experiment in Enhanced LIGO. *ArXiv e-prints*, October 2011.
- [76] N. Smith-Lefebvre, S. Ballmer, M. Evans, S. Waldman, K. Kawabe, V. Frolov, and N. Mavalvala. Optimal alignment sensing of a readout mode cleaner cavity. *Optics Letters*, 36(22):4365–4367, Nov 2011.
- [77] B. J. J. Slagmolen, A. J. Mullavey, J. Miller, D. E. McClelland, and P. Fritschel. Tip-tilt mirror suspension: Beam steering for advanced laser interferometer gravitational wave observatory sensing and control signals. *Review of Scientific Instruments*, 82(12):125108, 2011.
- [78] D. Z. Anderson. Alignment of resonant optical cavities. *Applied Optics*, 23(17):2944–2949, Sep 1984.
- [79] D. Coyne, P. Fritschel, J. Romie, and N. Robertson. Design specifications for the omc suspension. Technical Report LIGO-T070189-v2, LIGO Laboratory, August 2007.

- [80] I. Stevanovic and A. Weinstein. Understanding the ligo optics suspension controller electronics design. Technical Report LIGO-T000097-00-R, LIGO Laboratory, 2000.
- [81] M. V. Plissi. Cantilever blade analysis for advanced ligo. Technical Report LIGO-T030107-00-D, LIGO Laboratory, June 2003.
- [82] C. Torrie and N. Robertson. Triple pendulum blade parameters. Technical Report LIGO-T0900365-v2, LIGO Laboratory, July 2009.
- [83] S. M. Aston and D. M. Hoyland. Bosem design document and test report. Technical Report LIGO-T050111-04-K, LIGO Laboratory, March 2009.
- [84] G. Gonzalez. Asc: Environmental input to alignment noise. Technical Report LIGO-T960103-00-D, LIGO Laboratory, July 1996.
- [85] Mathematica notebook by mark a. barton, mark barton's suspension models, <http://www.ligo.caltech.edu/e2e/susmodels/index.html>, 2008.
- [86] P. A. Tipler. *Physics: for Scientists and Engineers*. WH Freeman & Co., 4 edition, 1999.
- [87] <http://www.mathworks.com/>.
- [88] M. Evans, N. Mavalvala, P. Fritschel, R. Bork, B. Bhawal, R. Gustafson, W. Kells, M. Landry, D. Sigg, R. Weiss, S. Whitcomb, and H. Yamamoto. Lock acquisition of a gravitational-wave interferometer. *Optics Letters*, 27(8):598–600, Apr 2002.
- [89] M. Evans. *Lock Acquisition for Resonant Optical Interferometers*. PhD thesis, California Institute of Technology, 2002.
- [90] E. J. Daw, J. A. Giaime, D. Lormand, M. Lubinski, and J. Zweizig. Long-term study of the seismic environment at ligo. *Classical and Quantum Gravity*, 21(9):2255, 2004.
- [91] R. Ward. *Length Sensing and Control of a Prototype Advanced Interferometric Gravitational Wave Detector*. PhD thesis, California Institute of Technology, 2010.
- [92] R. Abbott, R. Adhikari, S. Ballmer, L. Barsotti, M. Evans, P. Fritschel, V. Frolov, G. Mueller, B. Slagmolen, and S. Waldman. Advligo interferometer sensing and control conceptual design. Technical Report LIGO-T070247-01-I, LIGO Laboratory, April 2008.
- [93] P. Fritschel, D. McClelland, A. Mullavey, D. Shaddock, B. Slagmolen, , and S. Waldman. Adv. ligo arm length stabilisation requirements. Technical Report LIGO-T0900095-v2-D, LIGO Laboratory, April 2009.
- [94] Y. Aso. *Active Vibration Isolation for a Laser Interferometric Gravitational Wave Detector using a Suspension Point Interferometer*. PhD thesis, University of Tokyo, 2006.

- [95] D. A. Shaddock. Digitally enhanced heterodyne interferometry. *Optics Letters*, 32, 2007.
- [96] M. Principe, I. Pinto, V. Pierro, and R. DeSalvo. Minimum brownian noise dichroic dielectric mirror coating for advligo. Technical Report LIGO-T0803366-00-D, LIGO Laboratory, November 2008.
- [97] B. E. A. Saleh and M. C. Teich. *Fundamentals of Photonics*. John Wiley & Sons, Inc., New York, 1991.
- [98] T. J. Kane and R. L. Byer. Monolithic, unidirectional single-mode nd:yag ring laser. *Optics Letters*, 10(2):65–67, Feb 1985.
- [99] T. T. Y. Lam, B. J. J. Slagmolen, J. H. Chow, I. C. M. Littler, D. E. McClelland, and D. A. Shaddock. Digital laser frequency stabilization using an optical cavity. *IEEE Journal of Quantum Electronics*, 46(8):1178 –1183, aug. 2010.
- [100] M. B. Gray, D. A. Shaddock, C. C. Harb, and H. A. Bachor. Photodetector designs for low-noise, broadband, and high-power applications. *Review Scientific Instruments*, 69(11):3755–3762, 1998.
- [101] B. J. Cusack, B. S. Sheard, D. A. Shaddock, M. B. Gray, P. K. Lam, and S. E. Whitcomb. Electro-optic modulator capable of generating simultaneous amplitude and phase modulations. *Applied Optics*, 43(26):5079–5091, Sept 2004.
- [102] D. Coyne. Vacuum hydrocarbon outgassing requirements. Technical Report LIGO-T040001-00-D, LIGO Laboratory, January 2004.
- [103] B. J. J. Slagmolen, P. Fritschel, D. Sigg, J. Miller, A. J. Mullavey, S. J. Waldman, M. Evans, K. Arai, A. F. Brooks, D. Yeaton-Massey, L. Barsotti, R. Adhikari, and D. E. McClelland. Arm-length stabilisation for advanced ligo lock acquistion. In preparation, 2012.
- [104] S. A. Diddams, L. Hollberg, L. S. Ma, and L. Robertsson. Femtosecond-laser-based optical clockwork with instability  $\leq 6.3 \times 10^{-16}$  in 1s. *Optics Letters*, 27(1):58–60, 2002.
- [105] Th. Udem, R. Holzwarth, and T. W. Hansch. Optical frequency metrology. *Nature*, 416:233–237, 2002.
- [106] S. M. Foreman, K. W. Holman, D. D. Hudson, D. J. Jones, and J. Ye. Remote transfer of ultrastable frequency references via fiber networks. *Review of Scientific Instruments*, 78(021101), 2007.
- [107] F. Narbonneau, M. Lours, S. Bize, A. Clairon, G. Santarelli, O. Lopez, Ch. Daussy, A. Amy-Klein, and Ch. Chardonnet. High resolution frequency standard dissemination via optical fiber metropolitan network. *Review of Scientific Instruments*, 77(064701), 2006.

- [108] A. J. Mullavy, B. J. J. Slagmolen, D. A. Shaddock, and D. E. McClelland. Stable transfer of an optical frequency standard via a 4.6 km optical fiber. *Optics Express*, 18(5):5213–5220, Mar 2010.
- [109] P. A. Williams, W. C. Swann, and N. R. Newbury. High-stability transfer of an optical frequency over long fiber-optic links. *J. Opt. Soc. Am. B*, 25(8):1284–1293, 2008.
- [110] G. Grosche, O. Terra, K. Predahl, R. Holzwarth, B. Lipphardt, F. Vogt, U. Sterr, and H. Schnatz. Optical frequency transfer via 146km fiber link with  $10^{-19}$  relative accuracy. *Optics Letters*, 34(15):2270–2272, 2009.
- [111] L. S. Ma, P. Jungner, J. Ye, and J. L. Hall. Delivering the same optical frequency at two places: accurate cancellation of phase noise introduced by an optical fiber or other time-varying path. *Optics Letters*, 19(21):1777–1779, 1994.
- [112] G. Heinzel, C. Braxmaier, K. Danzmann, P. Gath, J. Hough, O. Jennrich, U. Johann, A. Rudiger, M. Sallusti, and H. Schulte. Lisa interferometry: recent developments. *Classical and Quantum Gravity*, 23:S119–S124, 2006.
- [113] P. Kwee and B. Willke. Automatic laser beam characterization of monolithic nd:yag nonplanar ring lasers. *Applied Optics*, 47(32):6022–6032, Nov 2008.
- [114] N. A. Robertson, M. Barton, D. Bridges, J. Heefner, M. Meyer, J. Romie, and C. Torrie. Omc suspension final design document. Technical Report LIGO-T0900060-v1, LIGO Laboratory, March 2009.
- [115] S. Ngo. Control of optical resonators using digitally enhanced interferometry. Master’s thesis, Australian National University, 2011.
- [116] D. M. R. Wuchenich, T. T. Y. Lam, J. H. Chow, D. E. McClelland, and D. A. Shaddock. Laser frequency noise immunity in multiplexed displacement sensing. *Optics Letters*, 36(5):672–674, Mar 2011.
- [117] Icon (intra government communications network), <http://www.finance.gov.au/e-government/infrastructure/icon/index.html>, 2010.
- [118] P. E. Ciddor. Refractive index of air: new equations for the visible and near infrared. *Applied Optics*, 35(9):1566–1573, Mar 1996.
- [119] E. R. Peck and K. Reeder. Dispersion of air. *J. Opt. Soc. Am.*, 62(8):958–962, Aug 1972.
- [120] T. B. Quoc, M. Ishige, Y. Ohkubo, and M. Aketagawa. Measurement of air-refractive-index fluctuation from laser frequency shift with uncertainty of order  $10^{-9}$ . *Measurement Science and Technology*, 20(12):125302, 2009.